

**Experimental investigation of ultrafast
internal conversion in aniline and
1,4-diazabicyclo[2.2.2]octane (DABCO)**

ROMAN SPESYVTSEV

A THESIS SUBMITTED FOR THE DEGREE OF
DOCTOR OF PHILOSOPHY

UNIVERSITY COLLEGE LONDON

January 2013

I, Roman Spesyvtsev, confirm that the work presented in this thesis is my own. Where information has been derived from other sources, I confirm that this has been indicated in the thesis.

Abstract

Pump-probe time-resolved photoelectron spectroscopy is employed to investigate ultrafast non-adiabatic dynamics in aniline, deuterated aniline (aniline-D₇) and 1,4-diazabicyclo[2.2.2]octane (DABCO).

Aniline molecules are photoexcited over a wide range of wavelengths between 269 and 236 nm. Our observations reveal direct population of the S₂($\pi 3s/\pi\sigma^*$) state. The photoelectron energy and angular distributions obtained in our experiments show an interesting bifurcation of the Rydberg population to two non-radiative decay channels. One of these involves ultrafast relaxation from the Rydberg component of the S₂($\pi 3s/\pi\sigma^*$) state to the S₁($\pi\pi^*$) state, from which the population relaxes back to the electronic ground state on a much longer timescale. The other channel appears to involve motion along the $\pi\sigma^*$ dissociative potential energy surface. At higher excitation energies, the dominant excitation is to the S₃($\pi\pi^*$) state, which undergoes extremely efficient electronic relaxation back to the ground state.

Aniline-D₇ is photoexcited with 260 nm wavelength light. The photodynamics of aniline-D₇ is similar to those observed in aniline. Comparison of the dynamics of aniline and aniline-D₇ confirm that the relaxation of the $\pi 3s$ component of the S₂($\pi 3s/\pi\sigma^*$) state to the S₁($\pi\pi^*$) state is a main relaxation pathway.

Photodynamics of DABCO molecules were also studied over a wide range of wavelengths between 251 and 234 nm. The ultrafast internal conversion in DABCO between the S₂ 3p_{*x,y*}(+) and S₁ 3s(+) Rydberg states follows a biexponential decay. It was found that initial randomly oriented molecules are partially aligned after absorption of linearly polarised light and, therefore, DABCO exhibits a preferential direction of excitation.

This thesis is based on the following publications:

Parts of Chapters 1 and 2:

- R. Spesyvtsev, J.G. Underwood, H.H. Fielding, *Ultrafast phenomena in molecular sciences*, ch. Time resolved photoelectron spectroscopy for excited state dynamics. Springer, to be published in 2013.

Chapter 3:

- R. Spesyvtsev, O.M. Kirkby, H.H. Fielding, *Ultrafast dynamics of aniline following 269-238 nm excitation and the role of the $S_2(\pi 3s/\pi\sigma^*)$ state*, Faraday Discuss. 157 (2012) 165-179.
- R. Spesyvtsev, O.M. Kirkby, M. Vacher, H.H. Fielding, *Shedding new light on the role of the Rydberg state in the photochemistry of aniline*, Phys. Chem. Chem. Phys. 14 (2012) 9942-9947.

Chapter 4:

- R. Spesyvtsev, R.S. Minns, M. Siano, J. Marangos, R. Livingstone, D. Townsend, D.M.P. Holland, E. Springate, E. Turcu, M.S. Schuurman, H.H. Fielding, J.G. Underwood, *Time-resolved photoelectron imaging studies of the ultrafast S_2 - S_1 internal conversion in the DABCO molecule*, in preparation.

In addition, contributions were made to the following publications:

- T.J. Penfold, D.S.N. Parker, R.S. Minns, R. Spesyvtsev, H.H. Fielding, G. A. Worth, *Quantum dynamics study of the competing ultrafast intersystem crossing and internal conversion in the “channel 3” region of benzene*, The Journal of Chemical Physics 137 (2012) 204310.
- A.D.G. Nunn, R.S. Minns, R. Spesyvtsev, M.J. Bearpark, M.A. Robb and H.H. Fielding, *Ultrafast dynamics through conical intersections and intramolecular vibrational energy redistribution in styrene*, Phys. Chem. Chem. Phys. 12 (2010) 15751-15759.

Acknowledgements

I am grateful to my supervisors Prof Helen Fielding and Dr Jonathan Underwood for giving me this exciting opportunity to work in the advanced field of ultrafast science. I am especially thankful to Prof Fielding for her everyday support, encouragement and enthusiasm and to Dr Underwood for sharing his experience and for numerous insightful discussions during my PhD. I would like to thank Dr Russell Minns for his patient help with the experimental setup at UCL, especially in the first year of my PhD, and for his company throughout all our collaborative experiments. I would also like to thank Oliver Kirkby, with whom I have spent many hours taking endless spectra of the aniline molecule. I thank Morgane Vacher, with whom we started our aniline experiments, Garikoitz Balerdi Villanueva with whom I worked in the lab, and Matthieu Sala who provided us with theoretical insight into aniline.

My thanks also go all collaborators with whom I worked on experiments at Rutherford Appleton Laboratory and Imperial College London: Prof Jon Marangos, Prof John Tisch, Dr Dave Townsend, Dr David Holland, Dr Emma Springate, Dr Edmond Turcu, Dr Felix Frank, Dr Marco Siano, Dr Ruth Livingstone; as well as to collaborators at the University of Nottingham: Prof Katherine Reid and Jonathan Midgely. In addition I would also like to thank everybody with whom I shared many hours in our office, especially Ciarán Mooney who always had my back.

Many thanks to the experimental support staff at UCL who always were there when needed, especially to Jim Stevenson for mechanical support and Dr Steve Fifth for support with the lab equipment.

I would also like to thank the Marie Curie FASTQUAST Network for funding and networking opportunities and to all FASTQUAST members with whom I had many discussions during meetings and conferences.

Finally, I would like to thank my family - my darling wife, my parents, and my sister for their love and support throughout my work.

Contents

| | | |
|----------|--|-----------|
| 1 | Introduction | 14 |
| 1.1 | Photochemistry of polyatomic molecules | 16 |
| 1.1.1 | Born-Oppenheimer approximation | 16 |
| 1.1.2 | Non-adiabatic dynamics | 17 |
| 1.1.3 | Franck-Condon principle | 20 |
| 1.1.4 | Jablonski diagram | 21 |
| 1.2 | Wavepacket dynamics | 22 |
| 1.3 | Time-resolved photoelectron spectroscopy | 24 |
| 1.3.1 | Koopmans' picture | 24 |
| 1.3.2 | Energy correlation between excited states and photoelectrons . | 25 |
| 1.4 | Photoelectron angular distributions | 27 |
| 1.5 | Applications of time-resolved photoelectron spectroscopy and imaging | 29 |
| 1.5.1 | Internal conversion | 29 |
| 1.5.2 | Intra-molecular vibrational energy redistribution | 31 |
| 1.5.3 | Intersystem crossing | 32 |
| 1.5.4 | Isomerisation | 33 |
| 1.5.5 | Photodissociation | 34 |
| 1.6 | Conclusions | 36 |
| 2 | Experimental toolkit | 38 |
| 2.1 | Femtosecond light sources | 39 |
| 2.2 | Molecular sources for gas phase measurements | 42 |
| 2.3 | Photoelectron spectrometers | 43 |
| 2.4 | UCL experimental setup | 44 |
| 2.4.1 | Femtosecond laser system | 44 |
| 2.4.2 | Nonlinear optics | 45 |

| | | |
|----------|--|-----------|
| 2.4.3 | Layout of the laser setup | 47 |
| 2.4.4 | Vacuum system | 49 |
| 2.5 | RAL experimental setup | 51 |
| 2.5.1 | Femtosecond laser system | 51 |
| 2.5.2 | Vacuum system | 52 |
| 2.6 | Experimental procedures and diagnostics | 54 |
| 2.6.1 | VMI reconstruction | 55 |
| 2.6.2 | VMI energy calibration | 57 |
| 2.6.3 | Pump-probe cross-correlation | 61 |
| 2.6.4 | Mass spectrum and ion imaging | 62 |
| 2.7 | Data analysis | 64 |
| 2.7.1 | Exponential kinetics | 64 |
| 2.7.2 | Fitting of the experimental data | 69 |
| 3 | Ultrafast non-adiabatic dynamics in aniline | 72 |
| 3.1 | Introduction | 73 |
| 3.2 | $\pi\sigma^*$ and $n\sigma^*$ states | 73 |
| 3.3 | Spectroscopy, structure and dynamics | 75 |
| 3.3.1 | Spectroscopy and structure of aniline | 75 |
| 3.3.2 | Intersystem crossing | 79 |
| 3.3.3 | Internal conversion | 79 |
| 3.3.4 | H atom loss | 81 |
| 3.4 | TRPEI investigation of aniline following 269 – 236 nm excitation | 84 |
| 3.4.1 | Experimental method | 84 |
| 3.4.2 | Integrated photoelectron intensity | 87 |
| 3.4.3 | Time-resolved photoelectron spectra | 87 |
| 3.4.4 | Timescales | 92 |
| 3.4.5 | Relaxation pathway | 95 |
| 3.5 | TRPEI investigation of deuterated aniline | 101 |
| 3.5.1 | Experimental method | 101 |
| 3.5.2 | Time-resolved photoelectron spectra | 102 |
| 3.5.3 | Timescales | 103 |
| 3.5.4 | Relaxation pathway | 105 |
| 3.6 | Discussion | 106 |

| | | |
|----------|--|------------|
| 3.6.1 | $S_2(\pi 3s/\pi\sigma^*)$ | 106 |
| 3.6.2 | $S_3(\pi\pi^*)$ | 109 |
| 3.7 | Conclusion | 111 |
| 4 | Ultrafast non-adiabatic dynamics in DABCO | 114 |
| 4.1 | Introduction | 115 |
| 4.2 | Spectroscopy, structure and dynamics | 115 |
| 4.2.1 | Spectroscopy of DABCO | 115 |
| 4.2.2 | Structure of DABCO | 117 |
| 4.2.3 | Internal conversion in DABCO | 118 |
| 4.3 | TRPEI investigation of DABCO following 251 – 234 nm excitation | 119 |
| 4.3.1 | Experimental method | 119 |
| 4.3.2 | Time-resolved photoelectron spectra | 121 |
| 4.3.3 | Timescales | 123 |
| 4.3.4 | Photoelectron anisotropy | 128 |
| 4.4 | Discussion | 129 |
| 4.4.1 | S_2 $3p_{x,y}(+)$ | 129 |
| 4.4.2 | S_1 $3s(+)$ | 131 |
| 4.5 | Conclusion | 132 |
| 5 | Summary and outlook | 134 |
| 5.1 | Ultrafast internal conversion in aniline | 134 |
| 5.2 | Ultrafast internal conversion in DABCO | 135 |
| | Appendix A Convolution integrals | 154 |
| A.1 | Double integral with variable limits of integration | 154 |
| A.2 | Triple integral with variable limits of integration | 157 |
| | Appendix B Image Inversion software | 159 |
| B.1 | Introduction | 159 |
| B.2 | User manual | 160 |
| B.2.1 | Computer requirements. | 160 |
| B.2.2 | GUI controls. | 160 |
| B.3 | Development information and compilation instructions | 164 |

List of Figures

| | | |
|------|--|----|
| 1.1 | Potential energy surfaces and conical intersections | 18 |
| 1.2 | A Jablonski diagram | 21 |
| 1.3 | Excitation and ionisation of a coherent superposition of excited eigen- states | 23 |
| 1.4 | Koopmans' picture of a pump-probe experiment | 25 |
| 1.5 | Energy level diagram for a pump-probe experiment | 26 |
| 1.6 | Energy level scheme for TRPES of 2,4,6,8-decatetraene | 29 |
| 1.7 | Schematic of the TRPES experiment and the photoelectron signal components of the electronically excited states of DABCO | 30 |
| 1.8 | TRPES following excitation of the $6a^1 + 10b^1 16b^1$ Fermi resonance in toluene | 31 |
| 1.9 | TRPES study of the ISC in aniline, 2-aminopyridine, and 3-aminopyridine | 32 |
| 1.10 | TRPES of the isomerisation of azobenzene | 33 |
| 1.11 | Schematic energy level diagram and TRPES experimental results of photodissociation of $(NO)_2^*$ | 35 |
| 1.12 | TRCIS photodissociation study of $(NO)_2^*$ | 36 |
| 2.1 | Schematic diagram of the UCL femtosecond laser system | 45 |
| 2.2 | Schematic view of the optical parametric amplification | 46 |
| 2.3 | Layout of the laser setup used for the experiments described in chapter 3 | 48 |
| 2.4 | Schematic view of the UCL vacuum system used for the experiments presented in chapter 3 | 49 |
| 2.5 | Schematic view of the velocity map imaging detector used for the experiments presented in chapter 3 | 50 |
| 2.6 | Layout of the laser setup used for the experiments described in chapter 4 | 52 |
| 2.7 | Schematic view of the Roentdek delay line anode detector | 53 |

| | | |
|------|---|----|
| 2.8 | Example of velocity map image processing obtained from the delay line anode detector | 54 |
| 2.9 | Flow chart of the processing procedure for data from the VMI spectrometer | 55 |
| 2.10 | Photoelectron imaging scheme | 56 |
| 2.11 | Calibration of the VMI detector using Xe peaks | 58 |
| 2.12 | Calibration of the VMI detector using the vibrational structure of NO ⁺ | 59 |
| 2.13 | FWHM of two photoelectron peaks from the Xe spectrum as a function of the extractor voltage | 60 |
| 2.14 | Pump-probe cross-correlation measurements using 2+1' non-resonant multiphoton ionisation of Xe | 61 |
| 2.15 | Time of flight spectrum of aniline | 62 |
| 2.16 | Velocity map image of aniline ions | 63 |
| 2.17 | Schematic diagram of a pump-probe experiment | 65 |
| 3.1 | Aniline molecule | 73 |
| 3.2 | A schematic diagram of the adiabatic potential energy surfaces produced from the interaction between the $\pi\sigma^*$ dissociative valence state and the $\pi 3s$ / Rydberg state. | 74 |
| 3.3 | A gas-phase UV absorption spectrum of aniline | 75 |
| 3.4 | An energy level diagram of the low-lying electronic states of aniline and its cation | 77 |
| 3.5 | Femtosecond pump-probe photoionisation study of aniline. | 80 |
| 3.6 | Schematic potential energy curves for the four lowest singlet states of aniline along the N-H stretch coordinate | 81 |
| 3.7 | Experimental results of H atom photofragment translational spectroscopy | 82 |
| 3.8 | H atom total kinetic energy release spectrum following excitation of aniline with 240 nm and 200 nm | 83 |
| 3.9 | TOF mass spectrum of aniline, gas-phase UV absorption spectrum of aniline with pump and probe pulse profiles superimposed, and aniline excitation scheme | 85 |

| | | |
|------|---|-----|
| 3.10 | TRPEI of aniline. Velocity map image, photoelectron spectrum and anisotropy parameter, β_2 , recorded with a 240 nm pump pulse, a 300 nm probe pulse and a pump-probe delay of 5 fs. | 86 |
| 3.11 | TRPEI of aniline. Time evolution of the integrated photoelectron signal and the photoelectron kinetic energy spectra as a function of pump-probe delay following excitation of aniline at 269 nm and 250 nm | 88 |
| 3.12 | TRPEI of aniline. Time evolution of the integrated photoelectron signal and the photoelectron kinetic energy spectra as a function of pump-probe delay following excitation of aniline at 240 nm, 238 nm and 236 nm | 89 |
| 3.13 | TRPEI of aniline. Photoelectron anisotropy parameter, β_2 , as a function of pump-probe delay time averaged over different photoelectron kinetic energy ranges for 250 nm and 240 nm excitation wavelengths . | 91 |
| 3.14 | TRPEI of aniline. Integrated photoelectron counts as a function of pump-probe delay following excitation at 269 nm and 250 nm | 93 |
| 3.15 | TRPEI of aniline. Integrated photoelectron counts as a function of pump-probe delay following excitation at 240 nm, 238 nm and 236 nm | 94 |
| 3.16 | TRPEI of aniline. Spectral components of the three decays and modelled photoelectron spectra for 269 nm, 250 nm and 236 nm excitation | 97 |
| 3.17 | TRPEI of aniline. Smoothed photoelectron spectral profiles and reconstructed photoelectron spectra for 236 nm excitation | 98 |
| 3.18 | TRPEI of aniline. Smoothed photoelectron spectral profiles and reconstructed photoelectron spectra for 240 nm and 238 nm excitation . | 99 |
| 3.19 | TRPEI of aniline. Photoelectron energy spectra for different excitation wavelengths and a 300 nm ionisation pulse | 100 |
| 3.20 | TRPEI of deuterated aniline. Velocity map image, photoelectron spectrum and anisotropy parameter, β_2 , recorded with a 260 nm pump pulse, a 305 nm probe pulse and a pump-probe delay of 3 fs . . | 102 |
| 3.21 | TRPEI of deuterated aniline. Time evolution of the integrated photoelectron signal and the photoelectron kinetic energy spectra as a function of pump-probe delay following excitation of deuterated aniline at 260 nm and ionisation with 305 nm | 103 |
| 3.22 | TRPEI of deuterated aniline. Integrated photoelectron counts as a function of pump-probe delay following excitation at 260 nm | 104 |

| | | |
|------|---|-----|
| 3.23 | TRPEI of deuterated aniline. Spectral components of the three decays and modelled photoelectron spectra for 260 nm excitation | 105 |
| 3.24 | 1/e decay times of the $S_2(\pi 3s/\pi\sigma^*)$ for aniline and deuterated aniline | 107 |
| 3.25 | Schematic diagram summarising the non-radiative decay pathways in aniline | 112 |
| 4.1 | DABCO molecule | 115 |
| 4.2 | A gas-phase UV absorption spectrum of DABCO | 116 |
| 4.3 | TRPEI of DABCO. Excitation scheme | 120 |
| 4.4 | TRPEI of DABCO. Velocity map image, photoelectron spectrum and anisotropy parameters recorded with a 251.2 nm pump pulse, a 400 nm probe pulse and a pump-probe delay of 150 fs | 121 |
| 4.5 | Time resolved photoelectron spectra of DABCO | 122 |
| 4.6 | TRPEI of DABCO. Summary of 1/e decay lifetimes of the electronically excited states, listed in Table 4.1 | 124 |
| 4.7 | TRPEI of DABCO. Integrated photoelectron counts of the $S_2 3p_{x,y}(+)$ photoelectron component (0.7 eV to 1.2 eV) as a function of pump-probe delay time | 125 |
| 4.8 | TRPEI of DABCO. Spectral components of the two decay times obtained from the analysis of the TRPES | 126 |
| 4.9 | TRPEI of DABCO. Modelled photoelectron spectra for 233.9 nm, 236.1 nm, 238.2 nm, 241.1 nm, 243.3 nm, 245.7 nm and 251.2 nm pump wavelengths | 127 |
| 4.10 | TRPEI of DABCO. Time dependent anisotropy parameters of the $S_1 3s(+)$ and $S_2 3p_{x,y}(+)$ photoelectron components | 129 |
| A.1 | Diagram showing the rotation of the coordinates system | 155 |
| A.2 | Integration area of the double integral (A.11) | 157 |
| B.1 | Block diagram of the main modules of the Image Inversion software . | 159 |
| B.2 | Layout of the Image Inversion software interface | 161 |

List of Tables

| | | |
|-----|--|-----|
| 2.1 | Available wavelength ranges from the Coherent OPAs used at UCL | 47 |
| 2.2 | NO ⁺ vibrational energy terms and photoelectron energies after two photon ionisation of NO with a 243 nm laser pulse. | 60 |
| 3.1 | Summary of 1/e decay lifetimes of the electronically excited states in aniline | 95 |
| 4.1 | Summary of 1/e decay lifetimes of the electronically excited states in DABCO | 124 |

Chapter 1

Introduction

The energy carried by light can be converted *via* photophysical and photochemical reactions into many applications and functions. Photochemical reactions are an important class of processes occurring in the biological sciences including vision, photosynthesis and light harvesting complexes [1, 2], and material sciences such as photovoltaics and photodegradation of materials [3, 4]. Following absorption of an ultraviolet (UV) photon, a molecule may be promoted to an excited electronic state. Photoexcitation of biological molecules in the UV region can also lead to excited-state photochemistry which may result in irreversible damage [5, 6]. However, many important biological chromophores, including DNA bases, are remarkably photostable [7, 8, 9, 10]. Their photostability arises mainly due to efficient electronic relaxation processes which transfer dangerous molecular electronic energy into vibrational molecular energy, faster than the timescale of the damaging chemical reactions. A significant number of photochemical reactions occur on a timescale of the vibrational motion of a molecule. A typical period of a vibrational mode in a molecule is on the order of a hundred femtoseconds (fs), where $1 \text{ fs} = 10^{-15} \text{ s}$. For example, the first step in the photochemistry of vision occurs within only 200 fs [1].

The development of femtosecond lasers has provided science with a unique tool with which to study ultrafast dynamics in photochemistry and photophysics. Ahmed Zewail was the first to directly observe the bond breakage process on a femtosecond timescale [11]. His pioneering work in femtochemistry was recognised by a Nobel Prize award in Chemistry in 1999 [12]. Since this first time-resolved measurement, a number of experimental techniques have been developed and successfully applied to different photochemical problems [1, 13, 14, 15]. The general concept of a femtosec-

ond time-resolved experiment is based on a pump-probe experimental scheme. A reaction is started by a femtosecond pump pulse which creates a non-stationary state or a wavepacket. The evolution of this wavepacket is then monitored by a probe pulse as a function of time delay between the pump and the probe laser pulses.

There are several probe techniques available such as transient absorption, laser induced fluorescence, resonant multiphoton ionisation and time-resolved photoelectron spectroscopies. The choice of the technique depends on the studied problem. This thesis concentrates on the experimental studies of isolated polyatomic molecules in the gas phase. Time-resolved photoelectron spectroscopy has been shown to be a powerful tool for the study of gas phase photochemistry [13, 15, 16] and has been used to perform the pump-probe experiments presented in this thesis.

This chapter provides an introduction to excited state dynamics in isolated molecules followed by a description of wavepacket dynamics and the principles of time-resolved photoelectron spectroscopy (TRPES) and photoelectron angular distribution (PAD) measurements. The chapter concludes with descriptions of several illustrative examples which highlight the scope of TRPES and PAD measurements.

1.1 Photochemistry of polyatomic molecules

1.1.1 Born-Oppenheimer approximation

Due to the low molecular density in the gas phase, it is possible to neglect the interactions between molecules. This allows the properties of isolated molecules to be studied. The description of a stationary isolated molecular system can be obtained from the solution of the time-independent Schrödinger equation [17]:

$$H\Psi = E\Psi, \quad (1.1)$$

where H is the Hamiltonian of the molecular system, Ψ is the wave function of the molecular system, and E is the total energy of the system.

The Hamiltonian of the molecular system can be represented as a sum of the electronic, T_e , and nuclear, T_N , kinetic energy operators and the potential energy of all the particles, V , thus $H = T_N + T_e + V$. Since the mass of the nuclei is three orders of magnitude larger than the mass of the electrons, the motion of the nuclei is much slower than the motion of the electrons. To a first approximation, the fast moving electrons can rapidly adjust to the slow moving nuclear potential while the nuclei experience only the average effect of the electronic field. This fact allows the adiabatic approximation to be used in order to describe a molecular system [17, 18]. In the adiabatic approximation, the total wavefunction of the system, $\Psi_n(\mathbf{r}, \mathbf{R})$, is factorised into the electronic, $\phi_n(\mathbf{r}, \mathbf{R})$, and nuclear, $\chi(\mathbf{R})$, parts:

$$\Psi_n(\mathbf{r}, \mathbf{R}) = \phi_n(\mathbf{r}, \mathbf{R})\chi(\mathbf{R}). \quad (1.2)$$

The electronic wavefunction is obtained by solving the Schrödinger equation with stationary nuclei ($T_n = 0$):

$$[T_e + V(\mathbf{r}, \mathbf{R})] \phi_n(\mathbf{r}, \mathbf{R}) = E_n(\mathbf{R})\phi_n(\mathbf{r}, \mathbf{R}), \quad (1.3)$$

where \mathbf{r} and \mathbf{R} are the electronic and nuclear coordinates, respectively. The nuclear coordinates, \mathbf{R} , are treated as parameters in equation (1.3) and for every value of \mathbf{R} there is a set of n eigenvalues corresponding to the zero-order electronic states, $\phi_n(\mathbf{r}, \mathbf{R})$. The eigenvalues, $E_n(\mathbf{R})$, depend on the nuclear coordinates, \mathbf{R} , and represent the adiabatic electronic potential energy surfaces. The nuclear wavefunction, $\chi(\mathbf{R})$, is then obtained by applying the variation method [17] where the energy of the system has to be minimised with respect to the variable $\chi(\mathbf{R})$ function.

Although the adiabatic approximation provides a good intuitive description of a molecular system, it neglects the couplings between the zero-order electronic states. A more complete description of a molecular quantum system, which relies on the mass difference between the electron and the nuclei, was given by Born and Oppenheimer [18, 19]. Born and Oppenheimer expanded the total Hamiltonian, H , into a power series of $\kappa = \sqrt[4]{m_e/M_N}$, where m_e is the electron mass and M_N is the nuclear mass. The solution for the wavefunction and the energy can also be expanded in a power series of κ :

$$\begin{aligned}\Psi &= \Psi^{(0)} + \kappa\Psi^{(1)} + \kappa^2\Psi^{(2)} + \dots \\ E &= E^{(0)} + \kappa E^{(1)} + \kappa^2 E^{(2)} + \dots,\end{aligned}\tag{1.4}$$

where each wavefunction term, $\Psi^{(i)}$, and energy term, $E^{(i)}$, can be obtained from the corresponding approximation of the Schrödinger equation [19]. This expansion describes the molecular system exactly, however, the series is infinite and must be truncated for practical applications. The zero-order Born-Oppenheimer (BO) equation is equivalent to equation (1.3) and therefore $\phi_n(\mathbf{r}, \mathbf{R})$ are the zero-order BO electronic states. The second to fourth orders describe nuclear vibrations and rotations. The first four orders provide an intuitive separation of the total molecular energy into a sum of the rotational, vibrational and electronic energies of the molecule [20, 21]. The higher order terms describe the coupling between the electronic, vibrational and rotational motions.

1.1.2 Non-adiabatic dynamics

The BO expansion is a perturbative approximation where the non-adiabatic coupling between the zero-order states is assumed to be a minor contribution. Although the adiabatic BO approximation provides a good and intuitive description of many chemical systems [20, 21], it has been shown that in many important cases this approximation breaks down [18, 23, 24, 25, 26]. The break down of the adiabatic BO approximation is especially pronounced in the photochemistry of polyatomic molecules, where a large number of nuclear degrees of freedom are present and electronic states have a small energy separation [27, 28, 29]. In order to analyse multimode vibronic couplings, Domcke *et al.* used the following expansion for the

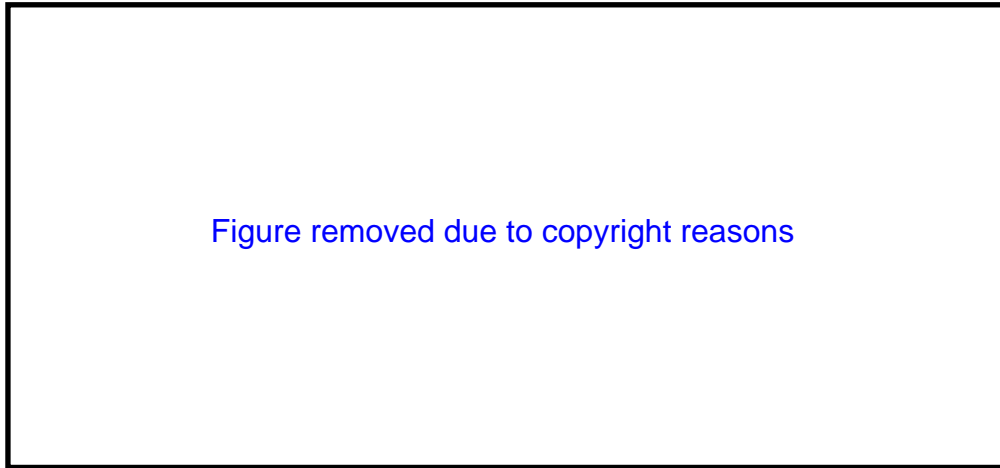


Figure 1.1: Schematic representation of the zero-order BO potential energy surfaces and conical intersections reproduced from reference [22]. After a molecule absorbs a UV photon, it can be photoexcited from the ground electronic state, S_0 , to the electronically excited singlet state, S_1 . A photoexcited wavepacket propagates on the excited potential energy surface and can arrive at a conical intersection (CoIn) between two electronic states where the electronic states become degenerate. At the conical intersection, the wavepacket can either follow the dynamics on the same excited state and form a photoproduct, or diabatically cross to the lower excited state and subsequently may return back to the ground state of the reactant.

exact vibronic wavefunction [27]:

$$\Psi_{\mathbf{r},\mathbf{R}} = \sum_n \phi_n(\mathbf{r}, \mathbf{R}) \chi_n(\mathbf{R}) \quad (1.5)$$

By substituting expansion (1.5) into equation (1.1) the Schrödinger equation can be reduced to:

$$(T_N + E_n(\mathbf{R}) - E) \chi_n(\mathbf{R}) = \sum_m \Lambda_{nm} \chi_m(\mathbf{R}), \quad (1.6)$$

where Λ_{nm} are the vibronic coupling operators:

$$\Lambda_{nm} = \int d\mathbf{r} \phi_n^* [T_N, \phi_m]. \quad (1.7)$$

In the adiabatic approximation, one neglects the vibronic coupling operators, $\Lambda_{nm} = 0$, which leads to an adiabatic wavefunction (1.2). However, the coupling operators, Λ_{nm} , are dependent on the inverse of the energy separation $E_n - E_m$ between two potential energy surfaces [18, 30] and diverge when two adiabatic electronic states become close in energy, thus the adiabatic approximation does not apply. The non-adiabatic effects are especially pronounced when approaching a conical intersection

(CI) between electronic states where two or more adiabatic electronic states become degenerate with respect to one or more nuclear coordinates. The degeneracy induces large non-adiabatic couplings between the vibronic states allowing the population to be transferred from one potential energy surface to another on a femtosecond timescale [14, 29]. An illustrative example of a conical intersection is shown in Figure 1.1.

While presence of a single coupling mode can lead to an avoided crossing between two electronic states, a CI requires at least two modes to be present [27]: a coupling mode, which couples two electronic states, and a tuning mode, which modulates the energy difference between the coupled electronic states. An intra-molecular energy redistribution (IVR) plays an important role in the dynamics near a CI [23, 31, 32]. The high density of the vibrational states near a CI in polyatomic molecules [23] creates a vibrational “bath” which is coupled to the active vibrational modes through the “doorway states” [31, 32]. This coupling provides an efficient electronic energy dissipation into vibrational modes on a femtosecond timescale [33], thus making non-radiative decay *via* a CI an irreversible process.

Although the description of a molecular system near a CI is complicated [18], away from a CI the adiabatic BO approximation provides a good intuitive description of a molecular system. However, even this intuitive description becomes complicated for polyatomic molecules. A molecule that consists of N atoms has $3N - 6$ vibrational degrees of freedom and thus a complete adiabatic potential energy surface has to be presented in $3N - 6$ coordinates. Even a simple polyatomic molecule, such as benzene or its derivatives have 30 or more vibrational degrees of freedom [34]. Due to this complexity, the description of the adiabatic potential energy surfaces is usually simplified to only a few important vibrational coordinates [35]. The choice of the coordinates depends on the process studied. The coordinates may be either the relevant vibrational modes or any combination of these modes which leads to crossing of the potential energy surfaces and/or chemical reactions. For example, in chapter 3 one of the important aniline coordinates is the N–H stretch motion which leads to the molecular dissociation and formation of H atom and anilino products.

1.1.3 Franck-Condon principle

The first step in a photochemical reaction is the absorption of light by a molecule. A photon with a sufficient amount of energy will change the molecular electronic energy on absorption. The change of the electronic energy in this process can be regarded as instantaneous compared to the nuclear motion since the electron is much lighter than the nuclei. The transition rate from a quantum state Ψ_i to a quantum state Ψ_f can be described by Fermi's golden rule which is the result of perturbation theory and includes only a first order perturbation potential V [36]:

$$T_{i \rightarrow f} = \frac{2\pi}{\hbar} |R_{\Psi_i \rightarrow \Psi_f}|^2 \rho_f, \quad (1.8)$$

where ρ_f is the density of the final states and $R_{\Psi_i \rightarrow \Psi_f} = \langle \Psi_f | V | \Psi_i \rangle$ is the perturbation matrix element between Ψ_i and Ψ_f . Some types of electronic transitions can be treated using the Franck-Condon principle [37]. In the frame of the BO approximation where the Schrödinger equation is solved in the molecular frame, the total wave function, Ψ , can be factorised into the electronic and vibrational wave functions, $\Psi_e \Psi_v$. The transition moment from one electronic state $\Psi_{e'v'}$ to another electronic state $\Psi_{e''v''}$ can be written as:

$$R_{\Psi' \rightarrow \Psi''} = \int \Psi_{v'}^* \Psi_{e'}^* \mu \Psi_{e''} \Psi_{v''} d\mathbf{r} d\mathbf{R}, \quad (1.9)$$

where $\mu = \mu_e + \mu_N$ is the operator of the dipole moment which consists of the electronic, μ_e , and nuclear, μ_N , parts:

$$\begin{aligned} R_{\Psi' \rightarrow \Psi''} &= \int \Psi_{v'}^* \Psi_{e'}^* (\mu_e + \mu_N) \Psi_{e''} \Psi_{v''} d\mathbf{r} d\mathbf{R} \\ &= \int \Psi_{v'}^* \left(\int \Psi_{e'}^* \mu_e \psi_{e''} d\mathbf{r} \right) \Psi_{v''} d\mathbf{R} + \int \Psi_{v'}^* \mu_N \left(\int \Psi_{e'}^* \Psi_{e''} d\mathbf{r} \right) \Psi_{v''} d\mathbf{R}. \end{aligned} \quad (1.10)$$

The electron wave functions are orthogonal at any position, \mathbf{R} , and therefore the second term of equation (1.10) is zero. In the Franck-Condon approximation, the electronic transition moment, $R_{e' \rightarrow e''} = \int \Psi_{e'}^* \mu_e \Psi_{e''} d\mathbf{r}$, is assumed to be independent of \mathbf{R} and equation (1.10) can be written as:

$$R_{\Psi' \rightarrow \Psi''} = R_{e' \rightarrow e''} \int \Psi_{v'}^* \Psi_{v''} d\mathbf{R}. \quad (1.11)$$

The transition intensity is proportional to $(\int \Psi_{v'}^* \Psi_{v''} d\mathbf{R})^2$, which is known as the Franck-Condon factor. From equation (1.11), it follows that the transition probability is directly correlated with the vibrational structure of the involved electronic states.

1.1.4 Jablonski diagram

The most common relaxation pathways of the electronically excited isolated molecule can be summarised by a Jablonski diagram, as presented in Figure 1.2. After a molecule absorbs a photon with sufficient energy, it will be promoted to an electronically excited state. The lifetime of the excited state depends mostly on the type of dominant relaxation pathway. The molecule can relax straight back to the ground state by emitting a photon (fluorescence) on a timescale usually of a few nanoseconds. This process often competes with intersystem crossing (ISC) which involves the change of the spin multiplicity from a singlet to a triplet state. The probability of the ISC depends on the spin-orbit coupling between the electronic states. An ISC usually occurs on the nanosecond–millisecond timescale, however, it can be enhanced by the presence of heavy atoms which decrease the ISC timescale [38]. From the excited triplet state, the molecule can emit electromagnetic radiation (phosphorescence) when relaxing back to the ground state.

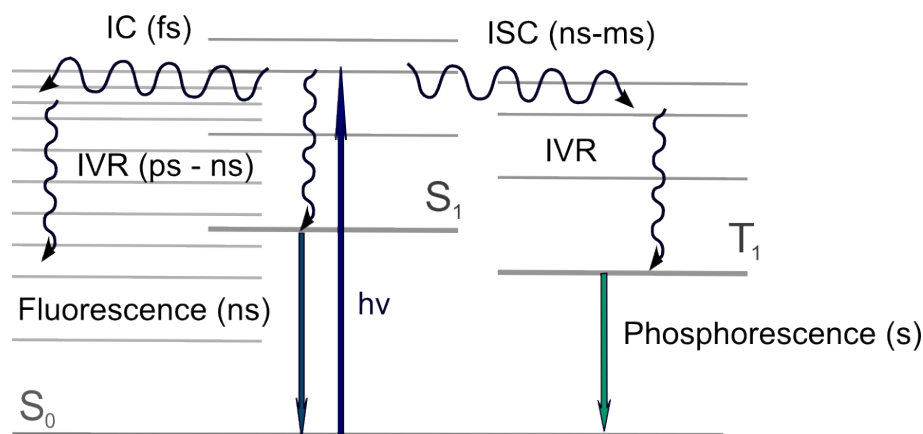


Figure 1.2: Jablonski diagram. Schematic view of the common relaxation pathways available to a molecule after absorption of a photon and promotion of the molecule to an electronically excited singlet state, S_1 . The excited state population can undergo an intersystem crossing bringing the population to a triplet state, T_1 . The molecule can emit electromagnetic radiation from a singlet state (fluorescence) or from a triplet state (phosphorescence). It can also undergo an internal conversion straight back to the ground state. Coupling between the vibrational states leads to intramolecular vibrational energy redistribution. The straight lines represent radiative transitions and the wavy lines represent non-radiative transitions.

Phosphorescence typically occurs on a timescale of seconds. If the molecule has a

lot of excess energy, the coupling between vibrational modes leads to intra-molecular vibrational energy redistribution (IVR) [31, 32]. The singlet electronic state can also relax back to the ground state *via* internal conversion (IC), redistributing the electronic energy amongst the molecular vibrational and rotational degrees of freedom. This process usually happens on a femtosecond timescale [39, 40]. Due to the high density of states at high excitation energies, the non-radiative processes are much faster than the radiative processes. This fact is reflected in Kasha’s rule [41]: *the radiation is usually emitted from the lowest excited level for a given multiplicity*. In addition to the conservative pathways shown in Figure 1.2, which bring the population back to the ground state, the molecule can undergo dissociation [42] or isomerisation [43] to form new chemical products, as shown in Figure 1.1.

1.2 Wavepacket dynamics

Any time-resolved pump-probe experiment is always governed by wavepacket dynamics. A pump-probe experiment consists of three main steps: the excited state preparation, the excited state evolution, and probing of the excited state.

The excited state population of a molecule is prepared by photoexcitation with a laser pulse, $\mathbf{E}_{\text{pump}}(\omega_1)$. The laser pulse has a finite bandwidth which often covers more than a single quantum state. As a result of photoexcitation with the laser pulse, a coherent superposition of excited states or a wavepacket is prepared (see Figure 1.3) [39]:

$$|\Psi(\Delta t)\rangle = \sum_N A_N e^{-iE_N t/\hbar} |N\rangle, \quad (1.12)$$

where A_N are the complex amplitudes of the molecular eigenstates $|N\rangle$ which contain information about the initial phase. The time evolution of every populated state in the wavepacket is contained within the phase factor $e^{-iE_N t/\hbar}$.

After a known time delay, a second laser pulse, $\mathbf{E}_{\text{probe}}(\omega_2)$, interacts with the wavepacket in the excited state and projects the excited state population onto the final state $|\Psi_f\rangle$. The time dependence of the ionisation signal can be expressed as:

$$I_f(t) = |\langle \Psi_f | \mathbf{E}_{\text{probe}}(\omega_2) \cdot \mathbf{d} | \Psi(\Delta t) \rangle|^2 = \left| \sum_N B_N e^{-iE_N t/\hbar} \right|^2, \quad (1.13)$$

where \mathbf{d} is the transition dipole moment and the substitution

$$B_N = A_N \langle \Psi_f | \mathbf{E}_{\text{probe}}(\omega_2) \cdot \mathbf{d} | N \rangle \quad (1.14)$$

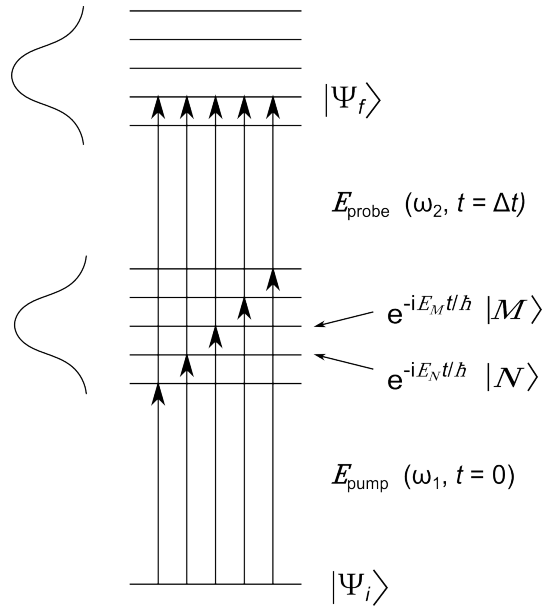


Figure 1.3: Diagram showing preparation and ionisation of an excited state wavepacket. A pump laser pulse \mathbf{E}_{pump} promotes the initial state $|\Psi_i\rangle$ of a molecule into a coherent superposition of excited eigenstates $|N\rangle$. After a known time delay, Δt , the excited state population is projected onto a set of final states $|\Psi_f\rangle$ using a probe laser pulse $\mathbf{E}_{\text{probe}}$.

has been applied. Equation (1.13) can be modified as:

$$I_f(t) = 2 \sum_N \sum_{M \leq N} |B_N| |B_M| \cos(E_N - E_M)t/\hbar + \Phi_{NM}, \quad (1.15)$$

where Φ_{NM} is the phase factor which includes the phase of initial eigenstates, $|N\rangle$ and $|M\rangle$, and the phase of the transition dipole moment between these states and the final state $|\Psi_f\rangle$. As a result of the wavepacket projection using a probe pulse, the resultant signal (1.15) is a coherent sum of all excited state projections on the final state. This signal also contains modulation frequencies $(E_N - E_M)/\hbar$ which are equal to the energy spacing between the eigenstates populated at the instant of ionisation.

In general, every eigenstate has a different overlap with a specific final state. If any of the states have a good overlap with the observed final state, their contribution to the signal is large; if the overlap is poor, the contribution to the observed signal is small. It is therefore important to be able to choose the final state in the pump-probe experiment. In addition, the probe pulse usually generates a set of different final states. Some techniques like total fluorescence or ion yield measurements can detect only the integrated signal from all final states, $I_{\text{tot}} = \sum_f I_f(t)$, and

therefore are unable to distinguish between the final states. Much more information can be acquired with the help of differential detection techniques such as dispersed fluorescence or photoelectron spectroscopy because these techniques can separately detect every final state. The ability to measure the differential signal, $I_f(t)$, is of great importance as the individual excited eigenstates can be disentangled when they have different correlations with the final states, $|\Psi_f\rangle$.

1.3 Time-resolved photoelectron spectroscopy

Time-resolved photoelectron spectroscopy (TRPES), which utilises photoionisation as a probe step, possesses a particular advantage compared to the other techniques - it has the ability to detect any final state, providing the photon energy is sufficient, because the ionisation is always an allowed process (the selection rules for ionisation are relaxed as a result of the range of possible symmetries of the outgoing electron). In addition, it is sensitive to both electronic and nuclear configurations [16, 39], providing a powerful tool for disentangling electronic and vibrational motion. An intuitive picture of a TRPES experiment is provided in section 1.3.1 and the energy correlation between the photoelectrons and the excited states is discussed in section 1.3.2.

1.3.1 Koopmans' picture

A TRPES experiment can be described within Koopmans' picture, shown in Figure 1.4. A pump laser pulse prepares a wavepacket in the zero-order BO electronically excited state S_n . The resulting wavepacket can propagate to another electronically excited zero-order BO state S_{n-1} . In Koopmans' picture, the ionisation process is assumed to remove an outer electron without rearranging the remaining molecular orbitals [44, 45, 46]. Thus, each electronic state of the neutral molecule is directly correlated to a particular final state of the cation.

An example in Figure 1.4 shows that after photoionisation from the initially prepared excited state, S_n , the molecule is left in the cation D_0 electronic state. However, if the excited state population propagates to the intermediate excited state, S_{n-1} , the ionisation pulse leaves the molecule in the cation D_1 electronic state. Therefore, it is possible to say that the two excited states correlate to differ-

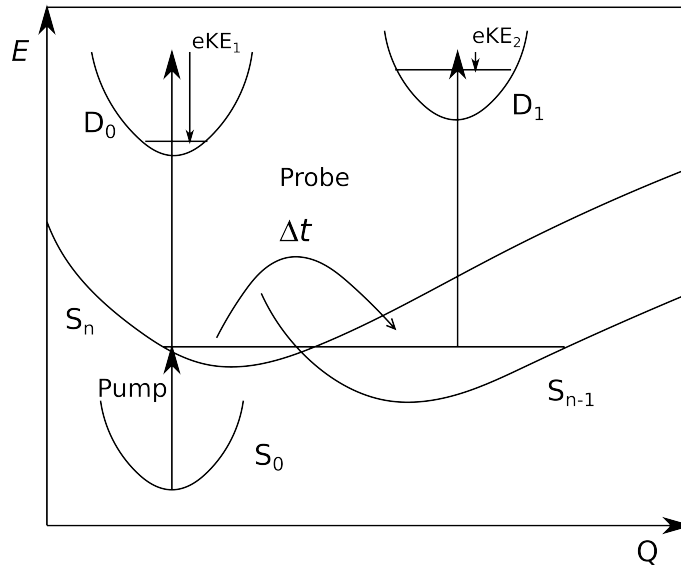


Figure 1.4: A TRPES scheme for disentangling electronic and vibrational dynamics in an excited polyatomic molecule exhibiting Type(I) Koopmans' correlations, e.g. the neutral excited states, S_n and S_{n-1} in this example, correlate to different cation electronic states D_0 and D_1 .

ent ionisation continua and the photoelectrons produced upon the ionisation from these states will have different kinetic energy distributions. This situation describes Type(I) Koopmans' correlation [45]. An example of a TRPES experiment in a system with Type(I) Koopmans' correlation is presented in section 1.5.1. Another possible situation is when both excited states correlate to the same cation state. In this case the excited states can be disentangled in the photoelectron distribution only if their Frank-Condon overlaps with the cation state, given by equation (1.11), are different. This case corresponds to a Type(II) Koopmans' correlation [46]. The photoionisation of the excited states in aniline and DABCO, presented in sections 3.4 and 4.3, correspond to Type(II) Koopmans' correlation.

1.3.2 Energy correlation between excited states and photoelectrons

Figure 1.5 illustrates the relation between the electron kinetic energy distribution, the pump and probe photon energies, and the energies of the molecular states. For simplicity, rotational energies are omitted in the following discussion. A molecule in the ground electronic state, S_0 , has some internal vibrational energy, $E_0(v)$. After absorption of a photon with energy E_{pump} the molecule is promoted into an elec-

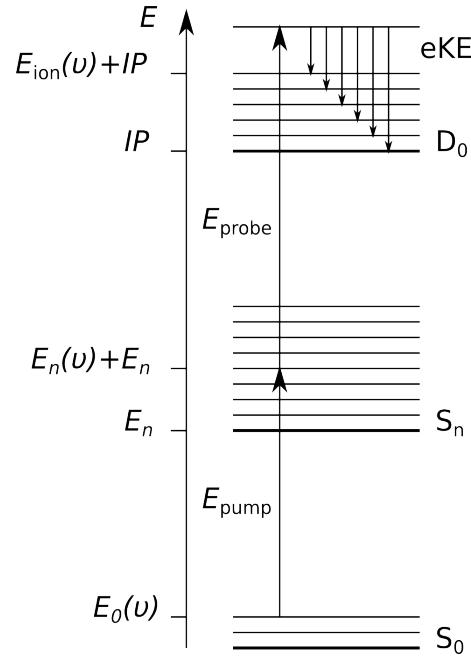


Figure 1.5: A diagram illustrating the relation between all energy components in the pump-probe experiment. E_{pump} and E_{probe} are the energies of the pump and the probe photons, $E_0(v)$, $E_n(v)$ and $E_{\text{ion}}(v)$ are the excess energies in the ground electronically excited and cation states, E_n is the onset of the electronically excited state S_n , IP is the adiabatic ionisation potential to the D_0 cation state, and eKE is the electron kinetic energy.

tronically excited state S_n . The excess energy in S_n , $E_n(v)$, is redistributed amongst the vibrational degrees of freedom. A probe photon with energy E_{probe} ionises the molecule and leaves the ion with some excess energy, $E_{\text{ion}}(v)$, redistributed amongst the vibrations.

According to the energy conservation principle, the following equality must hold:

$$E_0(v) + E_{\text{pump}} + E_{\text{probe}} = IP + E_{\text{ion}}(v) + \text{eKE}, \quad (1.16)$$

where IP is the adiabatic ionisation potential of the molecule. The distribution of the electron kinetic energies can be expressed as:

$$\text{eKE} = E_0(v) + E_{\text{probe}} + E_{\text{pump}} - IP - E_{\text{ion}}(v). \quad (1.17)$$

In a gas phase pump-probe experiment, the molecular rovibrational degrees of freedom are often cooled by the ultrasonic expansion, thus it is reasonable to neglect $E_0(v)$ in equation (1.17). The energies of the pump and the probe laser pulses are always known and therefore, the photoelectron energy distribution is directly related

to the final cation state. After ionisation, the cation vibrational state depends on the vibrational overlap integral in equation (1.11) between the neutral and the cation states. However, in the first approximation, it may be assumed that the vibrational energy does not change much upon ionisation $E_n(v) \approx E_{\text{ion}}(v)$, which is valid when the Franck-Condon factors defined in section 1.1.3 are “diagonal”. This assumption allows us to estimate the relation between the electron kinetic energy (eKE) and the energy of the photoexcited electronic state, E_n :

$$\begin{aligned} \text{eKE} &= E_{\text{pump}} + E_{\text{probe}} - IP - E_{\text{ion}}(v) \\ &\approx E_n + E_n(v) + E_{\text{probe}} - IP - E_{\text{ion}}(v) \\ &\approx E_n + E_{\text{probe}} - IP. \end{aligned} \quad (1.18)$$

Approximation (1.18) works well for the eKE distributions obtained from the electronic states with a Rydberg character (see chapters 3 and 4).

1.4 Photoelectron angular distributions

In addition to the photoelectron energy distribution discussed in section 1.3.2, more information on the excited state dynamics can be obtained from the photoelectron angular distribution (PAD) created during photoionisation [16, 39, 47, 48]. Following symmetry arguments, it is possible to show that any change in the excited state symmetry implies a change in the PAD or ion symmetry obtained during photoionisation [48]. The direct product of the symmetries of the initial state, Γ_i , final state of the molecule, Γ_f , and the electron, Γ_e , and the transition dipole operator, Γ_{dipole} , must contain the totally symmetric representation of the molecular point group, Γ^S :

$$\Gamma_e \otimes \Gamma_f \otimes \Gamma_{\text{dipole}} \otimes \Gamma_i \supset \Gamma^S. \quad (1.19)$$

Further separation of the vibrational, Γ_v , and electronic, Γ_α , symmetry components is possible when applying the Franck-Condon principle [16]:

$$\Gamma_{v_\alpha^\dagger} \otimes \Gamma_{v_\alpha} \supset \Gamma^S, \quad (1.20)$$

$$\Gamma_e \otimes \Gamma_{\alpha^+} \otimes \Gamma_{\text{dipole}} \otimes \Gamma_\alpha \supset \Gamma^S. \quad (1.21)$$

In the case of Type(II) Koopmans’ correlation [46], the ion state configuration, Γ_{α^+} , does not change upon photoionisation and thus the configuration of the excited state, Γ_α , is reflected in the symmetry of the outgoing electron, Γ_e .

The most general expression for the angular dependence of the photoelectron intensity, $I(\theta, \phi)$, originally obtained for nuclear reaction measurements [49], can be written as [47]:

$$I(\theta, \phi) \propto \sum_{L=0}^{L_{\max}} \sum_{M=-L}^L B_{LM} Y_{LM}(\theta, \phi), \quad (1.22)$$

where $Y_{LM}(\theta, \phi)$ is the spherical harmonic of order LM and B_{LM} is the expansion coefficient which depends on the experimental conditions and the photoionisation dynamics. Coefficients B_{LM} are often called the anisotropy parameters because the higher the harmonic order LM , the more anisotropic the angular distribution.

Expansion of the PAD in $Y_{LM}(\theta, \phi)$ is advantageous when describing photoionisation measurements: it is always truncated at a low spherical harmonic order [47]. While most of the information can be obtained from the PAD measurements in the molecular frame [50], many of the measurements are carried out in the laboratory frame (LF). In the pump-probe experiment, the molecular source is often randomly oriented and the LF PAD depends only on the laser polarisation and the molecular orbital configuration from which the electrons are ionised [51]. The L_{\max} value in this case is restricted to $2l_{\max}$, where l_{\max} is the number of photons interacting with the molecular system. Furthermore, if the reflection symmetry is present in the experiment, L must be even. The cylindrical symmetry in the experiment restricts expansion (1.22) further to $M = 0$ only. The cylindrical and reflection symmetries reduce equation (1.22) to the following expression [16]:

$$I(\theta, \phi) \propto \sum_{L=0}^{L_{\max}} \beta_L P_L(\cos \theta), \quad (1.23)$$

where $P_L(\cos \theta)$ is the Legendre polynomial of order L .

A time-resolved photoelectron imaging (TRPEI) experiment is one of the most common techniques used to measure photoelectron energy distributions and LF PADs simultaneously. This technique has been used to acquire the experimental data presented in sections 3.4 and 4.3, and the probe laser pulses must have parallel linear polarisation in the plane of the detector. Therefore, the cylindrical and reflection symmetry conditions were always satisfied for these experiments and equation (1.23) may be used to analyse the LF PADs. The angle θ in this case is measured with respect to the laser polarisation direction.

1.5 Applications of time-resolved photoelectron spectroscopy and imaging

TRPES and TRPEI have been successfully used in a large number of cases as can be seen from the following reviews [13, 14, 15, 16, 39, 47, 52, 53]. Some experimental examples are provided in this section which demonstrate the application of TRPES in a wide range of chemical processes. Firstly, two examples of internal conversion observation are shown in section 1.5.1 with Type(I) and Type(II) Koopmans' correlations, followed by an example of a restricted IVR study in toluene (section 1.5.2). Examples of an intersystem crossing study in aniline and isomerisation study in azobenzene is presented in sections 1.5.3 and 1.5.4. A comprehensive set of information can be obtained using a more complex photoelectron-photoion coincidence imaging technique to study photodissociation, an example of which is described in section 1.5.5.

1.5.1 Internal conversion

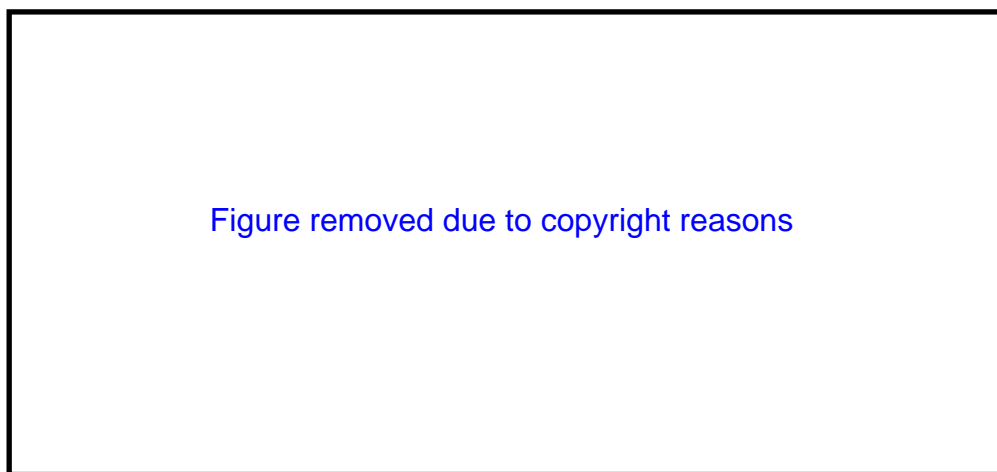


Figure 1.6: Energy level scheme (left) for TRPES of 2,4,6,8-decatetraene (DT) (right). The narrow peak at ε_1 corresponds to ionisation of S_2 to D_0 and the broader peak at ε_2 corresponds to ionisation of S_1 to D_1 . This figure is reproduced from reference [40].

Femtosecond TRPES has been exploited very successfully to observe ultrafast internal conversion (IC) in a number of polyatomic molecules. A classic example is S_2/S_1 IC in the linear polyene all-*trans* 2,4,6,8-decatetraene (DT) [40]. The energy level scheme is presented in Fig. 1.6. The first optically allowed transition is to

the $S_2(1^1B_u)$ state, which is a singly excited configuration, correlating electronically with the $D_0(1^2B_g)$ ground electronic state of the cation. The $S_1(2^1A_g)$ state arises from a configuration interaction between singly and doubly excited configurations and correlates electronically with the $D_1(1^2A_u)$ first electronically excited state of the cation. The photoelectron spectra presented in Fig. 1.6 show a rapid shift in electron distribution ε_1 (ionisation of S_2) to ε_2 (ionisation of S_1) with a ~ 400 fs timescale. This example illustrates Type(I) Koopmans' correlations.



Figure 1.7: Schematic of the TRPES experiment (left) and photoelectron signal components of two electronically excited singlet states S_2 and S_1 (right) in 1,4-diazabicyclo[2.2.2]octane (DABCO). The molecule is photoexcited with 251.1 nm and ionised with 267 nm femtosecond laser pulses. The photoelectron signal of the S_2 component decays on a femtosecond time scale while the S_1 component grows on the same timescale. Both components of the photoelectron signal show a 1.2 ps oscillation period. This graph is reproduced from reference [54].

A TRPES experiment on low lying excited states in 1,4-diazabicyclo[2.2.2]octane (DABCO) [54] is an example where the presence of two electronic states have been revealed by observing a modulation signal in the photoelectron spectrum (see Figure 1.7). The DABCO molecule is promoted to a second electronically excited singlet state, S_2 , *via* single photon absorption at 251.1 nm. An IC between S_2 ($1E'$) and S_1 ($1A_1'$) was observed by ionising the molecule with a 267 nm femtosecond laser pulse at different delay times and monitoring the photoelectron spectrum. Both excited states correlated with the same cation state D_0 . Therefore this experiment is an example of Type(II) Koopmans' correlations. The photoelectron signal from

the S_2 state decays while the photoelectron signal from the S_1 state grows on the same timescale indicating an internal conversion between these states. However, both signals oscillate with a period of 1.2 ps. According to equation (1.15), these oscillations demonstrate the presence of two states with a spacing of 11 cm^{-1} . These states were theoretically confirmed to form, due to the Jahn-Teller interaction near the conical intersection between the S_2 and S_1 states.

1.5.2 Intra-molecular vibrational energy redistribution



Figure 1.8: TRPES following excitation of the $6a^1 + 10b^116b^1$ Fermi resonance in toluene. The oscillations with a period of ~ 6 ps are observed in the photoelectron band around 500 cm^{-1} ion internal energy. These oscillations are out of phase with those observed at zero and 1000 cm^{-1} ion internal energy. This figure is reproduced from reference [55].

TRPES can also be exploited to follow intramolecular vibrational energy redistribution (IVR) in polyatomic molecules. An elegant example is restricted IVR in toluene [55, 56]. The pump pulse prepares a coherent superposition of the $6a^1$ state, corresponding to one quantum of vibrational excitation in the totally symmetric ring breathing mode, and the $10b^116b^1$ state, corresponding to one quantum in the CH_3 wagging mode (10b) and one quantum in the out-of-plane C–H bending mode (16b). As a result of anharmonic coupling between these two states (a Fermi resonance), population flows between them. This is observed as oscillations in the photoelectron spectrum (Figure 1.8). The period of the oscillation is ~ 6 ps and is inversely proportional to the energy separation between the two states in the superposition.

1.5.3 Intersystem crossing

The lowest triplet state in a molecular system is usually located below the first excited singlet state. Therefore, a TRPES study of ISC requires more energetic probe photons than the study of IC. An example of an ISC study in aniline, 2-aminopyridine, and 3-aminopyridine with TRPES, is shown in Figure 1.9. It was already known from phosphorescence studies [57] that an ISC in aniline leads to phosphorescence from the lowest triplet state T_1 . In addition, theoretical studies [58, 59] have predicted that another two triplet states T_2 and T_3 are located below the origin of the S_1 state. However, the role of these triplet states in the S_1 relaxation dynamics was unclear and was the subject of the study [60] described in this example.

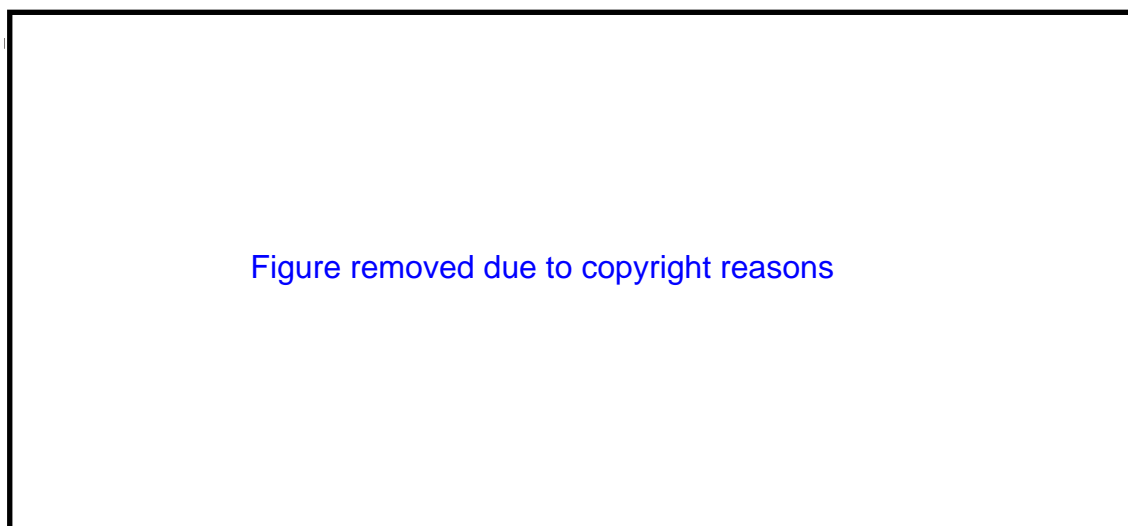


Figure 1.9: Photoelectron spectra following the excitation of aniline, 2-aminopyridine, and 3-aminopyridine to the onset of the S_1 state ($34\,032\text{ cm}^{-1}$ for aniline, $33\,471\text{ cm}^{-1}$ for 2-aminopyridine and $33\,050\text{ cm}^{-1}$ for 3-aminopyridine). The excited states of the molecules were ionised with a 200 nm laser pulse. The delay time between the pump and the probe pulses is $< 50\text{ ps}$ in (a) for all molecules. The pulses were delayed by (b) 8 ns and (c) 13 ns for aniline, (b) 2 ns and (c) 5 ns for 2-aminopyridine, and (b) 0.5 ns and (c) 2 ns for 3-aminopyridine. This figure is reproduced from reference [60].

The aniline, 2-aminopyridine and 3-aminopyridine molecules were initially promoted to their S_1 origin and ionised with a 200 nm delayed pulse. A 200 nm photon has sufficient energy to ionise the lowest triplet state in each molecule. All photoelectron spectra near the zero delay time (Figure 1.9 (a)) show the vibrationally resolved signature of the S_1 state. The photoelectron spectra with delayed probe

pulses show an additional vibrationally unresolved band centred at around 9.2 eV ionisation energy for aniline and 9.5 eV ionisation energy for 2-aminopyridine and 3-aminopyridine. These bands correspond energetically to the ionisation from the lowest triplet state in all molecules. The absence of any other signals in their photoelectron spectra led to the conclusion that there are no other intermediate triplet states involved in the relaxation dynamics of the S_1 state. Thus, the S_1 state is coupled directly to the lowest triplet state in all three molecules.

1.5.4 Isomerisation

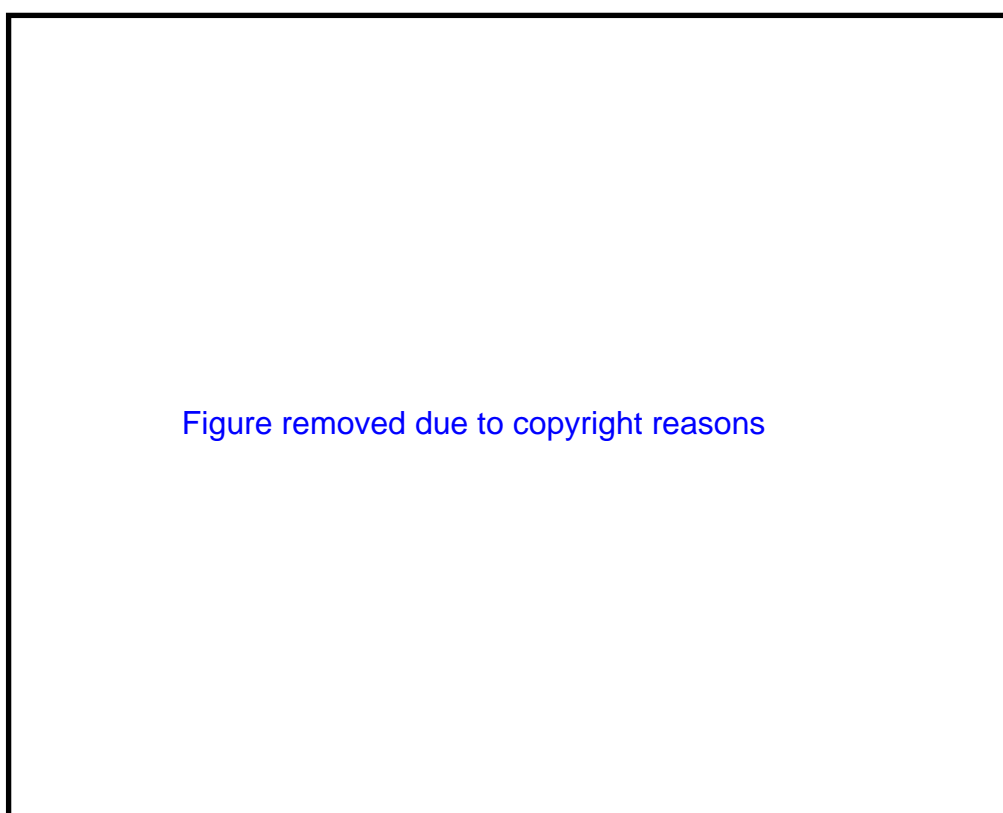


Figure 1.10: (a) The torsion and inversion pathways of the isomerisation dynamics from *trans*- to *cis*-azobenzene. (b) The TRPES of *trans*-azobenzene photoexcited with 330 nm and ionised with 207 nm. Two photoelectron bands correspond to two different excited electronic states which decay on a femtosecond timescale. The two photoelectron bands ε_1 and ε_2 correspond to photoionisation from the $S_2(\pi\pi_{N=N}^*)$ and $S_3(\pi\pi_{\phi}^*)$ electronic states and have decay times of 130 fs and 410 fs, respectively. This figure is reproduced from reference [39].

Another example of a successful application of TRPES is the isomerisation study of azobenzene [43]. Isomerisation of azobenzene is an important example in the study

of molecular electronic switches. There are two possible pathways for isomerisation to proceed from *trans*- to *cis*-azobenzene: through the torsion or inversion motion (Figure 1.10). The total isomerisation yield for the first excited singlet state $S_1(n\pi^*)$ is 25%. According to Kasha's rule [41], the isomerisation should proceed from the lowest singlet state independent of the excitation energy, and therefore the isomerisation yield should be approximately the same when promoting the molecule to other electronically excited states. However, contrary to Kasha's rule, the isomerisation yield decreases to 12% for higher electronically excited states.

A TRPES experiment was performed to study the excited state dynamics when promoting the *trans*-azobenzene molecule to the second electronically excited state $S_2(\pi\pi_{N=N}^*)$ localised on the N=N bond. The TRPES with 330 nm pump pulse and 207 nm probe pulse at different delay times is shown in Figure 1.10. Beside the excitation of the expected $S_2(\pi\pi_{N=N}^*)$ state (ε_1), the data reveals a direct excitation of a new previously unknown electronically excited singlet state (ε_2) which was theoretically confirmed to be the $S_3(\pi\pi_\phi^*)$ state. This state has a very close energetic location to the $S_2(\pi\pi_{N=N}^*)$ state but has different Koopmans' correlation, resulting in a different photoelectron energy distribution. The $S_3(\pi\pi_\phi^*)$ state has a different electronic configuration and is localised on the phenol ring. For this reason this state has a different relaxation pathway compared to the $S_2(\pi\pi_{N=N}^*)$ state. Based on theoretical calculations it was concluded that the phenyl-ring dynamics of the $S_3(\pi\pi_\phi^*)$ state provide a relaxation pathway directly to the ground *trans*-azobenzene state, thus reducing the isomerisation yield. The complexity of the information obtained from the TRPES experiment allowed the discovery of the previously unobserved electronic state which solved the question of the reduced isomerisation yield.

1.5.5 Photodissociation

A sophisticated variant of TRPEI, time-resolved photoelectron-photoion coincidence imaging spectroscopy, has been demonstrated to be a powerful tool for unravelling the mechanisms of photodissociation, as illustrated in reference [50]. A schematic energy level diagram is presented in Figure 1.11: a femtosecond 209.6 nm pump pulse promotes the dimer to an electronically excited state, $(NO)_2^*$, and a femtosecond 279.5 nm probe pulse ionises the initially excited state, the photodissociation product, $NO(A\ 3s)$, and intermediate states (represented by the grey box).

Figure removed due to copyright reasons

Figure 1.11: Schematic energy level diagram of the pump-probe scheme for investigating $(\text{NO})_2^* \rightarrow (\text{NO})_2^{**} \rightarrow \text{NO}(\text{A } 3s) + \text{NO}(\text{X})$ (left). TRPES (middle right) together with photoelectron spectra at $t = 0$ and $t = 3500$ fs (top right) and the time-evolution of the photoelectron signal with electron kinetic energies 9.66 eV and 10.08 eV (bottom right). This figure is reproduced from reference [50].

When the pump and the probe pulses are overlapped ($\Delta t = 0$), the photoelectron spectrum is broad due to photoionisation from $(\text{NO})_2^*$, whereas at long pump-probe time delays, the photoelectron spectrum is narrow due to photoionisation from the free $\text{NO}(\text{A } 3s)$ photoproduct. It is not possible to fit the data using a single exponential decay for $(\text{NO})_2^*$ and an equivalent rise for $\text{NO}(\text{A } 3s)$. Instead, the data is fit to a two-step sequential model where $(\text{NO})_2^*$ decays with a time constant of around 590 fs in some intermediate state and the intermediate state subsequently decays on a timescale of about 140 fs, forming a $\text{NO}(\text{A } 3s)$ product.

In order to identify the intermediate state, $(\text{NO})_2^{**}$, the momentum distributions of both the photoelectrons and photoions were recorded in coincidence (Figure 1.12). Importantly, measurement of the photoelectron momentum in coincidence with the recoiling photofragment allowed measurement of the PAD in the frame of the recoiling photofragment. Since this photofragmentation was a rapid process, the recoil frame PAD was equivalent to the molecular frame PAD, albeit averaged over rota-



Figure 1.12: The photoelectron angular distributions (PADs) are shown in the laboratory and the recoil reference frames at different time delays as labeled in the figure. The recoil frame PAD shows a time-dependent strong anisotropy. The fitted curves (solid lines) include up to 8th order Legendre polynomials. In contrast, the lab frame PAD is featureless and time independent. The evolution of the $3p_y$ contribution to the recoil PAD (bottom right) agrees well with the time evolution of the intermediate state obtained from the TRPES measurements. The direction of the laser polarisation is also shown in the bottom right. This figure is reproduced from reference [50].

tion about the recoil axis. These experiments, supported by *ab initio* calculations, revealed that the pump pulse excites a vibrationally excited state of $(\text{NO})_2^*$ which evolves towards an intermediate state with $3p_y$ Rydberg character, which correlates with the $\text{NO}(A\ 3s) + \text{NO}(X)$ photodissociation channel.

1.6 Conclusions

In this chapter, the basic principles of non-adiabatic dynamics in polyatomic molecules were discussed followed by a description of TRPEI - a powerful technique for unravelling these non-adiabatic dynamics. This technique has been used to study the femtosecond dynamics of the small organic molecules aniline and 1,4-diazabicyclo[2.2.2]octane (DABCO) which are the main subjects of this thesis. Chapter 2 provides an overview

of the experimental toolkit for TRPES and TRPEI. Chapter 2 also contains a description of the experimental setups and data analysis procedure used to study non-adiabatic dynamics in aniline and DABCO. The experimental results from TRPEI studies of aniline and DABCO are presented in chapter 3 and chapter 4, respectively.

Chapter 2

Experimental toolkit

An overview of the experimental tools available for pump-probe time-resolved photoelectron imaging experiments is presented in the first three sections of this chapter. Sections 2.4 and 2.5 describe the experimental apparatus used for performing the experiments presented in chapter 3 and chapter 4. Data processing and key experimental procedures are covered in section 2.6. The analysis of the time resolved photoelectron spectra is discussed in section 2.7.

2.1 Femtosecond light sources

Virtually all polyatomic molecules have strong absorption bands in the ultraviolet (200 – 350 nm) and ionisation potentials in the vacuum ultraviolet (VUV) (< 200 nm). The most common form of TRPES employs an ultraviolet (UV) pump pulse to access low-lying electronically excited states and a UV probe pulse to ionise the molecule from these excited states and generate photoelectrons with electron kinetic energies in the range 0 – 3 eV. Generally, it is not possible to ionise a molecule that has returned to its electronic ground state using a UV probe pulse, since the molecule will have considerable excess vibrational energy and there is a $\Delta v = 0$ propensity for photoionisation. Photoionisation of molecules that have returned to the electronic ground state by non-radiative decay from electronically excited states, usually requires a VUV probe pulse to access higher vibrational states in the ionisation continuum [15, 61]. Extreme ultraviolet (XUV) probe pulses (< 120 nm) allow the additional possibility of ionising core electrons; photoelectrons generated by photoionisation of the valence electrons will have much higher electron kinetic energies than the core electrons.

Most TRPES experiments employ commercial femtosecond laser systems that are tunable in the UV. Femtosecond laser technology is a research field in itself, and there are many excellent reviews available, see for example [62, 63]. The most common scheme for the production of femtosecond UV pulses is based on a Ti:Sapphire laser operating at around 800 nm. A bandwidth of around 100 nm can be achieved, enabling the production of pulses as short as 10 fs. The Ti:Sapphire crystal is usually pumped using a continuous laser with an output wavelength around 525 nm. The femtosecond pulses from the Ti:Sapphire oscillator are used to seed a chirped pulse regenerative amplifier; before amplification, the seeding pulses are stretched to a few hundreds of picoseconds to avoid non-linear processes and damage in the gain medium. Single pass amplifiers can be used to increase the pulse intensity further. After amplification, the amplified pulses are compressed back to durations of a few tens of femtoseconds. The amplifier is usually pumped by a nanosecond laser operating around 525 nm.

Harmonics of the fundamental output of the Ti:Sapphire amplifier can be obtained by second harmonic generation (SHG) and sum-frequency generation (SFG) processes in β -barium borate (BBO) crystals generating pulses around 400 nm,

267 nm and 200 nm [64, 65]. Optical parametric amplifiers (OPAs) [66, 67, 68] are employed to generate femtosecond pulses that are tunable in the visible and IR. In an OPA, the fundamental output of the Ti:Sapphire amplifier is focused onto a suitable transparent media to generate a white light continuum [68, 69], which is then mixed with the fundamental in a BBO crystal, providing tunable light in the range 1150 nm to 2630 nm through optical parametric amplification. Generation of femtosecond pulses throughout the UV to around 235 nm can be obtained by combination of OPA with nonlinear optics (SHG, SFG and difference frequency generation (DFG)). Ti:Sapphire based femtosecond laser systems were used for the experiments presented in chapter 3 and chapter 4. A more detailed descriptions of these setups is presented in sections 2.4 and 2.5.

The duration of a laser pulse is limited to the cycle of the laser field, which for 800 nm is 2 – 7 femtoseconds but can be less than a hundred attoseconds in the XUV [70, 71]. Attosecond XUV pulses are produced by high harmonic generation (HHG) in nonlinear gases [62]. In principle, it is possible to use any gas for HHG, however the ionisation potential of the atom or molecule has to be high enough for the HHG to compete with multiphoton ionisation. The energy range and intensity profile of the XUV spectrum depends on the gas: in Ar, the spectrum ranges from 10 eV (125 nm) to around 100 eV (12.5 nm). An XUV monochromator or filters can be used to select the photon energy range for the experiment. The efficiency of HHG is usually relatively low ($\sim 10^{-6}$) yielding photon fluxes of around 10^8 photons per pulse [62]. XUV laser sources have sufficient photon energy to ionise the ground-state of any molecule, but they also have sufficient photon energy to ionise inner valence electrons, which promises to yield complementary information [15, 72].

Free electron lasers (FELs) can produce very short laser pulses with high photon energy and high brilliance [73]. FELs work by generating high quality electron pulses which are accelerated to relativistic energies and compressed to femtosecond duration before being fed into an undulator. The periodic trajectory of the electrons in the magnetic field of the undulator results in the emission of synchrotron radiation. Due to the interaction between the emitted radiation and the electrons the radiation is amplified coherently, thus, producing coherent electromagnetic radiation with a mean photon energy that is controlled by the electron energy and the undulator parameters. There are several international FEL facilities in the world, which include the European soft x-ray FEL, Free-Electron Laser in Hamburg (FLASH) [74] and the

USA x-ray FEL (XFEL), the Linac Coherent Light Source (LCLS) [75]. The FLASH facility generates laser pulses in the wavelength range 6.8 nm to 47 nm and pulse durations from 10 fs to 70 fs. The LCLS facility operates in the wavelength range from 0.15 nm to 2.2 nm with pulse durations from 70 fs to 500 fs. The intensity of these XUV and x-ray free electron lasers (XFELs) is currently as high as 10^{13} photons per pulse, which is several orders of magnitude larger than those obtained using XUV HHG sources. A new XFEL facility is currently under development in Hamburg, Germany. This European project aims to achieve even higher photon intensities in the wavelength range from 0.1 nm to 6.2 nm.

The relationship between pulse duration and spectral bandwidth for Gaussian pulses is restricted by the inequality,

$$\Delta\nu \cdot \Delta t \geq 0.441, \quad (2.1)$$

which can be rewritten as,

$$\Delta\lambda[\text{nm}] \geq 1.471 \times 10^{-3} \frac{\lambda^2[\text{nm}^2]}{\Delta t[\text{fs}]}, \quad (2.2)$$

where $\Delta\nu$ is the spectral width (FWHM), $\Delta\lambda$ is the bandwidth (FWHM) at wavelength λ , and Δt is the pulse duration (FWHM) of the Gaussian laser pulse. Equation (2.1) stipulates that it is not possible to have infinitely good spectral resolution and time resolution simultaneously. The timescales for non-adiabatic processes range from tens of femtoseconds to hundreds of picoseconds. From equation (2.2), we see that the bandwidth of a 100 fs pulse at 250 nm is around 1 nm (equivalent to around 20 meV or 150 cm^{-1}) and the bandwidth of a 0.1 fs pulse at 15 nm is around 3 nm ($> 10 \text{ eV}$). Thus, planning a TRPES experiment requires careful consideration of the requirements for the photoionisation wavelength alongside the achievable temporal and spectral resolution.

Another important aspect of a TRPES experiment is the delay between the pump and probe laser pulses. This is usually controlled by changing the path length between the two pulses using optics mounted on commercial translation stages. In UV-UV and UV-VUV/XUV pump-probe experiments, the pump and probe laser pulses generally both originate from the same oscillator, which keeps the jitter well below the temporal resolution of the translation stage (typically around 0.01 fs). However, in pump-probe experiments using XFELs, UV pump and x-ray probe pulses do not have the same origin and the jitter may be significant [76].

2.2 Molecular sources for gas phase measurements

In order to make time-resolved photoelectron spectroscopy measurements of isolated molecules, an expansion into a vacuum chamber is usually employed ensuring a collision-free environment. Such conditions also allow for the stringent requirements of most electron detectors which place an upper limit of around 10^{-5} mbar in the laser-molecule interaction region.

The simplest way to deliver a gas sample into the laser-molecule interaction region is to feed it through a thin capillary. The gas will expand into the vacuum chamber with the highest density close to the capillary tip. Such a source is reasonably well collimated at close distances [77]. The effusive molecular source was used during the experiments performed at Rutherford Appleton Laboratory and presented in chapter 4.

A more efficient way to deliver a gas sample into the laser-molecule interaction region is with a supersonic molecular beam. The gas is usually delivered through a nozzle, which is a sealed tube with a 50–500 μm hole. The source chamber housing the nozzle is usually separated from the laser-molecule interaction region by a molecular skimmer with a diameter of a few millimetres, generating a high density, well-collimated molecular beam [78]. Such molecular beams have small transverse velocity and very low velocity spread in the propagation direction [79]. This reduces the number of molecules in the interaction region which have been thermalised through collisions with the chamber walls and scattered back into the interaction region. In addition, when a carrier gas is used, the expansion process cools down vibrational and rotational motions in the molecules often leading to spectral simplification. The cooling effect is a function of the nozzle diameter, the gas pressure behind the nozzle and the carrier gas [80, 81]. The rotational temperatures of the molecules are efficiently cooled down to the translational temperatures of the carrier gas due to the “velocity slip” effect if heavy carrier gas (for example Ar) is used [80]. The vibrational cooling in supersonic expansion is less efficient due to the poor vibrational-translational interaction cross-section and the vibrational temperatures of the molecules are usually much higher than the rotational temperatures. A liquid nitrogen cold trap is often placed after the laser-molecule interaction region to absorb scattered molecules that pass through the interaction region. This type of nozzle was used for the experiments described in chapter 3.

During a TRPES experiment the laser-molecule interaction occurs for only a tiny fraction of the total time of the experiment, defined by the laser pulse duration and laser repetition rate. Therefore, most of the gas from a continuous nozzle source does not interact with the laser. The efficiency can be improved significantly by using a pulsed nozzle. The pressure behind the pulsed nozzle can be as high as 100 bar whilst maintaining reasonable vacuum conditions in the photoelectron spectrometer. Such high pressures can produce very efficient cooling; for example, Even-Lavie pulsed nozzles can cool large molecules to rotational temperatures below 1 K [82].

A more recent development is TRPES of liquid samples. Liquid jets were first developed to study evaporation of molecular monomers and dimers [83]. For TRPES in liquids, the key component is a quartz glass liquid nozzle with an aperture size around 10 μm which generates a continuous flow of liquid; after travelling a few millimetres in the vacuum the liquid jet breaks into droplets which are collected in a trap [84]. Liquid jets have been employed successfully in UV-VUV/XUV [85] and UV-UV [86] TRPES experiments.

2.3 Photoelectron spectrometers

There are several different techniques for measuring photoelectron spectra. The most popular photoelectron spectrometers are based on velocity map imaging (VMI) or time of flight (ToF) methods.

ToF spectrometers measure the photoelectron spectrum by analysing the time taken for an electron to travel from the interaction region to a detector. The simplest ToF electron spectrometers are field free with a very low collection efficiency ($\sim 10^{-4}$) [87]. A much better collection efficiency of ToF spectrometers is achieved by introducing electrostatic or magnetic fields to guide the electrons to the detector. A commonly employed ToF spectrometer is the magnetic bottle electron spectrometer [88] which has the advantage of a large collection efficiency (typically 50%). Photoelectrons created in the molecule-laser interaction region are guided in a magnetic field toward the electron detector which is usually a microchannel plate. ToF spectrometers can be constructed to have high energy resolution over a wide range of photoelectron energies which is particularly useful for experiments using VUV or x-ray probe pulses. Obtaining information about photoelectron angular distributions from ToF measurements is more challenging, requiring ToF spectrometers

with small solid angles of collection (and so low collection efficiency) and repeated measurements with different experimental geometries.

Velocity map imaging (VMI) allows both the photoelectron spectrum and the photoelectron angular distribution to be measured simultaneously. VMI is based on using static electric fields to project the 3D photoelectron momentum distribution created in the molecule-laser interaction region onto a 2D photoelectron image in the plane of the electron detector [89]. The position sensitive electron detector usually comprises a microchannel plate, a phosphor screen and a charge-coupled device. The original 3D photoelectron momentum distribution can be reconstructed from 2D photoelectron image using an inversion algorithm such as an inverse Abel transform [90]. The energy resolution of a VMI apparatus depends on the electron detector resolution as well as on the focussing properties of the electrostatic lens. Energy resolution as low as $\Delta E/E = 0.38\%$ can be achieved [91]. VMI spectrometers were used for both experiments presented in chapter 3 and chapter 4.

2.4 UCL experimental setup

2.4.1 Femtosecond laser system

A commercial laser system from Coherent was used to provide femtosecond laser pulses with tunable wavelength. Figure 2.1 shows a schematic view of the UCL femtosecond laser system used for the experiments presented in chapter 3. The Ti:Sapphire oscillator (Coherent Mira) is pumped by a continuous wave (CW) 5 W laser at 532 nm (Coherent Verdi). The lasing wavelength of the Ti:Sapphire crystal can be varied around the optimum position of 785 nm by changing the length of the cavity. A passive mode-locking process, based on the optical Kerr effect, is used to produce femtosecond pulses. The oscillator generates femtosecond pulses with a bandwidth of about 40 nm and 1 W average power at a repetition rate of 100 MHz. The output pulses have a duration of about 25 fs. These pulses are used to seed a regenerative amplification cavity.

Before the actual amplification, the seeding pulses are temporally stretched using a grating and collimation optics. Stretching is required for reduction of the pulse intensity in order to avoid nonlinear processes and damage in the gain medium which are very likely to occur under the standard laser power and pulse durations. A

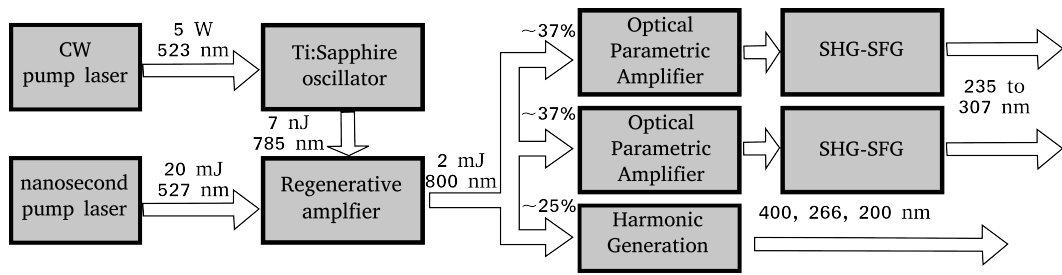


Figure 2.1: Schematic diagram of the UCL femtosecond laser system. A Ti:Sapphire based oscillator is pumped by a CW 523 nm laser. The output of the oscillator is seeded into the regenerative amplifier to gain more pulse power. Amplified pulses are split and seeded into OPAs to generate laser pulses with tunable wavelength in the UV region.

Ti:Sapphire crystal is used as the gain medium of the regenerative amplifier (Coherent Legend). The crystal is pumped by a nanosecond 527 nm Nd:YLF laser (Coherent Evolution) at a frequency of 1 kHz. The seed pulse is introduced into the cavity by switching a Pockels cell. The timing of the Pockels cell is controlled externally. After several rounds of oscillations through the crystal, an amplified pulse is released from the cavity by another Pockels cell which is triggered externally. The timing of the Pockels cells is tuned to optimise the number of round trips in the cavity in order to obtain maximum laser power and minimise material dispersion. The amplified pulse is then compressed back to a femtosecond duration. The optimised cavity produces an output laser power of approximately 2 mJ per pulse after compression. The resultant amplified laser pulse, with a wavelength of about 800 nm, is then split using beamsplitters into pulses used for pumping an optical parametric amplifier (OPA), harmonic generation or in beam diagnostics.

2.4.2 Nonlinear optics

Nonlinear processes induced by high intensity electric fields in a transparent media are used in a wide range of optical applications including frequency upconversion [64, 65, 68] and laser diagnostics [92, 93]. These processes are also utilised in extending the wavelength range obtained from the Ti:Sapphire laser. The induced dielectric polarisation of the medium, \mathbf{P} , can be expanded into a power series with respect to the electric field, \mathbf{E} :

$$\mathbf{P} = \sum_n \varepsilon_0 \chi^{(n)} \mathbf{E}^n = \varepsilon_0 (\chi^{(1)} \mathbf{E} + \chi^{(2)} \mathbf{E}^2 + \dots), \quad (2.3)$$

where ε_0 is the permittivity of free space and $\chi^{(n)}$ are the electric susceptibilities of the medium. The dielectric polarisation can be approximated as a linear function of the electric field at low laser intensities, however, at high laser intensities higher order contributions become important. The electric field of the laser beam of frequency ω can be expressed as:

$$\mathbf{E} = \mathbf{E}_\omega e^{i\omega t}. \quad (2.4)$$

By substituting expression (2.4) into expansion (2.3) the harmonic series is obtained:

$$\begin{aligned} \mathbf{P} &= \sum_n \varepsilon_0 \chi^{(n)} \mathbf{E}_\omega^n e^{in\omega t} \\ &= \varepsilon_0 (\chi^{(1)} \mathbf{E}_\omega e^{i\omega t} + \chi^{(2)} \mathbf{E}_\omega^2 e^{i2\omega t} + \chi^{(3)} \mathbf{E}_\omega^3 e^{i3\omega t} + \dots). \end{aligned} \quad (2.5)$$

The first term in equation (2.5) corresponds to the fundamental harmonic, the second term corresponds to the second harmonic, and so on. Thus the nonlinear response of the medium to the electric field generates higher order harmonics. If two different electric fields with frequencies ω_1 and ω_2 pass through a transparent medium the second order nonlinearity gives rise to a new frequency $\omega_3 = \omega_1 + \omega_2$. Crystals that are transparent to the incident electromagnetic radiation are often used to exploit nonlinear processes. The efficiency of this nonlinear frequency conversion in crystals is defined by the phase matching conditions $\mathbf{k}_3 = \mathbf{k}_1 + \mathbf{k}_2$ and can be tuned by rotating the optical axis of the crystal.

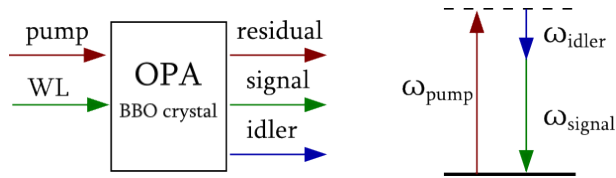


Figure 2.2: Schematic view of the optical parametric amplification process. The pump photons of frequency ω_{pump} are converted into the signal and idler photons due to the second order nonlinearity of dielectric polarisation of the crystal with respect to the laser field at high laser intensities. The frequencies of the signal and idler satisfy energy conservation principle $\omega_{\text{pump}} = \omega_{\text{signal}} + \omega_{\text{idler}}$. The process is seeded by a white light (WL) and the wavelength is determined by the phase matching between the polarisation of the fields to satisfy the momentum conservation $\mathbf{k}_{\text{pump}} = \mathbf{k}_{\text{signal}} + \mathbf{k}_{\text{idler}}$. By tuning the crystal axis the phase matching conditions for different signal frequencies can be satisfied.

Inside the OPA the 800 nm laser pulse is split into three beams. The first beam

Table 2.1: Available wavelength ranges from the Coherent OPAs used at UCL.

| Origin | Wavelength, nm |
|---------------------------|----------------|
| Fundamental | 800 |
| Idler | 1600 - 2630 |
| Signal | 1150 - 1600 |
| SFG (idler + pump) | 533 - 613 |
| SFG (signal + pump) | 472 - 533 |
| SFG (idler + pump) - SHG | 267 - 307 |
| SFG (signal + pump) - SHG | 236 - 267 |
| SHG idler | 800 - 1150 |
| SHG signal | 575 - 800 |
| FHG idler | 400 - 575 |
| FHG signal | 300 - 400 |

is focused into a sapphire crystal where white light is generated [68]. The white light then passes collinearly with the second 800 nm beam through the β -BaB₂O₄ (BBO) crystal. By adjusting the temporal overlap between the pulses from each beam, and the crystal angle, the phase matching conditions between the pump pulse and different wavelengths of the white light can be satisfied. As a result, signal and idler pulses are produced which satisfy the following condition:

$$\omega_{\text{pump}} = \omega_{\text{idler}} + \omega_{\text{signal}}. \quad (2.6)$$

This process is called optical parametric amplification and it is a three wave mixing process. Following the optical parametric amplification, the signal and idler are reflected back and pass collinearly with the third 800 nm beam through the BBO crystal where they are further amplified. Either the signal or the idler can be used to further generate a desirable wavelength by using optional modules including second (SHG) and fourth harmonic generation (FHG), sum frequency generation (SFG), and difference frequency generation (DFG). Table 2.1 summarises all available wavelengths from the OPAs used at UCL.

2.4.3 Layout of the laser setup

The time delay between the pump and the probe laser pulses, Δt , is controlled by a translation stage, schematically shown in Figure 2.3. The time delay is related to the

stage displacement, Δx , as $2\Delta x = \Delta tc$, where c is the speed of light. The coefficient 2 appears due to the double pass of the light along the stage. The translation stage can move with a precision of better than $0.1 \mu\text{m}$, thus providing a time resolution better than 1 fs. The pump and the probe laser pulses originate from the same initial laser source and thus, the time drift between them is well below the femtosecond scale.

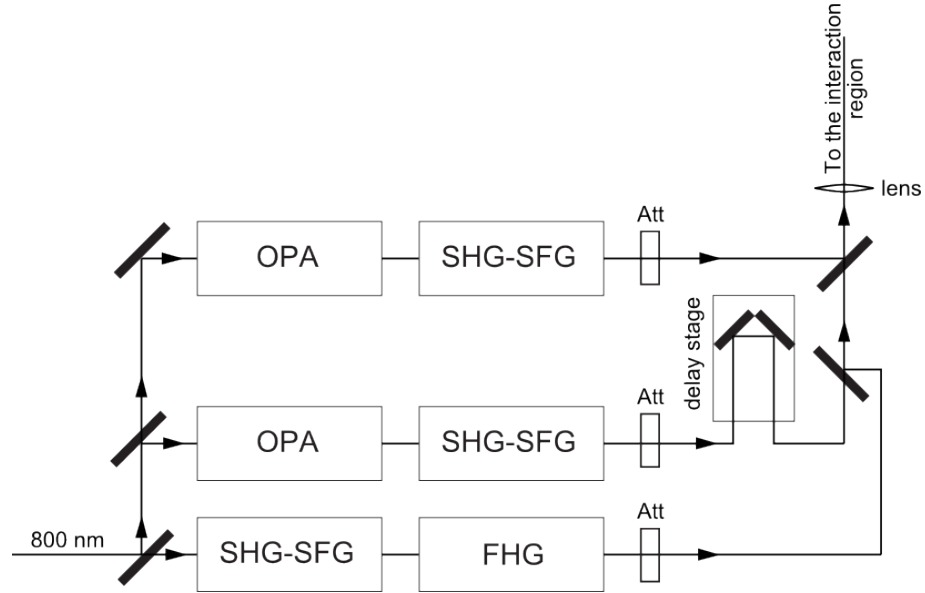


Figure 2.3: Layout of the UCL femtosecond laser setup. The 800 nm fundamental is delivered from the Coherent Legend laser system shown in Figure 2.1. A tunable wavelength in the UV range down to 235 nm is obtained from commercial Coherent OPA systems. Up to the fourth harmonic of the fundamental 800 nm is obtained using Coherent SHG, SFG and FHG systems. The laser intensity is varied by a diffractive variable attenuator (Att). The delay between the laser pulses is controlled by a translation stage installed into the laser beam pass. The laser pulses are recombined using a UV beam splitter and focused into the interaction region with a fused silica lens.

The intensity of the laser pulses is controlled by diffractive variable attenuators. Typical pulse intensities of about $0.5 \mu\text{J}$ per pulse at the lens position are used in the experiments described in chapter 3. The laser pulses were recombined either by a 50/50 beam splitter or a narrow bandwidth mirror reflecting one pulse and transmitting the other. After recombination, the pulses are focused into the interaction region by a fused silica lens with 250 mm focal length.

2.4.4 Vacuum system

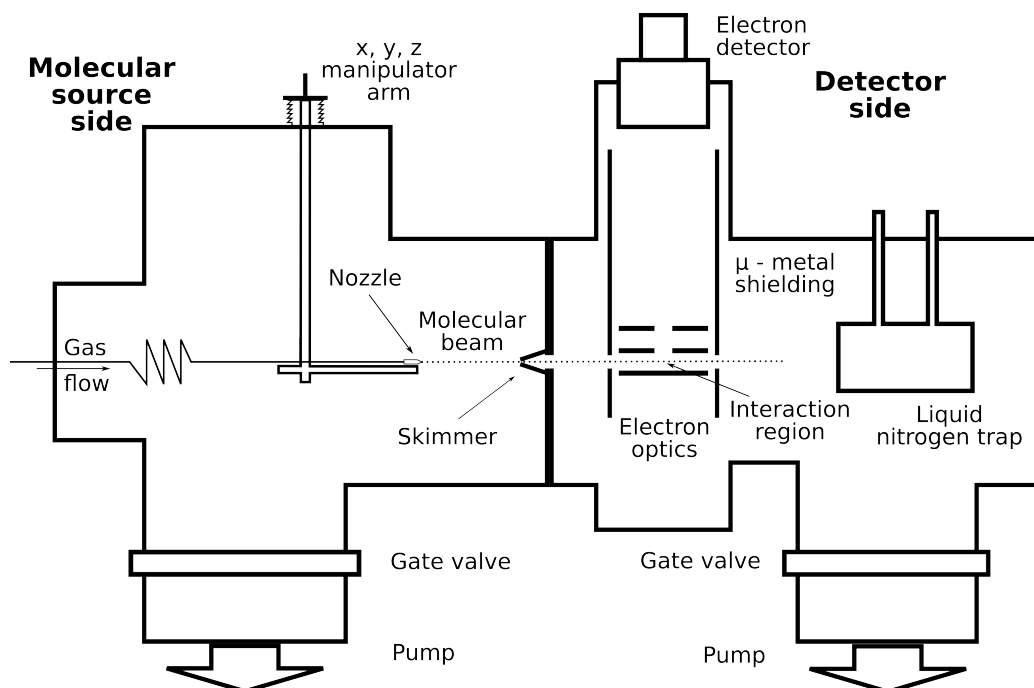


Figure 2.4: Schematic view of the UCL vacuum system used for the experiments presented in chapter 3. The molecular source side is separated from the detector side by a 1 mm skimmer. The molecular beam passes through the skimmer into the interaction region between the velocity map imaging electron optics. Photoelectrons produced in the interaction region are focused into the electron detector. After passing through the interaction region, molecules freeze to the surface of a liquid nitrogen trap. Typical operating pressures in the interaction region are 2×10^{-8} mbar without gas flow and 8×10^{-8} mbar with gas flow.

The schematics of the vacuum system used for the experiments presented in chapter 3 are shown in Figure 2.4. The vacuum chamber consists of two parts: the molecular source chamber and the photoelectron detector chamber. The molecular source part of the chamber includes a gas delivery 1/16 inch tubing with a CW nozzle on the end. The diameter of the nozzle can be varied, however, for the experiments described in chapter 3 the nozzle diameter was always $50 \mu\text{m}$. The nozzle is mounted on a x, y, z–manipulator arm which allows precise 3D alignment of the pointing of the molecular beam. The source part of the vacuum chamber is separated from the interaction region by a molecular skimmer. A skimmer with a 1 mm diameter hole was used to create sufficient differential pumping between the two chambers. The molecular beam passes through the skimmer and through a hole in the μ -metal

shielding into the interaction region between the electron optics. Photoelectrons produced in the interaction region are focused by the velocity map imaging electron optics onto the detector (see Figure 2.5 for details). The flight path of the electrons is shielded by μ -metal in order to suppress any magnetic fields produced by turbo pumps or vacuum gauges. After the interaction, the molecules pass through the μ -metal shielding and are trapped on the metal surface of the liquid nitrogen tap. Both chambers were evacuated separately by turbo pumps backed by rotary pumps. The vacuum in the detector chamber is about 2×10^{-8} mbar without the gas flow and maintained below 10^{-7} mbar during the experiment.

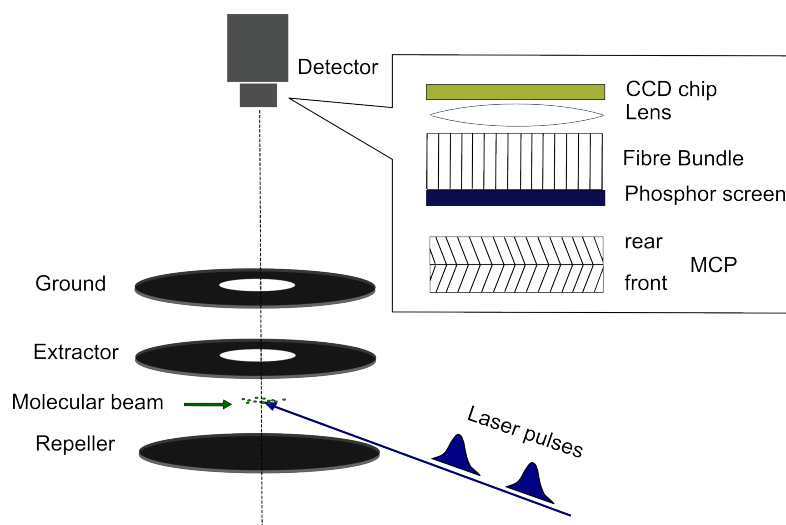


Figure 2.5: Schematic view of the velocity map imaging detector used for the experiments presented in chapter 3. The electron optics consist of the repeller, extractor and ground plates. The interaction volume is located between the repeller and extractor. The photoelectrons are focused onto the electron detector which includes micro-channel plates (MCP), phosphor screen, magnification lens and CCD camera. The front MCP is grounded while the rear MCP is kept under 1.5 kV. A 4.5 kV potential is applied to the phosphor screen. In order to reduce the background counts an additional pulsed voltage of 0.3 kV with a duration of $2 \mu\text{s}$ is applied to the rear MCP. The camera and the pulsed MCP voltage are synchronised with the laser pulses by using the common trigger with the Coherent Legend amplifier.

After photoionisation with a probe laser pulse, ionised electrons are focused on to the detector using the electric lens (Figure 2.5). The lens system has cylindrical symmetry and consists of three electrodes: a repeller, an extractor and a ground. The molecular beam is ionised between the repeller and the extractor where the

electrons are accelerated towards the electron detector. The repeller and extractor electrode potentials are set to produce the best velocity resolution at the detector plane. The voltage ratio between the repeller and the extractor for the best velocity resolution is always constant for a given detector geometry [89]. The magnitude of the repeller and extractor potentials determine the electron velocity (energy) range which can fit onto the detector. A commercial detector VID240 produced by Photek company was used for the electron velocity measurements. The detector consists of a micro-channel plate (MCP), a phosphor screen and a charge-coupled device (CCD). During the first stage, electrons are multiplied in the MCP; afterwards they are converted into photons in a phosphor screen which are then detected by a CCD camera. A double layer MCP is used in this system with a gain range of 10^5 to 10^7 . The transverse resolution of the MCP, together with the phosphor screen, is 20-30 line pairs per millimetre. The Photek detector uses a Basler A312f CCD camera which has a coupled magnifying lens with a magnification factor of 2, and a 782x582 pixel resolution CCD chip with 8 μm square pixels.

2.5 RAL experimental setup

2.5.1 Femtosecond laser system

The experiments reported in chapter 4 were conducted at the Artemis facility at the Rutherford Appleton Laboratory. The pump and probe laser pulses were derived from a 1 kHz Ti:Sapphire chirped pulse amplification (CPA) system (KM Labs Red Dragon) operating at 800 nm and delivering less than 30 fs pulses with 14 mJ pulse energy [94]. The output of this laser system was split to produce synchronised pump and probe pulses (see Figure 2.6). Tunable pump pulses in the region 233.9–251.1 nm were generated using a commercial OPA (Lightwave HE-TOPAS) and subsequent frequency mixing producing pulses with a duration of 40–50 fs and pulse energies up to 35 μJ . Probe pulses at 400 nm were obtained by frequency doubling the output of the CPA system. For experiments employing a two-photon probe process, the output of the CPA system was used directly. The pump and probe pulse energies were reduced to < 100 nJ using polarisers and half-wave plates, as needed. The pump and probe pulses were recombined using an uncoated fused-silica flat mirror with the UV pump pulse derived from the front surface (4%) reflection,

and the probe pulse transmitted through the mirror. Under these conditions, on average, less than one electron was produced per laser shot. The pump-probe time delay was adjusted using motorised delay stages under computer control. The laser beam was focused with a concave mirror of 250 mm radius of curvature.

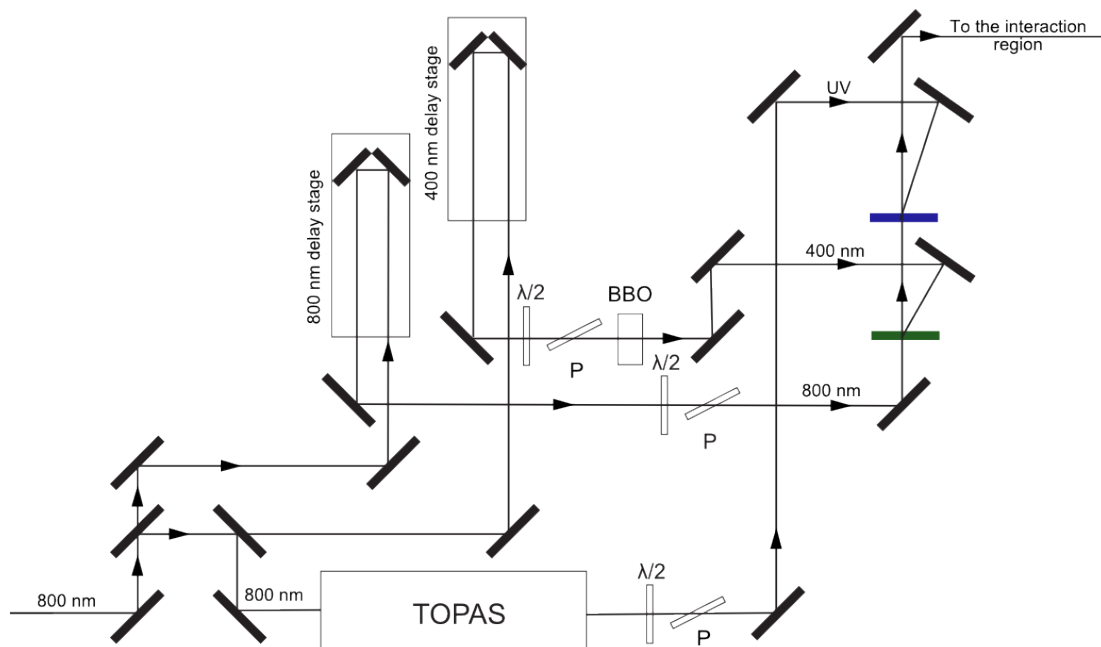


Figure 2.6: Schematic view of the laser setup used for the experiments described in chapter 4. The 800 nm fundamental is delivered from the KM Labs Red Dragon CPA laser system. A tunable wavelength in the UV range was obtained from commercial OPA (Lightwave HE-TOPAS). A BBO— β -BaB₂O₄ crystal was used for the second harmonic generation. A set of half-wave plates ($\lambda/2$) and polarisers (P) were used to adjust the laser power for each beam arm.

2.5.2 Vacuum system

The vacuum system is similar to the one described in Figure 2.4, however, there were a few major differences. There was no separation between the molecular source and the detector regions. An effusive inlet was used to deliver DABCO vapour to the interaction region and it was placed as close to the interaction region as possible, without disturbing the focusing of the VMI detector, to insure maximum molecular density in the interaction region. The liquid nitrogen trap was absent. A VMI spectrometer was equipped with a time and position sensitive delay line anode detector (Roentdek DLD40) for measurement of the photoelectron spectra and angular distributions. The operational principle of the detector is shown in Figure 2.7 [95].

The electron signal is amplified by a double stack of MCPs multiplying the electron signal by about 10^7 before it hits the delay line. The detector has two delay lines to allow detection of electron hit position in two coordinates (X, Y). After each electron hit, the signal arrival times are recorded (X_1, X_2, Y_1, Y_2). The electron position information (X, Y) is encoded in the difference between the signal arrival times at both ends of the delay line:

$$\begin{aligned} X &= X_1 - X_2 \\ Y &= Y_1 - Y_2. \end{aligned} \quad (2.7)$$

The multi-hit dead time of the detector is 10 – 20 ns which is longer than the spread in the electron arrival times from a single laser shot. Thus, only a single electron event per laser shot could be detected. All multiple events had to be discarded during data processing. The sampling time step of the time to digital converter is 25 ps.

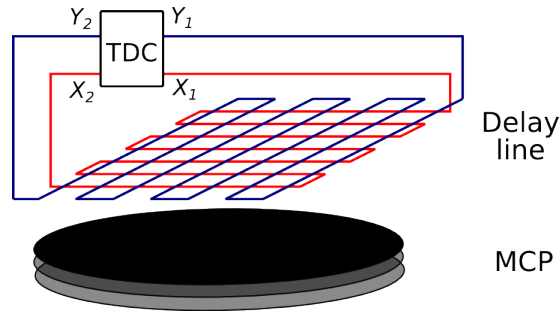


Figure 2.7: Schematic view of the Roentdek delay line anode detector. The detector is equipped with a double stack of MCP plates and a position sensitive delay line. The signal from the delay line is fed into a time to digital converter (TDC), before each event is processed and stored on the computer.

The detector was triggered by a photo-diode which detected the fundamental 800 nm laser pulses, thus the detector was synchronised with the laser pulses. The delay line signals were recorded and saved for every trigger event. The following data processing steps were applied to every trigger event in order to eliminate multiple hit events and other data acquisition noise:

1. All events with $X = 0$ and $Y = 0$ were discarded.
2. For a single hit event, the total signal travel times, $X_1 + X_2$ and $Y_1 + Y_2$, depend only on the wire length and must fit in a certain time window t_w .

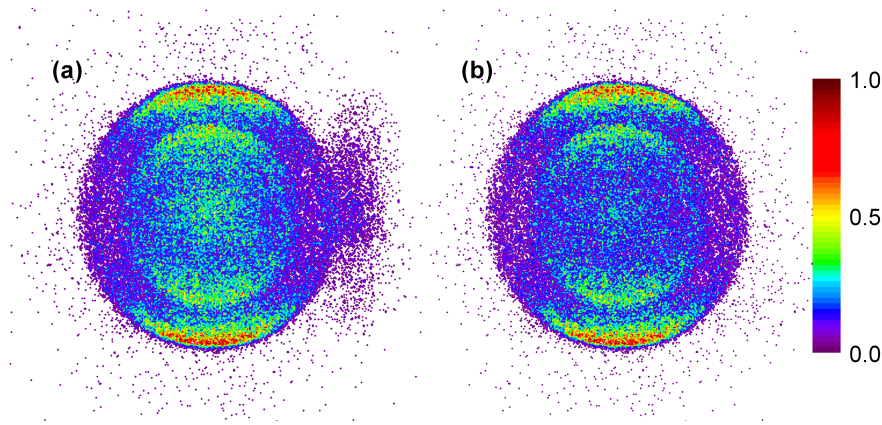


Figure 2.8: (a) Raw image and (b) processed image obtained from the delay line anode detector. The noise events on the right and in the centre of the image are removed by the image processing. The processing procedure is described in the text.

Therefore the time window conditions must be satisfied $t_1 > X_1 + X_2 > t_2$ and $t_1 > Y_1 + Y_2 > t_2$, where $t_2 - t_1 = t_w$ and t_1 is defined by the trigger delay. The trigger delay is dependent on the photodiode position and was varied during the course of the experiment. The optimum time window, t_w , was determined to be 7 ns.

The result of the image processing is shown in Figure 2.8. The original noisy image (Figure 2.8 (a)) is successfully improved by the image processing (Figure 2.8 (b)), described above.

2.6 Experimental procedures and diagnostics

This section covers the experimental procedures required to obtain photoelectron spectra from a VMI spectrometer as well as some important diagnostic routines. Figure 2.9 summarises the main steps in the processing of the experimental images. Firstly, the raw data obtained from the detector was filtered in order to eliminate possible noise. Afterwards, a 3D velocity map image is obtained by applying the inverse Abel transform to the processed image. The energy scale of the detector is then obtained from the calibration procedure.

The procedure for processing the delay line anode images (RAL setup) is described in section 2.5.2. Processing of images from the Photek detector (UCL setup) was performed directly by the Photek software during data acquisition. When an electron hits the detector, it produces an oversized phosphorescence image on the

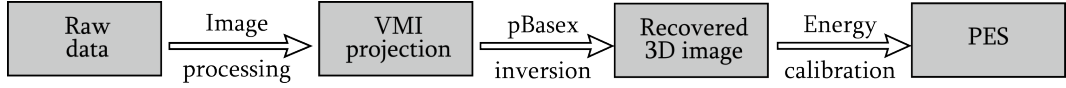


Figure 2.9: Flow chart of the processing procedure for data from the VMI spectrometer.

CCD camera covering several pixels, which is due to the limited MCP and phosphor screen resolution. In addition, the light intensity from a single electron hit fluctuates. To overcome these issues, the Photek data acquisition software records the average position of such a group of pixels as a single hit.

The pBasex algorithm was used to perform the Abel inverse transform for all the data presented in chapters 3 and 4. This algorithm is described in section 2.6.1. The energy scale of the detector must be calibrated for every VMI voltage settings and each time after any changes in the experiment geometry are made (for example nozzle realignment). The calibration procedure is described in section 2.6.2.

2.6.1 VMI reconstruction

All the experimental data presented in this thesis is acquired with the velocity map imaging (VMI) detectors. The first important step in the analysis of the VMI data is to reconstruct the three dimensional (3D) electron momentum distribution from the two dimensional (2D) projection obtained from the detector. The imaging system has a static electric field which focuses electrons such that the electron velocity is proportional to the position of the electron on the image sphere at the detector plane, shown in Figure 2.10 ($\mathbf{v} \propto \mathbf{r}$ and $E_{kin} \propto |\mathbf{r}|^2$). This sphere is projected onto a position sensitive detector. Thus, the imaging system projects a 3D electron momentum distribution $F(r, \theta, \phi)$ onto the 2D plane of the detector (r', θ') . In this case, the radial position on the detector is proportional to the component of the electron velocity parallel to the detector plane ($\mathbf{v}_{\mathbf{r}} \propto \mathbf{r}'$).

If the original 3D velocity distribution contains cylindrical symmetry with respect to the detector plane, the electron momentum distribution becomes independent of ϕ , and the electron distribution in the detector plane, $P(r', \theta')$, can be expressed as:

$$P(r', \theta') = 2 \int_{|r' \sin \theta'|}^{\infty} \frac{x F(r, \theta)}{\sqrt{x^2 - (r' \sin \theta')^2}} dx. \quad (2.8)$$

Equation (2.8) is known as the Abel transform of a function $F(r, \theta)$. There is no

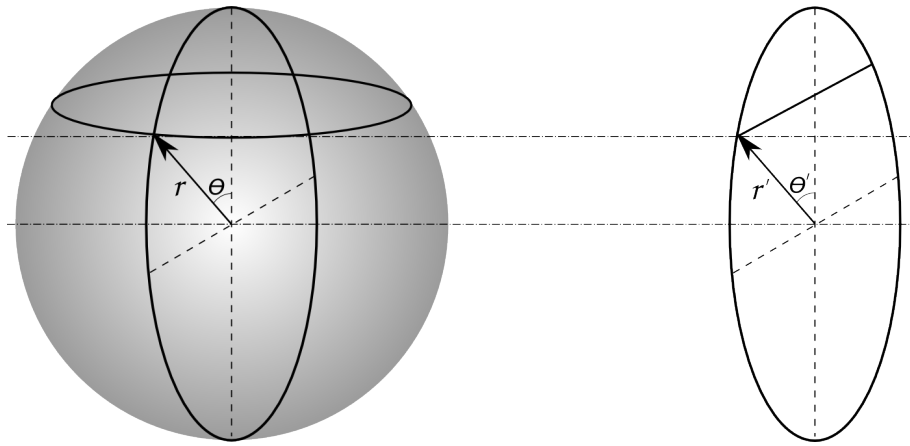


Figure 2.10: Photoelectron imaging scheme. The 3D electron velocity distribution (left hand side) is projected onto the 2D detector plane (right hand side).

algebraic solution for the inverse Abel transform when the $P(r', \theta')$ distribution is known and the distribution $F(r, \theta)$ has to be found. However, it is possible to use numerical mathematical methods to reconstruct the distribution $F(r, \theta)$. Several techniques are available to perform the reconstruction which are discussed in reference [90] along with analyses of their performance. This section focuses on two methods developed recently: 1) polar basis function expansion (pBasex) [96] and 2) polar onion-peeling (POP) [97]. The pBasex algorithm was used for all the analysed data presented in this manuscript.

The pBasex technique is based on the BASEX algorithm [98], however, it uses a polar coordinate system for the detector plane instead of Cartesian coordinates. The method represents a 3D velocity distribution as an expansion in a well-behaved basis set $\{f_{k, l}(r, \phi, \theta)\}$ where (r, ϕ, θ) are the spherical coordinates. The velocity distribution must have cylindrical symmetry and, thus, be independent of ϕ . Angle θ is measured with respect to the polarisation direction in the case of linearly polarised light. The choice of the basis set has some restrictions in order to avoid numerical instabilities during computation. The recommended basis set of the original 3D distribution for the pump-probe experiment is:

$$f(r, \theta)_{k, l} = e^{-(r-r_k)^2/\sigma^2} P_l(\cos \theta), \quad (2.9)$$

where r_k represents the centre of the k -th Gaussian, σ is the Gaussian coefficient and $P_l(\cos \theta)$ is the Legendre polynomial of the l -th order. In practice the expansion has to be limited to some maximum values k_{\max} and l_{\max} , ($k = 0, \dots, k_{\max}$ and

$l = 0, \dots, l_{\max}$). The advantage of the algorithm is good performance and the smallest systematic error amongst the available methods. However, the basis set (2.9) has to be converted into the polar coordinates of the detector plane which requires numerical integrations. The procedure is very time consuming and usually is performed in advance for the particular basis set with defined values k_{\max} and l_{\max} . The higher the dimension of the basis $k_{\max} \times l_{\max}$, the longer it takes to calculate the basis set and the more memory is required.

A recent version of the POP algorithm also operates in polar coordinates [99]. In contrast to pBasex, this method does not require *a priori* knowledge of the basis set. The procedure starts from the outermost ring of the 3D distribution and calculates its contribution to all inner rings in the 2D image. The contribution is then subtracted from the whole image and the procedure is repeated for all rings until it reaches the innermost ring. The POP algorithm does not artificially smooth the noise compared to the predefined basis set approach employed in pBasex. In addition, the new POP algorithm borrows the idea of the basis functions from BASEX in order to improve the performance of the algorithm. However, the size of the basis depends only on the resolution of the detector (resolution of the CCD chip) and it has to be generated only once.

2.6.2 VMI energy calibration

A VMI spectrometer projects the velocity distribution of the photoelectrons in the interaction region onto the spatial coordinate of the electron detector, producing a velocity map image. After the inverse Abel transform, the velocity spectrum of the photoelectrons can be recovered from the image (see section 2.6.1). The electron velocities are proportional to the distance on the electron detector $v \propto r$, thus the original data obtained from the VMI detector is a velocity spectrum in arbitrary velocity units. The energy spectrum has to be obtained from the velocity distribution. For non-relativistic electrons, the relation between their velocity, v , and energy, E , can be expressed as following:

$$E = \frac{m}{2}v^2 = ar^2, \quad (2.10)$$

where m is the electron mass, r is the position on the detector and a is the calibration factor. However, the calibration factor depends on the detector geometry and VMI voltages and has to be determined experimentally. Thus, the absolute energy scale

of the VMI detector requires calibration of the detector using a known photoelectron distribution. For this purpose, a photoelectron spectrum of Xe or NO can be used to calibrate the detector.

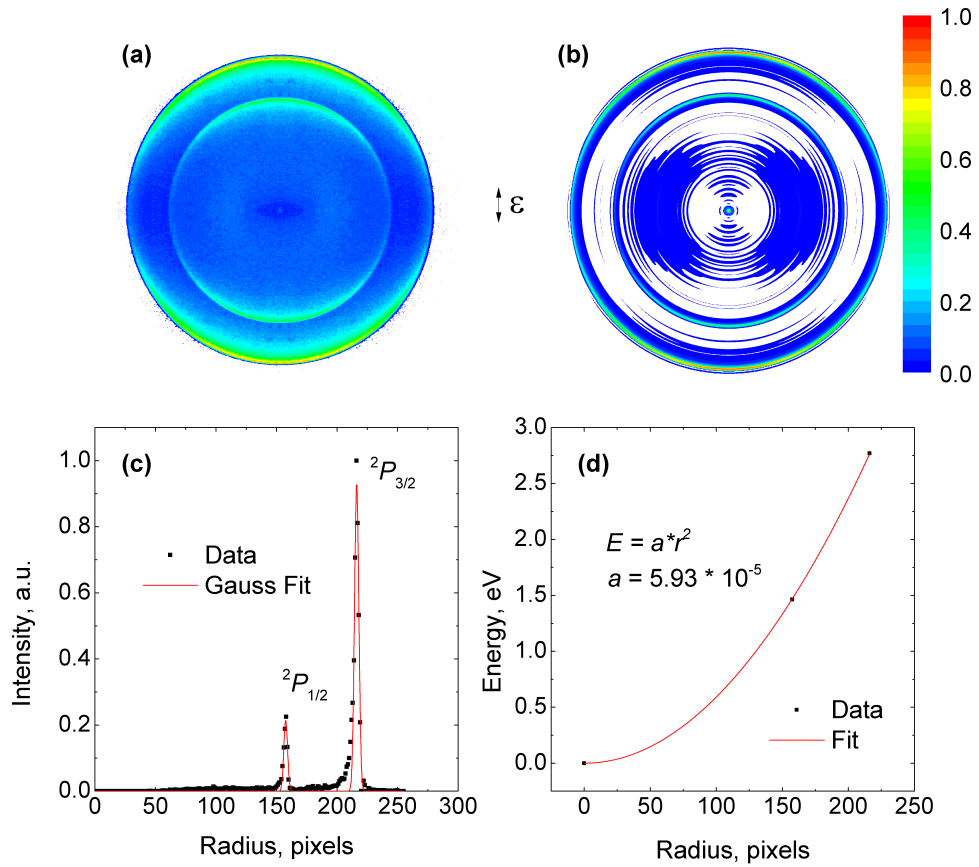


Figure 2.11: (a) An example of a velocity map image of 2+1 REMPI ionisation of Xe at 249.63 nm *via* a 6p Rydberg resonance accessible with two 249.63 nm photons, (b) inverted VMI with pBasex, (c) velocity spectrum obtained from the inverted image and (d) energy calibration curve. The photoelectron peaks at 1.46 eV and 2.76 eV correspond to ionisation to $^2P_{1/2}$ and $^2P_{3/2}$ cation energy levels. The repeller and extractor voltages in this case were -3000 V and -2095 V, respectively.

Xe has two well-known ionisation energies, $\text{Xe}(^1S_0) \rightarrow \text{Xe}^+(^2P_{3/2})$ with an IP of 12.13 eV and $\text{Xe}(^1S_0) \rightarrow \text{Xe}^+(^2P_{1/2})$ with an IP of 13.437 eV. Usually three UV photons are required to ionise Xe, due to its high ionisation potential. The ionisation cross-section of Xe significantly increases when ionisation proceeds through one of the Xe intermediate excited states. An example of the energy calibration with Xe is shown in Figure 2.11. Xe atoms were ionised with a 249.63 nm laser pulse *via* a 6p Rydberg resonance located at 9.93 eV, producing two photoelectron peaks at

1.46 eV and 2.76 eV. The calibration coefficient, a , is obtained from the fit of the experimentally determined peak radii on the detector and the known photoelectron energies to equation (2.10).

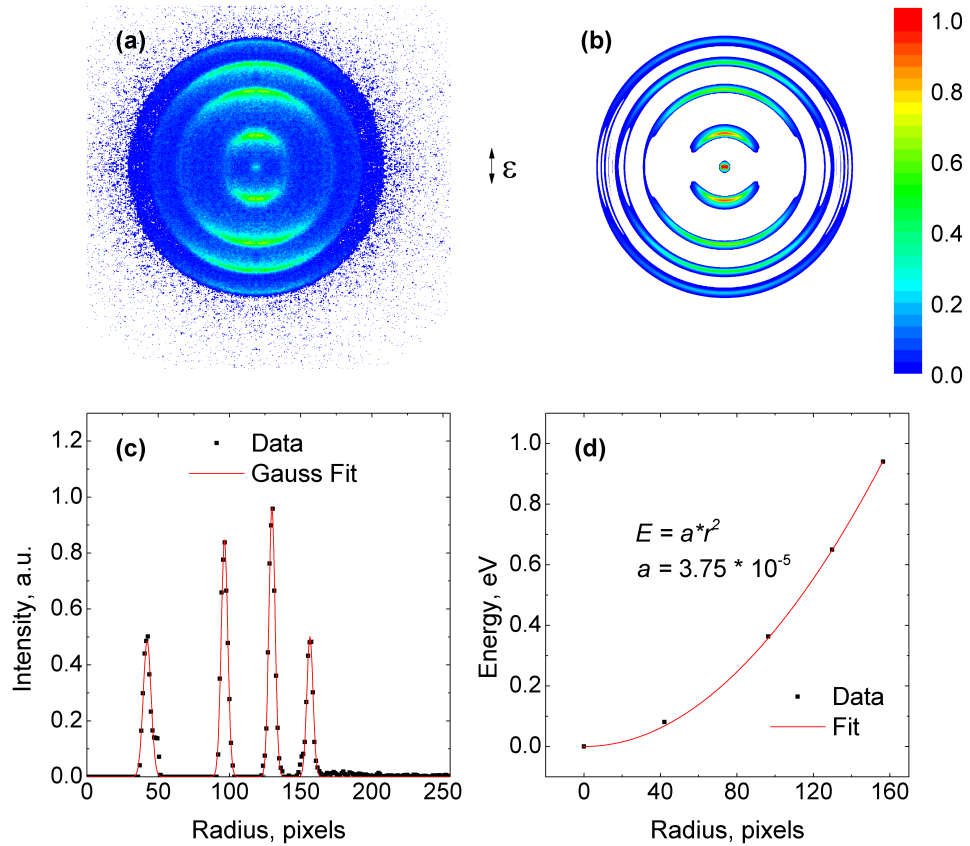


Figure 2.12: (a) Velocity map image of 1+1 non-resonant ionisation of NO at 243 nm, (b) inverted velocity map image with pBasex, (c) velocity spectrum obtained from the inverted image and (d) energy calibration curve. The repeller and extractor voltages in this case were -2500 V and -1783 V, respectively.

Another possible candidate for the calibration of the detector energy scale is nitric oxide (NO). After ionisation, nitric oxide ions (NO^+) can be left in the ground vibrational state or any of the vibrational excited states. The adiabatic IP of NO is 9.26 eV. The vibrational energy spectrum of NO^+ is well known and it can be used for energy calibration. The first six vibrational energy terms are shown in table 2.2. The number of photoelectron peaks in the NO ionisation energy spectrum depends on the photon energy. An example of the energy calibration using a 1+1 ionisation spectrum of NO with a 243 nm laser pulse is shown in Figure 2.12.

The detector energy range depends on the repeller and extractor voltages, how-

| v^+ | G_{v^+}, cm^{-1} | G_{v^+}, eV | E_e, eV |
|-------|---------------------------|----------------------|------------------|
| 0 | 1184.14 | 0.1468 | 0.94 |
| 1 | 3528.04 | 0.4374 | 0.65 |
| 2 | 5839.41 | 0.7240 | 0.36 |
| 3 | 8118.26 | 1.0065 | 0.08 |
| 4 | 10364.58 | 1.2850 | — |
| 5 | 12578.38 | 1.5595 | — |

Table 2.2: NO^+ vibrational energy terms and photoelectron energies after a two photon ionisation of NO with 243 nm laser pulse. Only the first four cation vibrational energies were accessible with 243 nm photons.

ever, the best VMI focusing conditions are satisfied at certain $V_{\text{rep}}/V_{\text{extr}}$ ratio for any given detector geometry. It is important to mention that a VMI detector geometry includes the position of the interaction region which can be modified after the alignment of the molecular beam (nozzle). Thus, the energy calibration has to be performed each time the nozzle alignment is changed. The energy resolution can be estimated from the full width half maximum (FWHM) of the photoelectron peaks. The dependence of the FWHM of two photoelectron peaks from the Xe spectrum as a function of extractor voltage is shown in Figure 2.13. The best focusing conditions

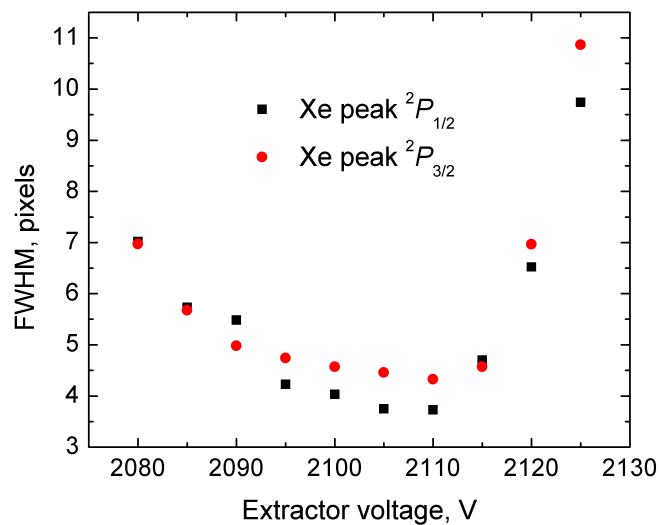


Figure 2.13: FWHM of two photoelectron peaks from the Xe spectrum as a function of the extractor voltage. The repeller voltage was constant and set to -3000 V.

produce photoelectron peaks with a radial FWHM, Δr , of 4 pixels. The following equation can be used to obtain the energy width of the photoelectron peak:

$$\Delta E = 2ar\Delta r. \quad (2.11)$$

For example, the energy width of the $^2P_{1/2}$ photoelectron peak, shown in Figure 2.11 (c), is estimated to be 70 meV. The width of the photoelectron peak depends on several factors: the laser bandwidth, the focusing of the VMI optics, the resolution of the photoelectron detector, and the inverse Abel transform algorithm.

2.6.3 Pump-probe cross-correlation

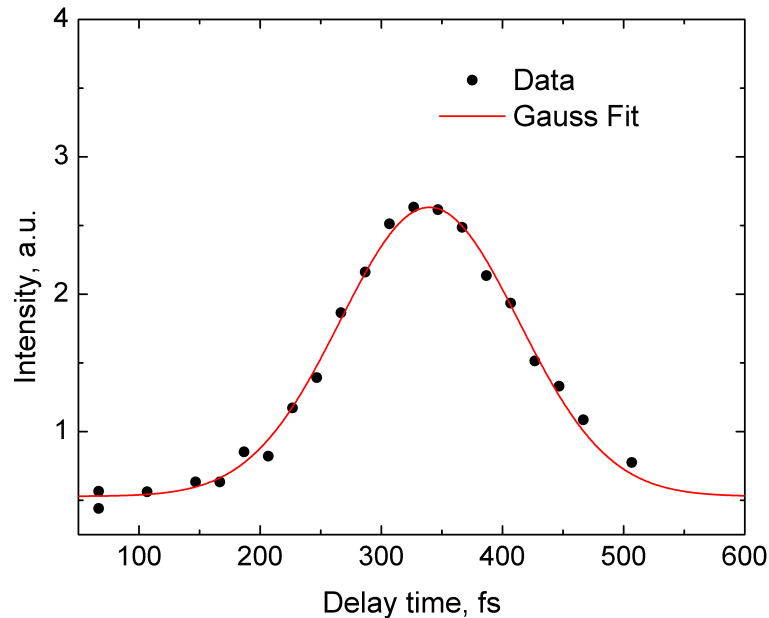


Figure 2.14: Photoelectron signal of $2+1'$ non-resonant multiphoton ionisation of Xe with 2×300 nm and 1×250 nm as a function of the delay time between the two wavelengths. The FWHM of the cross-correlation function is 173 ± 5 fs.

The width of the laser pulse can be obtained from an auto-correlation or a cross-correlation measurement. For a pump-probe experiment, one of the valuable characteristics is the cross-correlation of the pump and probe laser pulses in the interaction region. A cross-correlation in the interaction region of a gas phase TRPEI experiment can be measured with the help of non-resonant multiphoton ionisation. An example of the cross-correlation measurement using $2+1'$ non-resonant ionisation

of Xe is shown in Figure 2.14. The data was fit to a Gaussian function with a FWHM of 173 fs, which corresponds to an average single pulse FWHM of 141 fs.

2.6.4 Mass spectrum and ion imaging

The composition of a molecular sample and formation of molecular clusters in the molecular beam can be verified by performing time of flight (ToF) measurements. A VMI spectrometer can be used for ToF measurements by measuring the ion arrival time at the MCP. Any ion produced in the interaction region will have a kinetic energy proportional to its charge and defined only by the VMI voltages. For non-relativistic ions, the relationship between the arrival time, t , and the mass to charge ratio, m/Z , is:

$$m/Z \propto t^2. \quad (2.12)$$

An example of the ToF spectrum of aniline is shown in Figure 2.15.

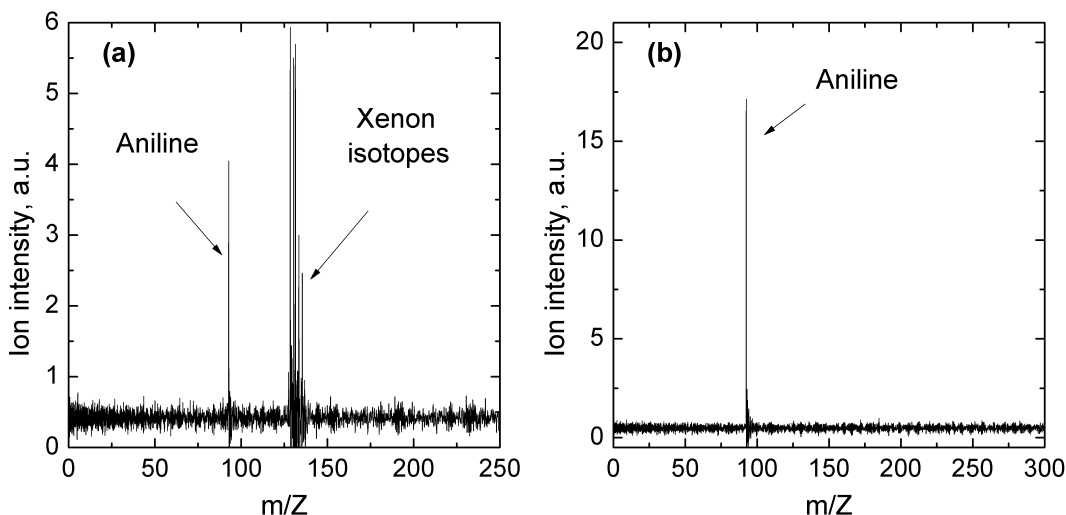


Figure 2.15: Time of flight (ToF) spectrum of (a) aniline seeded in Xe at 1 bar backing pressure and (b) aniline seeded in He at 780 mbar backing pressure. The x axis was calibrated using the ToF of singly ionised Xe isotopes. Only aniline monomers are present in (b) ToF spectrum.

Another way to detect clustering in the molecular beam is to measure a VMI of ions. The molecules in the molecular beam have a reasonably narrow velocity distribution in the direction of propagation. Moreover, the velocity distribution of the clusters will be the same as the monomers, however, the time of flight will be different according to equation (2.12). Assuming that all clusters are singly ionised,

the position on the electron detector, X_i , of a cluster with mass m_i can be calculated as:

$$X_i = v \times t_i \propto v \times \sqrt{m_i}. \quad (2.13)$$

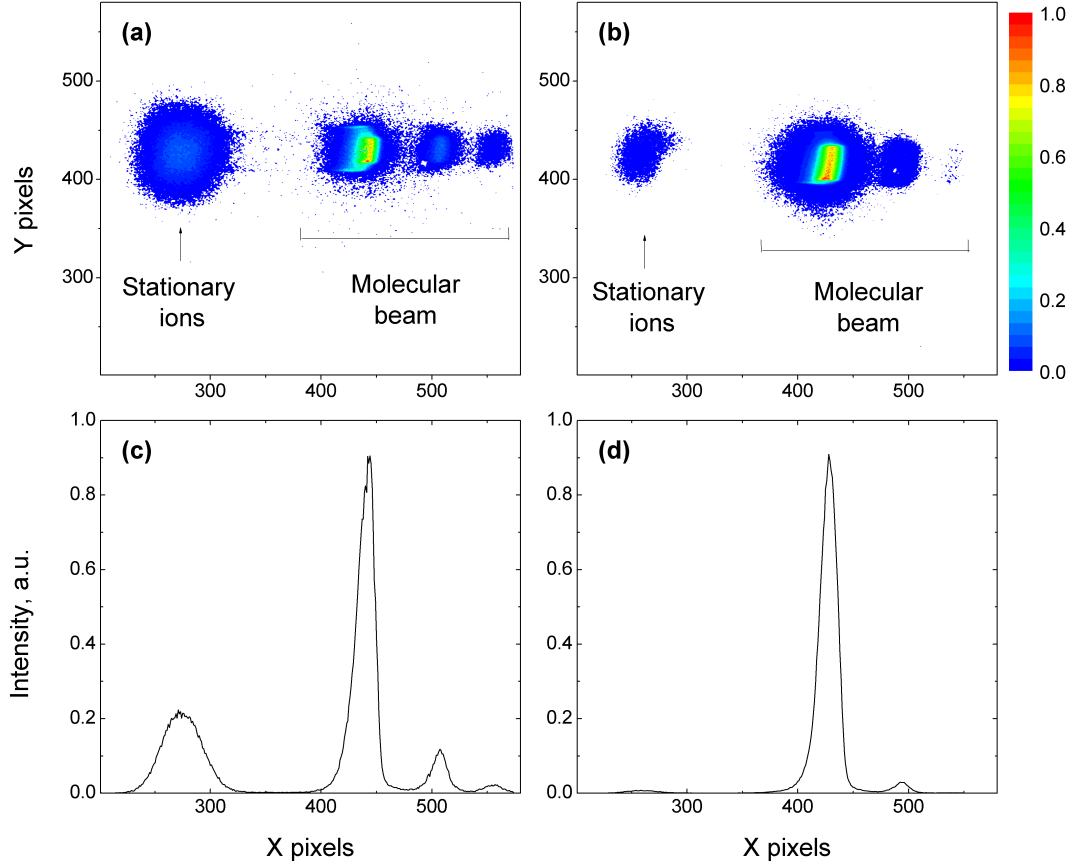


Figure 2.16: A VMI of singly ionised aniline molecules seeded in He gas with backing pressure of (a) 1.5 bar and (b) 780 mbar. (c) and (d) are the projections of the VMI onto the molecular beam propagation direction (x axis) of (a) and (b), respectively. The VMI voltages were slightly defocused in order to spread out the ion signal on the detector. According to equation (2.14), the first peak in the molecular beam corresponds to aniline monomers; the second peak corresponds to dimers; and the third peak, to trimers.

Using equation (2.13), the position ratios between any two cluster types (monomer, dimer, trimer etc.) can be obtained:

$$\begin{aligned} \frac{X_{\text{dimer}}}{X_{\text{monomer}}} &= \sqrt{\frac{m_{\text{dimer}}}{m_{\text{monomer}}}} = \sqrt{2} \\ \frac{X_{\text{trimer}}}{X_{\text{monomer}}} &= \sqrt{\frac{m_{\text{trimer}}}{m_{\text{monomer}}}} = \sqrt{3}. \end{aligned} \quad (2.14)$$

Figure 2.16 shows VMIs of aniline ions at two different backing pressures of He. The higher the backing pressure, the colder is the molecular beam and the more probable is clustering. At 1.5 bar backing pressure of He, the molecular beam cools sufficiently to create dimers and trimers. When the pressure of He is lowered to 780 mbar, the amount of clusters is significantly reduced.

A VMI of a molecular beam also provides an important diagnostic on the nozzle alignment. If the molecular beam passes through the centre of the skimmer, then the VMI image is symmetric with respect to the Y coordinate (perpendicular to the propagation direction). The alignment of the molecular beam through the holes in the μ -metal shielding is also crucial (see Figure 2.4). A badly aligned molecular beam can hit the wall of the μ -metal shielding and scatter around the interaction region, preventing its efficient evacuation and creating a stationary background source.

2.7 Data analysis

2.7.1 Exponential kinetics

The description of the excited state dynamics requires a solution of the time-dependent Schrödinger equation. For polyatomic molecules, this equation can only be solved numerically with some approximations, however, the dynamics of many polyatomic molecules remain a challenge for theoretical chemistry. For the purpose of the experimental data analysis, it is much more convenient to use a simple kinetic model instead of the complicated theoretical calculations.

The kinetic model described in this section does not claim to reproduce an accurate picture of the quantum dynamical processes; however, it provides a simple tool for the semi-quantitative characterisation of the molecular system and allows comparison between different processes and different molecular systems. This model takes into account only the envelope field intensity of the laser pulse and neglects coherence between the two laser pulses.

In the pump-probe experiment, the molecule is electronically excited by a pump laser pulse and ionised after a known time delay by a probe laser pulse. The photoelectron signal is measured as a function of the pump-probe delay time. If no pulse shaping is applied, it is reasonable to assume that the pump, $f_1(t)$, and the probe, $f_2(t)$, laser pulses have a Gaussian temporal profile:

$$f_i(t) = \frac{A_i}{\sqrt{2\pi}\sigma_i} e^{-\frac{1}{2}\left(\frac{t-t_i}{\sigma_i}\right)^2} \quad (i = 1, 2), \quad (2.15)$$

where σ_i is the Gaussian width ($\text{FWHM}_i = 2\sqrt{2\ln 2} \sigma_i$) and A_i is the total laser intensity. In the case of a two-step sequential system (see diagram 2.17) where the excited state S_A is populated from the ground state, S_0 , with a single photon absorption and S_A consequently decays to some intermediate state S_B , the evolution of the populations ρ_A in the excited state S_A , and ρ_B in the excited state S_B , can be described according to the rate equations:

$$\frac{d\rho_A(t)}{dt} = \sigma_{0A}f_1(t) - \lambda_A\rho_A(t), \quad (2.16)$$

$$\frac{d\rho_B(t)}{dt} = \lambda_{AB}\rho_A(t) - \lambda_B\rho_B(t), \quad (2.17)$$

where σ_{0A} is the excitation cross-section from the ground state S_0 to the electronically excited state S_A , λ_A and λ_B are the total decay rates of S_A and S_B , respectively, and λ_{AB} is the partial decay rate of S_A into S_B . In many cases the S_A state has only a single decay pathway, thus, $\lambda_{AB} = \lambda_A$.

In the pump-probe experiments the pump power is kept low such that only a few percent of the ground state population is promoted to the excited state ($\rho_0 \gg \rho_A$), thus ρ_A is not saturated and σ_{0A} can be considered time-independent. The first-order

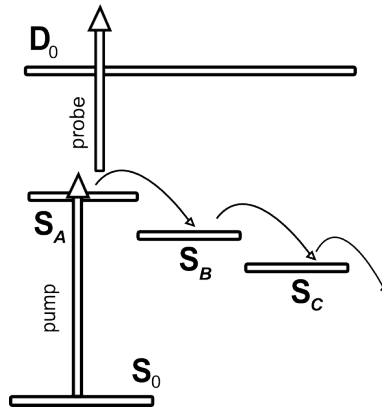


Figure 2.17: Pump-probe experiment diagram with a sequence of three exponential decays $S_A \rightarrow S_B \rightarrow S_C$. A pump photon promotes a molecules from the ground electronic, S_0 state into the excited electronic state, S_A . A probe photon ionises the molecule.

differential equation (2.16) has a known solution:

$$\rho_A(t) = e^{-\lambda_A t} \left(\int_{-\infty}^t e^{\lambda_A x} \sigma_{0A} f_1(x) dx + C_A \right). \quad (2.18)$$

The constant C_A is equal to the S_A population which is unrelated to the excitation process from the ground state. There are no other S_A population pathways considered in this chapter, therefore C_A is always equal to zero. After substituting $f_1(x)$ from equation (2.15) into equation (2.18), the following expression for $\rho_A(t)$ is obtained:

$$\rho_A(t) = e^{-\lambda_A t} \frac{A_1}{\sqrt{2\pi}\sigma_1} \sigma_{0A} \int_{-\infty}^t e^{\lambda_A x} e^{-\frac{1}{2}\left(\frac{x-t_1}{\sigma_1}\right)^2} dx. \quad (2.19)$$

Finally, the $\rho_A(t)$ population has to be convoluted with the probe pulse, $f_2(t)$, in the case of a single photon ionisation process, to obtain the expression for the photoelectron intensity:

$$\begin{aligned} I_A &= \int_{-\infty}^{\infty} \sigma_{\text{ion}A} f_2(t) \rho_A(t) dt \\ &= \sigma_{0A} \sigma_{\text{ion}} \frac{A_1 A_2}{2\pi \sigma_1 \sigma_2} \int_{-\infty}^{\infty} e^{-\frac{1}{2}\left(\frac{t-t_2}{\sigma_2}\right)^2} e^{-\lambda_A t} \int_{-\infty}^t e^{\lambda_A x} e^{-\frac{1}{2}\left(\frac{x-t_1}{\sigma_1}\right)^2} dx dt, \end{aligned} \quad (2.20)$$

where $\sigma_{\text{ion}A}$ is the photoionisation cross-section from the S_A state. The double integral (2.20) can be solved (see Appendix A.1) and the final expression for I_A can be written as:

$$I_A = e^{-\lambda_A(t_2-t_1)} \sigma_{0A} \sigma_{\text{ion}A} \frac{A_1 A_2}{2} e^{\frac{(\sigma \lambda_A)^2}{2}} \left(1 + \text{erf} \left(\frac{t_2 - t_1 - \sigma^2 \lambda_A}{\sqrt{2}\sigma} \right) \right), \quad (2.21)$$

where $\sigma = \sqrt{\sigma_1^2 + \sigma_2^2}$ is the Gaussian cross-correlation of the pump and the probe laser pulses. The photoelectron intensity is a function of the time delay between the pump and the probe laser pulses ($\Delta t = t_2 - t_1$), the pump-probe cross-correlation, σ , and the decay rate, λ_A . It is also proportional to the excitation and ionisation cross-sections and to the total laser intensities A_1 and A_2 . Equation (2.21) consists of two time-dependent parts: the exponential decay and the error function. The error function appears in this equation due to the cross-correlation of the pump and

the probe laser pulses. If the cross-correlation is much shorter than the decay time, the following conditions are fulfilled:

$$\sigma\lambda_A \ll 1 \text{ and } \sigma/\Delta t \ll 1, \quad (2.22)$$

and the convolution part of equation (2.21) disappears:

$$I_A = e^{-\lambda_A(t_2-t_1)}\sigma_{0A}\sigma_{\text{ion}A}A_1A_2, \quad (2.23)$$

and equation (2.21) transforms into a simple exponential decay. However, in many cases the cross-correlation of the laser pulse is comparable to or even larger than, the decay time of the electronic state, thus it is important to take laser temporal width into account.

A similar equation can be obtained for the photoelectron intensity from the S_B state, I_B , by solving the differential equation (2.17):

$$\rho_B(t) = e^{-\lambda_B t} \frac{A_1}{\sqrt{2\pi}\sigma_1} \sigma_{0A} \lambda_{AB} \int_{-\infty}^t e^{\lambda_B x} e^{-\lambda_A x} \int_{-\infty}^x e^{\lambda_A y} e^{-\frac{1}{2}\left(\frac{y-t_1}{\sigma_1}\right)^2} dy dx, \quad (2.24)$$

and then convoluting it with the probe pulse:

$$\begin{aligned} I_B &= \int_{-\infty}^{\infty} \sigma_{\text{ion}B} f_2(t) \rho_B(t) dt \\ &= \sigma_{0A} \sigma_{\text{ion}B} \frac{A_1 A_2}{2\pi\sigma_1\sigma_2} \lambda_{AB} \times \\ &\quad \int_{-\infty}^{\infty} e^{-\frac{1}{2}\left(\frac{t-t_2}{\sigma_2}\right)^2} e^{-\lambda_B t} \int_{-\infty}^t e^{\lambda_B x} e^{-\lambda_A x} \int_{-\infty}^x e^{\lambda_A y} e^{-\frac{1}{2}\left(\frac{y-t_1}{\sigma_1}\right)^2} dy dx dt. \end{aligned} \quad (2.25)$$

The triple integral (2.25) can be solved (see Appendix A.2) and the final expression consists of two additions:

$$\begin{aligned} I_B &= \sigma_{0A} \sigma_{\text{ion}B} \frac{A_1 A_2}{2} \frac{\lambda_{AB}}{\lambda_A - \lambda_B} \times \\ &\quad \left[e^{-\lambda_B(t_2-t_1)} e^{\frac{(\sigma\lambda_B)^2}{2}} \left(1 + \operatorname{erf} \left(\frac{t_2 - t_1 - \sigma^2 \lambda_B}{\sqrt{2}\sigma} \right) \right) - \right. \\ &\quad \left. e^{-\lambda_A(t_2-t_1)} e^{\frac{(\sigma\lambda_A)^2}{2}} \left(1 + \operatorname{erf} \left(\frac{t_2 - t_1 - \sigma^2 \lambda_A}{\sqrt{2}\sigma} \right) \right) \right]. \end{aligned} \quad (2.26)$$

The error functions appear in the solution (2.26) due to the convolution with a Gaussian cross-correlation function as in equation (2.21). The first positive term inside the brackets of equation (2.26) is an exponential decay, while the second negative term is an exponential rise. The important outcome of this solution is that, if the photoelectron signal from the states S_A and S_B can be separately measured, it is possible to compare the decay rate of the S_A state with the rise of the S_B state. Thus, it is possible to follow the population flow from one state to another. This result is especially valuable when more than two states are involved and the dynamics cannot be predicted by any indirect observations. However it is not possible to extract from the measurements, using the analysis of the above solutions, the partial decay rate, λ_{AB} , or the branching ratio, λ_{AB}/λ_A , of the decaying state S_A . This is because the excitation and ionisation cross-sections are usually unknown for the excited states. Once again, for the short laser pulses, when the conditions (2.22) are satisfied, equation (2.26) can be simplified:

$$I_B = \sigma_{0A}\sigma_{\text{ion}B}A_1A_2\frac{\lambda_{AB}}{\lambda_A - \lambda_B} [e^{-\lambda_B(t_2-t_1)} - e^{-\lambda_A(t_2-t_1)}]. \quad (2.27)$$

The previous two solutions (2.21) and (2.26) were obtained for the directly excited state S_A and the indirectly populated state S_B . It is possible to extend the above solutions to more than two states. In a similar manner, the solution for the third state S_C in a three-step model (see Figure 2.17) can be obtained:

$$\begin{aligned} I_C = \sigma_{0A}\sigma_{\text{ion}C} \frac{A_1A_2}{2} \frac{\lambda_{AB}\lambda_{BC}}{\lambda_A - \lambda_B} \times \\ \left[e^{-\lambda_C(t_2-t_1)} e^{\frac{(\sigma\lambda_C)^2}{2}} \frac{\lambda_A - \lambda_B}{(\lambda_A - \lambda_C)(\lambda_B - \lambda_C)} \left(1 + \text{erf} \left(\frac{t_2 - t_1 - \sigma^2\lambda_C}{\sqrt{2}\sigma} \right) \right) - \right. \\ e^{-\lambda_B(t_2-t_1)} \frac{e^{\frac{(\sigma\lambda_B)^2}{2}}}{\lambda_B - \lambda_C} \left(1 + \text{erf} \left(\frac{t_2 - t_1 - \sigma^2\lambda_B}{\sqrt{2}\sigma} \right) \right) + \\ \left. e^{-\lambda_A(t_2-t_1)} \frac{e^{\frac{(\sigma\lambda_A)^2}{2}}}{\lambda_A - \lambda_C} \left(1 + \text{erf} \left(\frac{t_2 - t_1 - \sigma^2\lambda_A}{\sqrt{2}\sigma} \right) \right) \right]. \quad (2.28) \end{aligned}$$

The evolution of the photoelectron signal consists of a sum of exponential functions convoluted with a Gaussian cross-correlation function. A general solution of the evolution of the photoelectron signal in time for any excited state, X , can be written as:

$$I_X = \sum_{i=1}^M C_i e^{-\lambda_i(t_2-t_1)} e^{\frac{(\sigma\lambda_i)^2}{2}} \left(1 + \operatorname{erf} \left(\frac{t_2 - t_1 - \sigma^2\lambda_i}{\sqrt{2}\sigma} \right) \right), \quad (2.29)$$

where M is the total number of steps required to reach the excited state X . For the directly excited state, $M = 1$. Positive C_i coefficients correspond to the exponential decay, while negative C_i coefficients correspond to the exponential rise. When fitting experimental data to equation (2.29), a number of decays are usually unknown and the number M has to be chosen to be as low as possible yet sufficiently large to describe the experimental data.

2.7.2 Fitting of the experimental data

There are two types of data sets obtained from the TRPES experiments. The first type is a one-dimensional dependence of the count rate on the pump-probe delay, $g(\Delta t)$. The second type is a two-dimensional dependence of the photoelectron spectrum on the pump-probe delay, $g(\Delta t, \text{eKE})$, where eKE is the electron kinetic energy. The one dimensional dependence is used for the analysis of the total count rate or when a contribution from a single excited state can be separated in the photoelectron spectra (PES).

As a result of the data processing, the count rate, y , versus the time delay, $\Delta t = t_{\text{probe}} - t_{\text{pump}}$, can be obtained $\{\Delta t_j, y_j, \Delta y_j\}_{j=1\dots N}$, where N is the number of experimental points.

There are two possible ways to estimate the statistical error, Δy , for the count rate. The first method is to make a set of n independent measurements, $\{y_i\}$, for each time delay Δt . Then the mean value of the count rate and its statistical error can be evaluated as following:

$$y_{\text{mean}} = \frac{1}{n} \sum_{i=1}^n y_i, \quad \Delta y = \sqrt{\sum_{i=1}^n \frac{(y_i - y_{\text{mean}})^2}{n(n-1)}}. \quad (2.30)$$

The second option is to assume that the photoelectron counts have a Poisson distribution. In this case, it is sufficient to use only a single measurement of the photoelectron counts, y_{tot} , at a particular time delay to estimate the statistical error:

$$\Delta y = \sqrt{y_{\text{tot}}}. \quad (2.31)$$

The advantage of equation (2.30) is that it takes into account all the statistical changes in the system (laser power, laser divergence, laser position, etc.). However, to make a good estimation using equation (2.30), a sufficient number, n , of independent measurements must be taken, which is often not possible. The data presented in the experimental section has only a single measurement for each time delay, therefore, equation (2.31) was used in all cases.

In order to extract desirable parameters like decay rates, λ_k , from the experimental data, a χ^2 function can be constructed [100] and minimised:

$$\chi^2 = \sum_{j=1}^N \frac{(y_j - g(\Delta t_j; \sigma, \lambda_k, \dots))^2}{\Delta y_j^2}, \quad (2.32)$$

where $g(\Delta t_j; \sigma, \lambda_k, \dots)$ is the function of pump-probe delay time, Δt , which describes the evolution of the photoelectron count rate and N is the number of experimental points. A general expression for this function is given by equation (2.29). For the data presented in the experimental chapter, the minimisation of the χ^2 expression (2.32) was performed using MINUIT minimisation libraries as part of ROOT scientific software [101]. The MIGRAD fitting strategy (Davidon-Fletcher-Powell variable-metric algorithm) was employed from within the MINUIT package. The errors were derived from the error matrix estimated by the MIGRAD procedure and they were always checked by the MINOS procedure which is based on the method described in [102] and designed to calculate the correct errors in all cases. The goodness of the fit was estimated using χ^2 normalised by the number of degrees of freedom (DoF):

$$\frac{\chi^2}{\text{DoF}} = \frac{\chi^2}{N - \nu - 1}, \quad (2.33)$$

where N is the number of experimental points and ν is the number of parameters. For an ideal fit, $\chi^2/\text{DoF} = 1$. If $\chi^2/\text{DoF} \ll 1$, then either the errors are over-estimated or the fitting function is over-parametrised. If $\chi^2/\text{DoF} \gg 1$ then either the errors are under-estimated or the fitting function does not describe the experimental data correctly.

If the contributions from different electronic states are overlapped in the PES then a two-dimensional dependence has to be used for revealing the desired parameters such as decay rates and photoelectron intensity contributions at a particular photoelectron kinetic energy, eKE. In this case, equation (2.29) is slightly modified as the C_i coefficients are now dependent on eKE:

$$y(\Delta t, \text{eKE}) = \sum_{i=1}^M C_i(\text{eKE}) e^{-\lambda_i \Delta t} e^{\frac{(\sigma \lambda_i)^2}{2}} \left(1 + \text{erf} \left(\frac{\Delta t - \sigma^2 \lambda_i}{\sqrt{2} \sigma} \right) \right), \quad (2.34)$$

The experimental data now contains a two-dimensional set of photoelectron intensities, $\{\Delta t_j, \text{eKE}_k, y_{jk}\}_{j=1\dots N, k=1\dots K}$, as a function of the pump-probe delay time, Δt , and photoelectron kinetic energy, eKE. The value K represents the number of energy bins. The χ^2 function (2.32) can be modified for this case:

$$\chi^2 = \sum_{k=1}^K \sum_{j=1}^N \frac{(y_{j,k} - g(\Delta t_j, \text{eKE}_k; \sigma, \lambda_i, \dots))^2}{\Delta y_{j,k}^2}. \quad (2.35)$$

It is clear that equation (2.34) contains many more parameters than equation (2.29). Minimisation with a large number of parameters takes a lot of computing power and its convergence is heavily dependent on the guess of the initial parameters. Therefore, it is often more practical to use integrated photoelectron intensity minimisation (2.32) for determining decay rates and two-dimensional minimisation (2.35) to obtain spectral coefficients, $C_i(\text{eKE})$.

Chapter 3

Ultrafast non-adiabatic dynamics in aniline

Femtosecond time-resolved photoelectron imaging is employed to investigate ultrafast electronic relaxation in aniline and fully deuterated aniline (aniline-D₇). Aniline is excited at wavelengths between 269 and 236 nm while aniline-D₇ is excited at 260 nm. Our observations show the direct population of the S₂($\pi 3s/\pi\sigma^*$) state in both molecules and at all wavelengths studied, and that the population bifurcates to two decay pathways. The first pathway involves the decay of the Rydberg $\pi 3s$ component to the S₁($\pi\pi^*$) state and the other pathway appears to involve motion along the $\pi\sigma^*$ dissociative potential energy surface. Comparison of the relaxation times between aniline and aniline-D₇ suggests that no significant tunneling occurs from the S₂($\pi 3s/\pi\sigma^*$) state. In aniline, at higher excitation energies, the dominant excitation is to the S₃($\pi\pi^*$) state, which undergoes extremely efficient electronic relaxation back to the ground state.

This chapter begins with a detailed discussion of the $\pi\sigma^*$ states and the electronic structure, spectroscopy and dynamics of aniline, to set our work in context. It is followed by a brief description of the experimental details relevant to our work, presentation of the first TRPES of aniline and deuterated aniline, and a detailed discussion of the interpretation of the data.

3.1 Introduction

Aniline is the simplest aromatic amine (see Figure 3.1) and has been used as a benchmark molecule to understand the photochemistry and electronic structure of other aromatic amines [103, 104, 105, 106]. Aromatic amines are a common structural motif in biological molecules. Many biological chromophores are substituted aromatics whose UV absorption spectra are dominated by strong transitions to $^1\pi\pi^*$ states. These molecules also tend to have low-lying dissociative states with $^1\pi\sigma^*$ or $^1n\sigma^*$ character [107], which can be populated directly, albeit weakly, or indirectly by internal conversion from optically bright $^1\pi\pi^*$ states. Since Sobolewski *et al.* [108] suggested that these dissociative states play an important role in the non-radiative decay of various biological chromophores, there has been a surge of interest in studying the photochemistry of substituted aromatics [109].

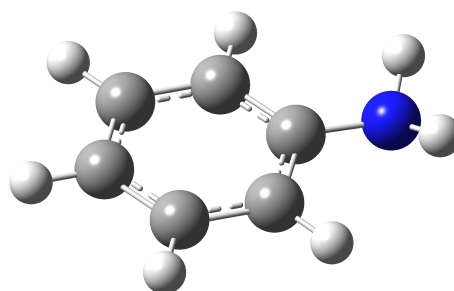


Figure 3.1: Aniline molecule in the ground electronic state. Benzene ring with NH_2 group replacing one of the hydrogen atoms.

3.2 $\pi\sigma^*$ and $n\sigma^*$ states

The $\pi\sigma^*$ and $n\sigma^*$ states are formed from the electronic excitation of π and n electronic molecular orbitals to the σ^* molecular orbital, where π are bonding and n are non-bonding occupied orbitals. These states generally exhibit weak single photon absorption compared to the $\pi^* \leftarrow \pi$ transitions. However, they may be populated either directly or indirectly through an IC from the optically “bright” $\pi\pi^*$ states. Sobolewski *et al.* [108] provided a detailed theoretical characterisation of the $\pi\sigma^*$ states in aromatic biomolecules. The $\pi\sigma^*$ state is totally repulsive with respect to the X–H bond stretch (X=N,O), the energetic location of the $\pi\sigma^*$ state with respect

to the $\pi\pi^*$ states very much depends on the environment due to its polar configuration, and the $\pi\sigma^*$ potential energy surface generally has a CI with the ground potential energy surface. The latter provides a route for ultrafast internal conversion from the dissociative $\pi\sigma^*$ state back to the ground electronic state.

The shape of the $\pi 3s/\pi\sigma^*$ potential energy surface is highly dependent on the relative stability of the Rydberg and valence configurations. If the $\pi 3s$ and $\pi\sigma^*$ components are nearly degenerate in the vertical Franck-Condon region, as they are in phenol [42], the entire potential energy surface is almost totally dissociative (see Figure 3.2 (a)). If, however, the Rydberg state is lower in energy than the dissociative valence state, as it is in aniline [103, 104, 106], the $\pi 3s/\pi\sigma^*$ potential energy surface will have a pronounced potential well in the vertical Franck-Condon region and only becomes dissociative at longer N–H bond distances, as shown in Figure 3.2 (b).

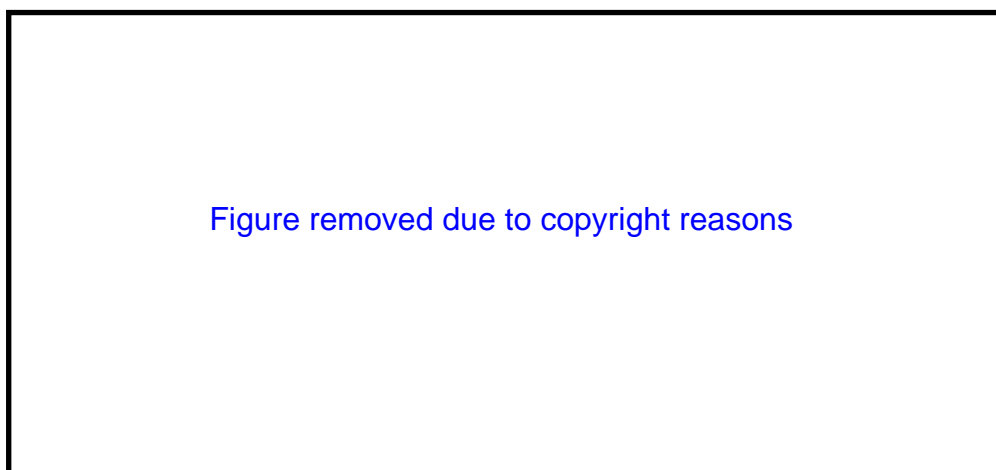


Figure 3.2: A schematic diagram of the adiabatic potential energy surfaces produced from the interaction between the $\pi\sigma^*$ dissociative valence state and the $\pi 3s/$ Rydberg state reproduced from reference [103]. The potential energy surfaces are shown as a function of the X–H bond stretch (X=N,O). (a) The $\pi 3s$ and $\pi\sigma^*$ states are nearly degenerate in the vertical Franck-Condon region forming an entirely dissociative potential energy surface. (b) The $\pi 3s$ state is lower in energy than the $\pi\sigma^*$ state and the resulting potential energy surface has a pronounced potential well in the vertical Franck-Condon region.

In aniline, the N-centered $^1\pi 3s$ and $^1\pi\sigma^*$ configurations form an avoided crossing at relatively modest N–H internuclear separations (Figure 3.2 (b)) and the lower adiabatic potential energy surface is best described as a singlet $\pi 3s/\pi\sigma^*$ state [107].

Along the N–H stretch coordinate in aniline, the $\pi 3s/\pi\sigma^*$ state intersects the lower-lying ${}^1\pi\pi^*$ state and the electronic ground state. These crossings develop into conical intersections when out of plane vibrations are introduced [42, 109, 110, 111].

3.3 Spectroscopy, structure and dynamics

3.3.1 Spectroscopy and structure of aniline

The equilibrium electronic ground state geometry of aniline is shown in Figure 3.1. The geometry was determined to be non-planar from electron diffraction and microwave spectroscopy experiments [112, 113] and DFT theoretical studies [114, 115]. The NH_2 plane in the ground state was found to be around 40° with respect to the ring plane by both experimental and theoretical studies [112, 113, 114, 115]. Thus, the ground state of the aniline molecule has a C_S point group.

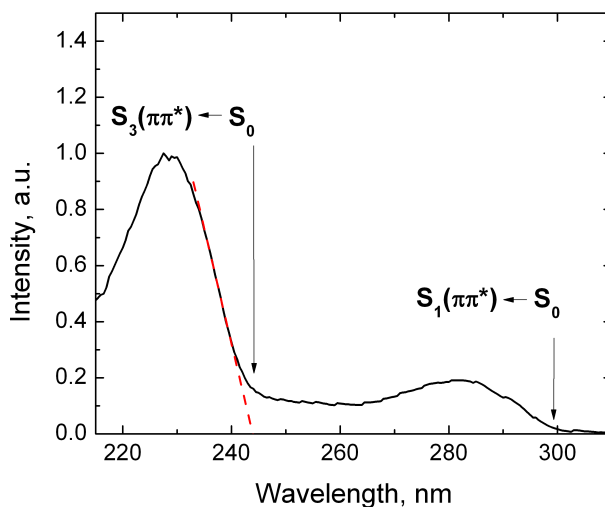


Figure 3.3: A gas-phase UV absorption spectrum of aniline. The low intensity band centred at 280 nm corresponds to absorption to the $S_1(\pi\pi^*)$ state while the high intensity band centred at 230 nm corresponds to absorption to the $S_3(\pi\pi^*)$ state. The black arrows indicate the onset of the corresponding absorption band. The origin of the $S_3(\pi\pi^*)$ state has been estimated to be 243 nm (5.1 eV) from the intersection between the linear fit to the slope of the second absorption band (dashed red line) and the x axis.

The absorption spectrum of gas-phase aniline (see Figure 3.3) has two strong

bands centred at 280 nm and 230 nm. The third band rises below 210 nm [116] which is outside the wavelength measurement range of our equipment. The first two bands correspond to absorption to the first and second valence singlet $\pi\pi^*$ states: $S_1(\pi\pi^*)$ and $S_3(\pi\pi^*)$ [106]. The origin of the first singlet $S_1(\pi\pi^*)$ state was measured to be $34\,029\text{ cm}^{-1}$ (4.22 eV) above the ground state [117] in a zero kinetic energy (ZEKE) photoelectron spectroscopy study. The vertical excitation energy of the second valence $S_3(\pi\pi^*)$ state has been calculated to be 5.34 eV [106] which is close to the absorption maximum at 5.4 eV (230 nm), shown in Figure 3.3. The origin of the $S_3(\pi\pi^*)$ state has not been determined experimentally at present, however, our estimate of its origin is 5.1 eV, obtained from the intersection of the linear fit to the slope of the second absorption band with the x axis as shown by a red dashed line in Figure 3.3.

The equilibrium geometries of the first and second excited states of aniline have been determined at the CASPT2 level of theory in our group [118]. The first excited state, $S_1(\pi\pi^*)$, has similar structure to the ground state with a slightly expanded ring and around 20° pyramidal angle between the NH_2 plane and the ring plane which is in a good agreement with previous CASSCF calculations [119, 120]. According to the CASSCF calculations by Stavros *et al.*, the equilibrium structure of the $S_3(\pi\pi^*)$ state undergoes a significant change compared to the ground electronic state: the angle between the NH_2 plane and the ring plane decreases to 16° and the C-N bond becomes shorter (from 1.4 Å in S_0 to 1.34 Å in S_3).

In addition to the $\pi\pi^*$ states, which are pronounced in the absorption spectrum of aniline, Ebata *et al.* were the first to observe experimentally the $S_2(\pi 3s/\pi\sigma^*)$ state [105]. They employed UV-IR double-resonance spectroscopy to study the vibrational levels of $S_1(\pi\pi^*)$; however, they observed a number of broad transitions lying at wavenumbers greater than 3500 cm^{-1} above the $S_1(\pi\pi^*)$ origin that could not be assigned to fundamental vibrations of the $S_1(\pi\pi^*)$ state. Subsequent 2+2 resonance-enhanced multiphoton ionisation spectroscopy found a sharp peak at $37\,104\text{ cm}^{-1}$ (4.6 eV) above the ground state, which was assigned as the $S_2(\pi 3s/\pi\sigma^*)$ origin. The observation of a short vibronic progression then led to the conclusion that the potential energy surface is not purely repulsive but has a potential minimum close to the Franck-Condon region. The structure of the second excited state, $S_2(\pi 3s/\pi\sigma^*)$, was found to be planar with a slightly expanded ring compared to the ground state [118].

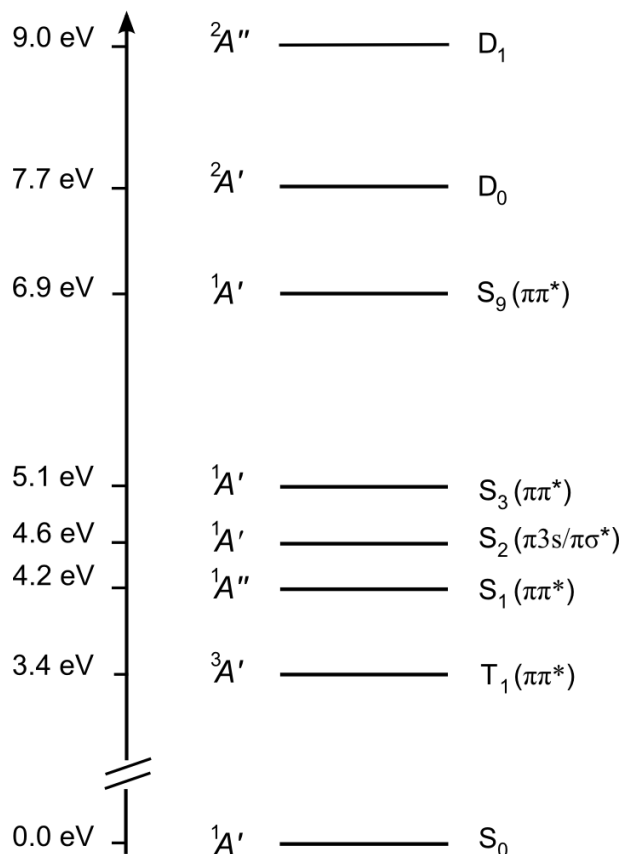


Figure 3.4: An energy level diagram of the low lying electronic states of aniline and its cation. The symmetries of the electronic states in the C_s point group are shown on the left side. The $\pi\pi^*$ states have high oscillator strengths and therefore strongly contribute to the absorption spectrum shown in Figure 3.3. The $S_9(\pi\pi^*)$ state has the highest oscillator strength according to the SAC-CI calculations by Honda *et al.* [106], however, it lies energetically beyond the single photon excitation energies studied in this work.

Honda *et al.* have reported the most detailed theoretical study of the electronic structure of aniline using symmetry adapted cluster/configuration interaction [106]. They determined that the lowest singlet excited state was a $1\pi\pi^*$ state with mainly charge-resonance character and some charge-transfer character (hereafter referred to as $S_1(\pi\pi^*)$). The vertical excitation energy of this state was calculated to be 4.20 eV. The second singlet excited state was determined as having mixed Rydberg-valence character and a calculated vertical excitation energy of around 4.53 eV (hereafter referred to as $S_2(\pi 3s/\pi\sigma^*)$). However, the oscillator strength of this state was calculated to be four times weaker than the one for the $S_1(\pi\pi^*)$ state. The third singlet excited state was identified as another $1\pi\pi^*$ state, resulting from local excitation on the benzene ring (hereafter referred to as $S_3(\pi\pi^*)$). The vertical

excitation energy of this state was determined to be 5.34 eV. These calculations are consistent with the gas-phase absorption spectrum of aniline (Figure 3.3) which displays absorption maxima around 4.4 eV and 5.4 eV and a fairly significant, but structureless, background between them.

A summary of the electronic structure of aniline and symmetries in the C_S point group is shown in Figure 3.4. The adiabatic ionisation energies of aniline to the ground, D_0 , and first excited, D_1 , electronic states of the aniline cation have been determined to be 7.72 eV from the study of a ZEKE aniline spectrum [117] and 9.03 eV from the two-colour photoelectron spectrum obtained *via* the excitation of the $S_1(\pi\pi^*)$ origin [60], respectively.

The aniline molecule has 36 vibrational degrees of freedom. A number of experimental measurements have been performed on the vibrational structure of aniline in the ground electronic state using infrared spectroscopy [121, 122, 123, 124] providing detailed information about all 36 vibrational modes. A comprehensive theoretical study of the vibrational modes in the ground electronic state of the neutral molecule and cation have been reported in several papers [114, 115] showing a good agreement with the experimental data. The wave numbers of the vibrational modes in the ground electronic state of aniline range from 200 cm^{-1} for the benzene ring deformation to 3500 cm^{-1} for the modes containing C-H and N-H stretch motions. The high resolution spectra of aniline $S_1(\pi\pi^*)$ vibronic states have very sharp features at low excess energies and are vibrationally unresolved above 3000 cm^{-1} [105, 117, 120, 125, 126]. A high resolution LIF spectrum measured by N. Mikami *et al.* in jet-cooled aniline [126] shows that the most intense vibronic transitions with a single photon absorption involve totally symmetric vibrations: ν_{6a} (492 cm^{-1}), ν_1 (798 cm^{-1}), ν_{12} (955 cm^{-1}), ν_{13} (1311 cm^{-1}) and ν_8 (1434 cm^{-1}). All of these modes involve benzene ring deformation motions except mode ν_{13} which involves CN stretch, ring stretch and a small amount of NH_2 scissor motion [117]. In addition, their assignment includes a reasonably intense out of plane NH_2 inversion mode ν_1 (352 cm^{-1}).

A comprehensive theoretical study of the triplet states in aniline is presented in [59] where the vertical excitation energies and electronic character of seven triplet states have been studied. The lowest three triplet states correspond to $\pi\pi^*$ excitation character. The first two triplet states have 3.74 eV and 3.82 eV vertical excitation energy which is below the first singlet excited state. The lowest triplet state adiabatic

energy has been calculated as 3.45 eV which is in good agreement with experimental values of 3.41 eV – 3.45 eV above the ground state, determined in phosphorescence studies [127, 128].

3.3.2 Intersystem crossing

After photo-excitation to the $S_1(\pi\pi^*)$ state with low excess energy (below 3000 cm^{-1}) the molecule fluoresces with a quantum yield of about 0.2 [129] and non-adiabatic intersystem crossing (ISC) brings the rest of the population directly to the lowest triplet state [60] (see section 1.5.3). The time-scale of the ISC depends on the vibrational state and varies between 7 ns and 12 ns when the excess energy in the $S_1(\pi\pi^*)$ state is below 3000 cm^{-1} [129]. However, at higher excitation energies above the origin of $S_2(\pi 3s/\pi\sigma^*)$, the lifetime of the $S_1(\pi\pi^*)$ state decreases with the excitation wavelengths as shown in Table 3.1 (section 3.4.4). These observations are similar to the observations around the “channel 3” region in the photodynamics of benzene [130, 131, 132], indicating that at high excess energies internal conversion between the S_1 state and the ground state becomes dominant.

3.3.3 Internal conversion

After photoexcitation of aniline above the origin of the S_2 state, internal conversion between the singlet states becomes a dominant relaxation process. Castaño *et al.* carried out the first femtosecond time-resolved study of electronic relaxation in aniline using pump-probe photoionisation spectroscopy [104]. They observed a 165 fs timescale for all excitation wavelengths in the range 269–240 nm (see Figure 3.5), which they attributed to dynamics on the $S_2(\pi 3s/\pi\sigma^*)$ surface through the S_2/S_1 conical intersection. They argued that population was transferred both to the dissociative $\pi\sigma^*$ potential energy surface and to the $S_1(\pi\pi^*)$ state. They also observed a long timescale (tens of picoseconds to nanoseconds) which they attributed to subsequent electronic relaxation of $S_1(\pi\pi^*)$ back to the electronic ground state. Due to the relatively minor contribution of the 165 fs component, they concluded that the dissociative $\pi\sigma^*$ potential energy surface plays a minor role in the photochemistry of aniline. Decreasing the excitation wavelength to 234 nm resulted in a very fast 21 fs timescale, which was attributed to population on $S_3(\pi\pi^*)$ undergoing extremely rapid internal conversion to $S_1(\pi\pi^*)$ which relaxes back to the ground state

on a timescale of tens of picoseconds. By using only the total ion detection, however, they were unable to observe electronic states separately and thus the population flow between the electronic states was not detected. The two photon ionisation scheme is also disadvantaged by a high contribution of the multiphoton ionisation signal to the measurements, which can add some complications to the interpretation of the data.

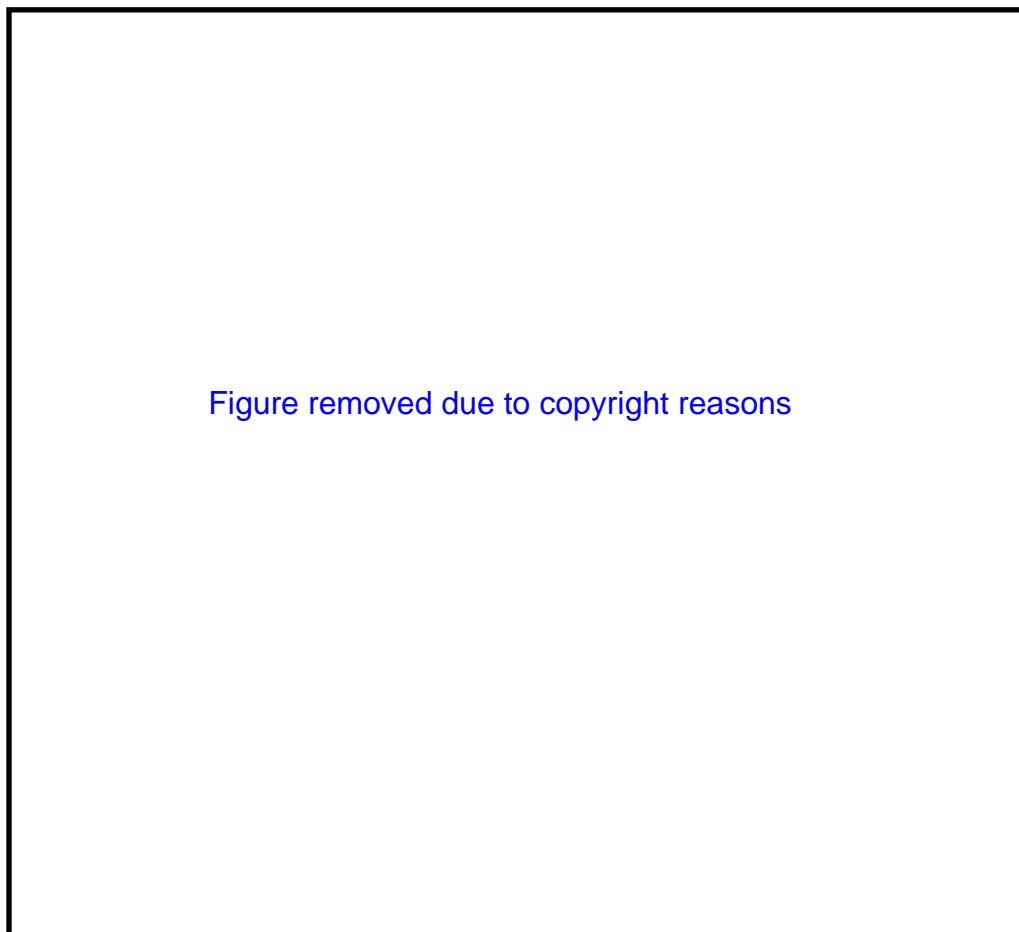


Figure 3.5: Femtosecond pump-probe photoionisation study of aniline reproduced from reference [104]. Aniline ion signal as a function of pump-probe delay time, recorded for different excitation wavelength. The pump wavelength was varied in the range 274–240 nm and the probe wavelength was 400 nm. The circles and red line correspond to the experimental data and multi-exponential fit, respectively. The black, blue, and green lines are the individual exponential components with the values indicated in (f).

3.3.4 H atom loss

The N-H bond is the weakest bond in aniline. When the bond is broken, the anilino radical (C_6H_5NH) and H atom fragments are formed. The bond dissociation energy (BDE) of C_6H_5NH in the gas phase has been measured as 89.7 kcal/mol (3.89 eV or $31\,373\text{ cm}^{-1}$) using photoacoustic calorimetry [133] and $31\,630\text{ cm}^{-1}$ (3.92 eV or 90.4 kcal/mol) from H atom photofragment translational spectroscopy [103]. The value of BDE is below the first excited state (4.22 eV), however, the potential energy curve has a barrier with respect to the N-H stretch coordinate before it becomes dissociative (see Figure 3.6).

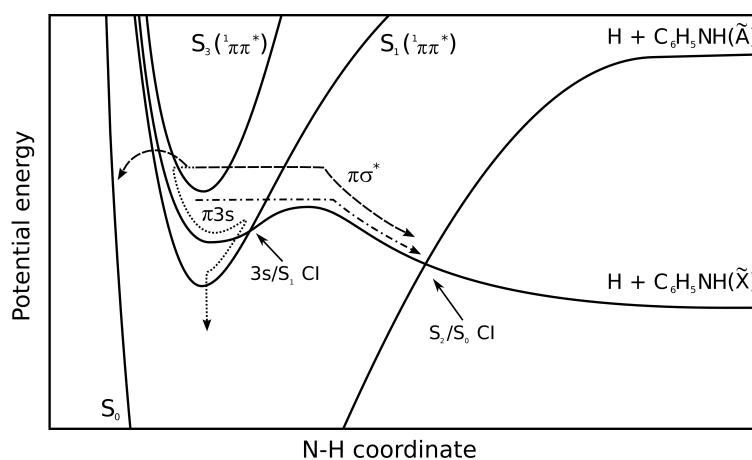


Figure 3.6: Schematic potential energy curves for the four lowest singlet states of aniline along the N-H stretch coordinate. The S_0 , $S_1(\pi\pi^*)$ and $S_3(\pi\pi^*)$ states are bound whereas the $S_2(\pi 3s/\pi\sigma^*)$ state has mixed Rydberg and valence character and is dissociative along the N-H stretch coordinate. Various non-radiative decay mechanisms, deduced from our analysis of the time-resolved photoelectron spectra, are also illustrated.

Ashfold *et al.* have undertaken a comprehensive study of the photodissociation of aniline using H (Rydberg) atom photofragment translational spectroscopy [103]. Below the $S_2(\pi 3s/\pi\sigma^*)$ origin, they found that H atom loss occurred mainly by multiphoton processes, resonantly enhanced at the one-photon level. Decreasing the excitation wavelength in order to excite the first few vibrational levels of $S_2(\pi 3s/\pi\sigma^*)$ (269–260 nm) was found to induce N–H bond fission, creating H atoms with anisotropic velocity distributions and anilino radicals in a few low vibrational states of the ground electronic state (see Figure 3.7). These observations were explained in terms of H atom tunnelling through the barrier along the N–H bond stretch, on a



Figure 3.7: Experimental results of H atom photofragment translational spectroscopy reproduced from reference [103]. The graphs show the dissociation signal as a function of the internal energy of the anilino radical formed following a single photon excitation of aniline with a different excitation wavelengths. The graphs are derived from TKER spectra. The peaks in the spectra labeled as $v=0$ correspond to the anilino radical in its ground vibrational state. The excitation wavelength is indicated in each graph.

timescale faster than molecular rotation, and adiabatic evolution of the vibrational mode of aniline into the corresponding vibrational mode in the anilino fragment. The rotation period of a molecule depends on the rotational quantum number, J , and can be estimated from the rotational constant according to the following formula [134]:

$$T(J) = \frac{1}{2c\sqrt{BE_J}}, \quad (3.1)$$

where B is the rotational constant in cm^{-1} , c is the speed of light and E_J is the rotational energy in cm^{-1} . The most probable E_J can be estimated from the rotational temperature, T_R , of the molecular sample: $E_J = k_B T_R$. A typical rotational temper-

ature in a molecular jet under the experimental conditions described in [103] (aniline is seeded in Ar at 700 mbar) is about 5 K [80] which corresponds to $E_J = 7 \text{ cm}^{-1}$. Rotation constants for aniline are $0.03\text{--}0.2 \text{ cm}^{-1}$ in the ground and first excited singlet states [120, 135], corresponding to rotational periods of 20 to 50 ps.

Decreasing the excitation wavelength further, led to the observation of anilino radicals with greater vibrational excitation, explained as direct excitation to $S_1(\pi\pi^*)$ followed by internal conversion through an S_1/S_2 conical intersection to the dissociative $\pi\sigma^*$ potential energy surface. At around 230 nm excitation wavelength, changes in the profile of the H atom kinetic energy distribution were interpreted in terms of direct excitation to $S_3(\pi\pi^*)$ followed by internal conversion through an S_3/S_2 conical intersection or through successive S_3/S_1 and S_1/S_2 conical intersections to the dissociative $\pi\sigma^*$ potential energy surface.

Figure removed due to copyright reasons

Figure 3.8: H atom total kinetic energy release spectrum following (a) 240 nm and (c) 200 nm excitation wavelengths. H^+ signal integrated over the Gaussian fit components (blue area) as a function of pump-probe delay for (b) 240 nm and (d) 200 nm excitation wavelengths. All graphs in this figure are reproduced from reference [119].

Stavros *et al.* have employed femtosecond pump-probe velocity map imaging to monitor the formation of H atoms following excitation of aniline around 240 nm and 200 nm (see Figure 3.8) and observed a timescale of around 155 fs for the formation of low and high kinetic energy H atoms [119] which they attributed to the dissociation on the $\pi\sigma^*$ potential energy surface following the population flow

through $S_1(\pi\pi^*)/S_2(\pi3s/\pi\sigma^*)$ CI. Their experiments were complemented by theory at the CASSCF level and identified a number of CIs between the first three excited singlet states.

3.4 TRPEI investigation of aniline following 269 – 236 nm excitation

3.4.1 Experimental method

In our investigation of the femtosecond excited state dynamics of aniline we employed the TRPEI technique. These experiments complement the previous time-resolved total ion signal measurements carried out by Castaño *et al.* [104]. The advantage of PES detection scheme over the energy integrated scheme employed by Castaño *et al.* is that in the photoelectron spectrum it is possible to differentiate between the excited states, populated upon photoionisation, thus, gaining a better detection sensitivity and ability to follow the population flow between the excited states. The excitation scheme is shown in Figure 3.9. Aniline is excited above the origin of the second singlet excited state, $S_2(\pi3s/\pi\sigma^*)$, using 269–236 nm (4.61–5.25 eV) femtosecond laser pulses. The excited state population was projected onto the photoionisation continuum using a delayed 300 nm (4.13 eV) femtosecond laser pulse, selected to access as much of the ionisation continuum as possible whilst being below the onset of significant S_1-S_0 absorption. Photoelectron images are then recorded for a series of pump-probe delays.

A detailed description of the experimental apparatus is presented in chapter 2. Briefly, it consists of a continuous molecular beam, a 1 kHz femtosecond laser system and a velocity map imaging apparatus based on the Eppink and Parker design [89]. The molecular beam of aniline is created by passing He carrier gas through liquid aniline (Sigma-Aldrich, > 99%) at 750 mbar and expanding it through a 50 μm nozzle. The beam is collimated by a 1 mm skimmer before passing into the interaction region of the velocity map imaging spectrometer. The time-of-flight mass spectrum of aniline is shown in Figure 3.9 (a). The spectrum contains only the ion signal from a singly ionised aniline molecule and shows that there are no clusters formed.

The cross-correlation of the pump and the probe laser pulses ranges from 150 fs to 210 fs. The pulse energies are attenuated to less than 1 μJ to minimise multiphoton

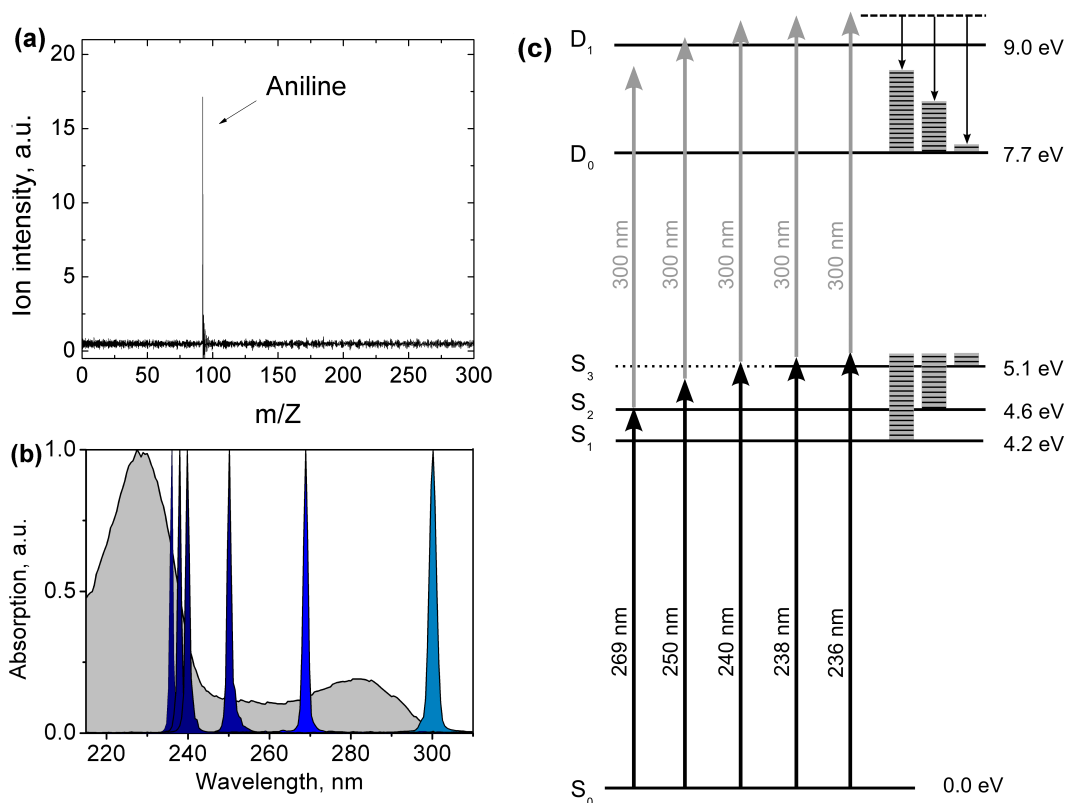


Figure 3.9: (a) TOF mass spectrum of aniline seeded with He gas under 750 mbar backing pressure, excited with 236 nm and ionised with 300 nm femtosecond laser pulses. (b) Gas-phase UV absorption spectrum of aniline, with pump and probe pulse profiles superimposed. (c) Excitation scheme: aniline is excited using 269 nm (4.61 eV), 250 nm (4.96 eV), 240 nm (5.17 eV), 238 nm (5.21 eV) and 236 nm (5.25 eV) pump pulses. The excited state population is projected onto the photoionisation continuum using a delayed 300 nm (4.13 eV) probe pulse. Assuming a $\Delta v = 0$ propensity rule for photoionisation, the electron kinetic energy following ionisation out of the Franck-Condon region is expected to increase in the order $S_1 < S_2 < S_3$. The vibrational energies (blocks of horizontal lines) and corresponding eKEs (downward vertical arrows) are illustrated for 236 nm excitation.

processes and to keep photoelectron count-rates below 20 photoelectrons per laser pulse. For each pump-probe delay, we collect pump-only, probe-only and pump + probe images, in sequence, for 20 seconds each. This is repeated around 30 times for approximately 30 minutes for each pump-probe delay. The pump-only and probe-only signals are subtracted from the pump + probe signal to eliminate one-colour contributions from the images. Photoelectron spectra are recovered from the raw images using the pBasex image inversion algorithm [96]. Photoelectron angular distributions are obtained as a result of the pBasex inversion, which has the following expression for the angular basis set:

$$I(\theta) = a[1 + \beta_2 P_2(\cos \theta) + \beta_4 P_4(\cos \theta)], \quad (3.2)$$

where $I(\theta)$ is the probability of photoelectron emission at a particular angle θ , defined as the angle between the laser polarization and the velocity vector of the photoelectron, $P_n(\cos \theta)$ are the n^{th} order Legendre Polynomials, β_n are the anisotropy parameters and a is a normalisation constant. A raw photoelectron image recorded with a 240 nm pump pulse and a 5 fs pump-probe delay is presented in Figure 3.10(a) together with the corresponding photoelectron spectrum and anisotropy parameter, β_2 , in Figure 3.10(b). The anisotropy parameter β_4 is found to be zero for all data presented in this chapter.

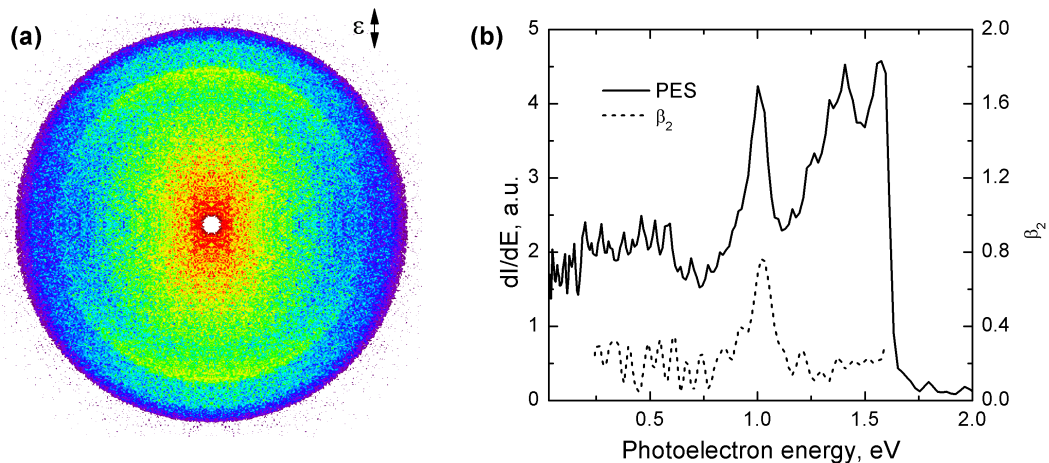


Figure 3.10: (a) Velocity map image recorded with a 240 nm pump pulse, a 300 nm probe pulse and a pump-probe delay of 5 fs. (b) Corresponding photoelectron spectrum (solid line) and eKE dependence of the anisotropy parameter, β_2 (dashed line).

3.4.2 Integrated photoelectron intensity

The evolution of the integrated photoelectron signal, following excitation of aniline at 269, 250, 240, 238 and 236 nm, is plotted as a function of time in Figures 3.11(a)-(b) and Figures 3.12(a)-(c). All the measured time-profiles exhibit dynamics on more than one timescale. We fit the experimental data to equation (3.6) which is a sum of exponentially decaying profiles convoluted with a Gaussian function representing the cross-correlation of the pump and probe laser pulses $g(t)$. The decay times are those determined from the fitting procedure described in Section 3.4.4 below and are listed in Table 3.1.

Following 269 nm excitation (Figure 3.11(a)), approximately 20% of the integrated photoelectron signal disappears during the first picosecond and the remaining 80% has a lifetime that is longer than one nanosecond. Following 250 nm excitation (Figure 3.11(b)), approximately 60% of the integrated photoelectron signal decays during the first picosecond and the remaining 40% decays on a timescale of around 600 ps. For 240, 238 and 236 nm excitation (Figures 3.12(a), (b) and (c)), approximately 75% of the photoelectron signal decays during the few hundred femtoseconds and this increases to around 85% after one picosecond. The remaining 15% of the signal then decays on a timescale of around 200 ps (240 nm), 100 ps (238 nm) or 81 ps (236 nm).

This energy-integrated analysis generates data similar to that reported by Castaño *et al.* [104]; it provides some information about timescales, but the intermediate electronic states involved in the electronic relaxation are not observed directly.

3.4.3 Time-resolved photoelectron spectra

The photoelectron kinetic energy spectra are plotted as a function of pump-probe delay, following excitation of aniline at 269 and 250 nm in Figures 3.11(c)-(d) and 240, 238 and 236 nm in Figures 3.12(d)-(f). These figures show that the fast decaying and slow decaying components of the total integrated photoelectron spectra have quite different eKE distributions.

To a first approximation, we can use the conservation of energy to assign the components of the photoelectron spectra. In rigid molecules that do not undergo large amplitude motion, there is a tendency for the excess vibrational energy in a given electronic state, $E_{\text{vib}} = h\nu_{\text{pump}} - E(S_n)$, to be approximately conserved during

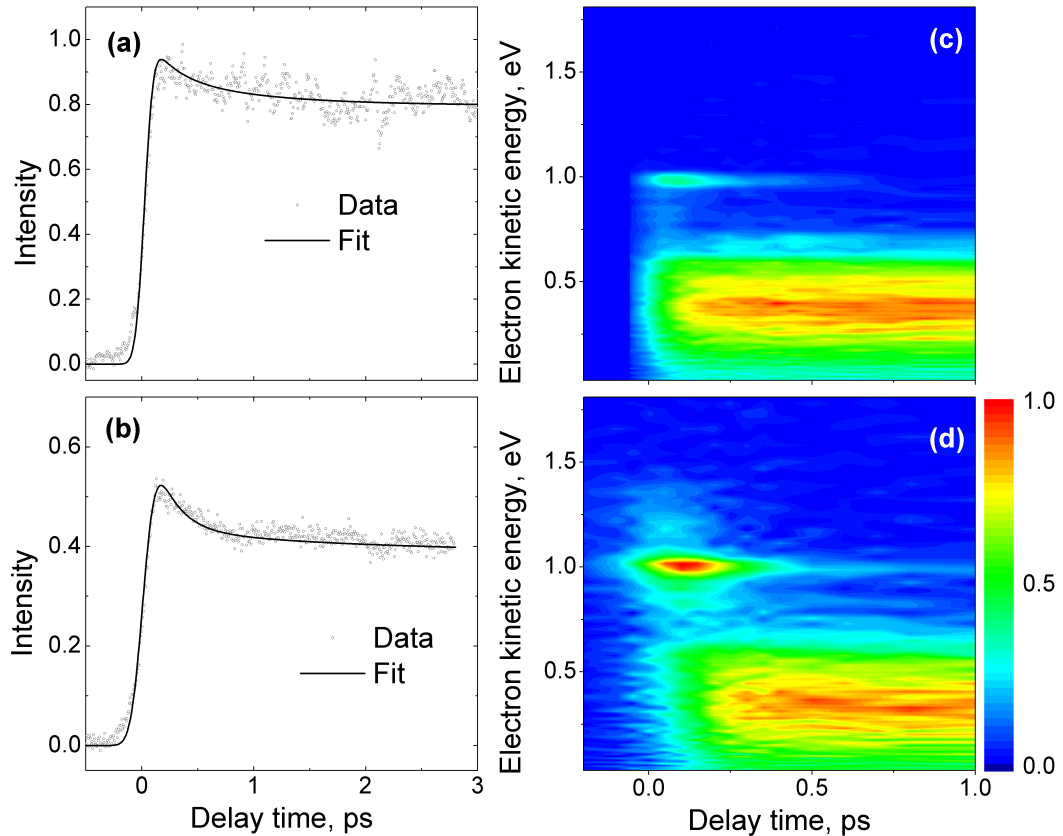


Figure 3.11: Time evolution of the integrated photoelectron signal following excitation of aniline at (a) 269 nm and (b) 250 nm: points represent experimental data, solid lines are fits to equation (3.6), vertical scales are normalised so that $\sum_i c_i = 1$ (equation (3.6)). Photoelectron kinetic energy spectra as a function of pump-probe delay following excitation of aniline at (c) 269 nm and (d) 250 nm.

photoionisation:

$$eKE = h\nu_{\text{probe}} - [E(D_n) - E(S_n)], \quad (3.3)$$

where D_n are the electronic states of the cation and have been determined to be 7.72 eV [117] and 9.03 eV [60] for the ground and first excited electronic states of the aniline cation, respectively. The 0-0 excitation energies of $S_1(\pi\pi^*)$ and $S_2(\pi 3s/\pi\sigma^*)$ have been determined to be 4.22 eV [117] and 4.60 eV [105], respectively. The theoretical value for the vertical excitation of the $S_3(\pi\pi^*)$ state is 5.34 eV [106]. To the best of our knowledge an accurate value for the 0-0 excitation energy of $S_3(\pi\pi^*)$ has not been reported, but as discussed in section 3.3.1 we estimate it to be around 5.1 eV from the gas-phase absorption spectrum (Figure 3.9). Using this information, we assign peaks in the photoelectron spectrum around 1.5 eV

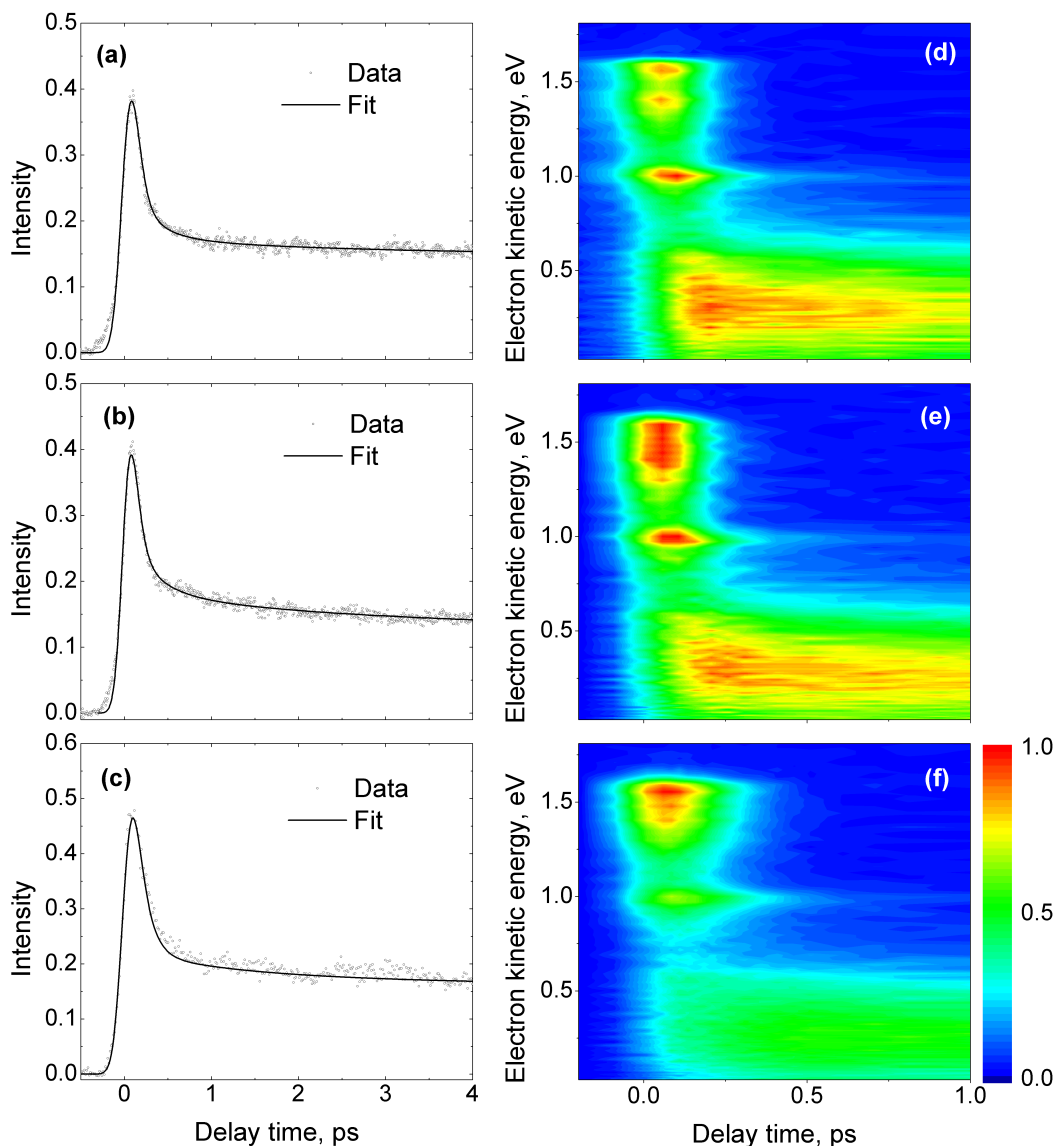


Figure 3.12: Time evolution of the integrated photoelectron signal following excitation of aniline at (a) 240 nm, (b) 238 nm and (c) 236 nm: points represent experimental data, solid lines are fits to equation (3.6), vertical scales are normalised so that $\sum_i c_i = 1$ (equation (3.6)). Photoelectron kinetic energy spectra as a function of pump-probe delay following excitation of aniline at (d) 240 nm, (e) 238 nm and (f) 236 nm.

and 1 eV to photoionisation from $S_3(\pi\pi^*)$ and the $\pi 3s$ component of $S_2(\pi 3s/\pi\sigma^*)$, respectively. The photoelectron spectrum at lower eKE (< 0.7 eV) is broad and vibrationally unresolved. Energetically, this region is most likely to correspond to photoionisation from $S_1(\pi\pi^*)$ or $S_2(\pi 3s/\pi\sigma^*)$. Ionisation from $S_3(\pi\pi^*)$ to D_1 is also possible (eKE < 0.2 eV) but is expected to be about 10 times weaker than ionisation

to the ground state of the cation [60].

The most intense features in the 240, 238 and 236 nm photoelectron spectra are the asymmetric bands visible at high eKE, which correspond to ionisation from $S_3(\pi\pi^*)$. As the pump-probe delay increases, the intensity of this band decreases very rapidly on a timescale of around one hundred femtoseconds. A short vibrational progression is visible in the 240 nm and 236 nm spectra with vibrational wavenumbers of approximately 1200 cm^{-1} and 604 cm^{-1} , respectively, and remains visible throughout the decay of both spectra.

The peak at 1 eV, corresponding to ionisation from the $\pi 3s$ component of the $S_2(\pi 3s/\pi\sigma^*)$ state, is visible in all five spectra; it is narrow and symmetric, as expected for Rydberg states that obey the $\Delta v = 0$ propensity rule during ionisation. From the eKE, we determine the origin of the $S_2(\pi 3s/\pi\sigma^*)$ state to be 4.6 eV, which is in excellent agreement with the more precise value of 37104 cm^{-1} (4.6003 eV) obtained using 2 + 2 resonance enhanced multiphoton ionisation [105]. The anisotropy parameter rises to a maximum value of around $\beta_2 = 1.1$ across this narrow peak, which is consistent with photoelectrons being ionised from a 3s Rydberg state. As the pump-probe delay increases, this feature decays less rapidly than $S_3(\pi\pi^*)$, but still on the timescale of hundreds of femtoseconds. Our observations suggest that the anisotropy of the $\pi 3s$ contribution is preserved during its decay (see Figure 3.13 (a)). The anisotropy change around 1 eV eKE at 240 nm excitation shown in Figure 3.13 (b) (red dots), is due to the significant signal contribution from the $S_3(\pi\pi^*)$ state as indicated in Figure 3.13 (d). A possible small drop in the anisotropy (red dots in Figure 3.13 (a)) around zero pump-probe delay can be also explained by a small photoelectron signal contribution from the $S_3(\pi\pi^*)$ state. Interestingly, the decay timescale does not appear to vary significantly between 269 nm excitation (resonant with the S_2-S_0 origin) and 236 nm (0.66 eV above the S_2 origin).

The broad band observed at low eKE has two components, with both visible in all five spectra. Following excitation at 250–236 nm, the lower eKE component has a Gaussian profile centered around 0.2–0.26 eV; it grows with a timescale of a few hundred femtoseconds and decays on a timescale that decreases monotonically with decreasing excitation wavelength (from 600 ps at 250 nm to around 81 ps at 236 nm). This band seems most likely to correspond to photoionisation from $S_1(\pi\pi^*)$. Following excitation at 269 nm, the low eKE component is asymmetric and has a maximum photoelectron intensity at 0.3 eV. The asymmetric shape arises

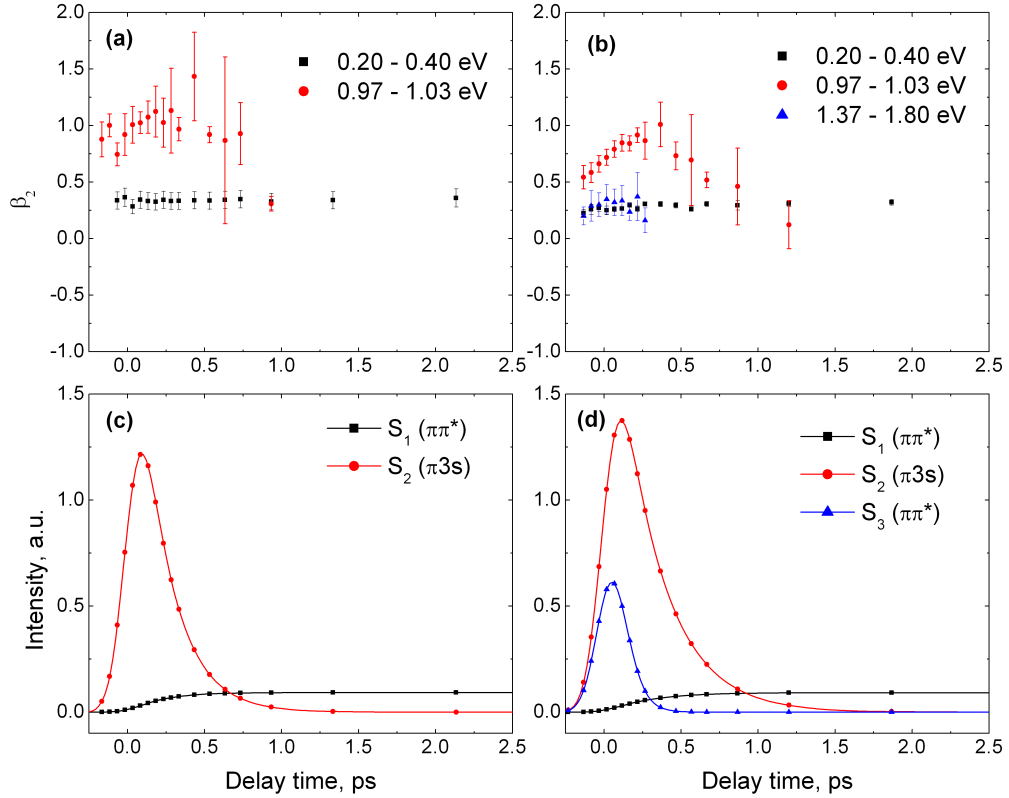


Figure 3.13: Photoelectron anisotropy parameter, β_2 , as a function of pump-probe delay time averaged over different photoelectron kinetic energy ranges for (a) 250 nm and (b) 240 nm excitation wavelengths. (c) and (d) An estimated photoelectron signal contributions to the 0.97-1.03 eV eKE range derived from equation (3.6) with the decay associated components (Figures 3.18 and 3.16) and lifetimes (Table 3.1) obtained from our analysis. The anisotropy distribution does not vary for the photoelectrons ionised from the $S_1(\pi\pi^*)$ state (0.2–0.4 eV energy range), the $S_3(\pi\pi^*)$ state (1.37–1.8 eV energy range) and the $\pi 3s$ state (0.97–1.03 eV energy range in (a)). The variation in the anisotropy parameter across the 0.97–1.03 eV energy range in (b) is most likely to be due to the overlapping contributions in the PES (see Figure 3.10 (b)) from the different electronic states which decay on a different time scale. The anisotropy is calculated as a weighted average over the indicated eKE range and the error bars correspond to one standard deviation.

because $S_1(\pi\pi^*)$ is also populated directly during the excitation process at this wavelength, as expected from the absorption spectrum. This band decays on a time scale >1 ns that we cannot measure in our experiment. In all five spectra, the higher eKE component of the broad photoelectron band, around 0.6 eV, decays on

a picosecond timescale; we believe this component corresponds to photoionisation from $S_2(\pi 3s/\pi\sigma^*)$ (see section 3.6).

3.4.4 Timescales

To extract timescales, we fit our experimental photoelectron spectra to a sum of exponentially decaying spectral profiles convoluted with a Gaussian cross-correlation of the pump and probe laser pulses $g(t)$,

$$S(\text{eKE}, t) = \sum_i c_i(\text{eKE}) e^{-t/\tau_i} \otimes g(t), \quad (3.4)$$

where $c_i(\text{eKE})$ is the intensity of the i th decay at a given eKE and τ_i is its corresponding $1/e$ decay time. Equation (3.4) clearly separates the molecular dynamics function, $I(\text{eKE}, t)$ from the instrument function, $g(t)$, where:

$$I(\text{eKE}, t) = \sum_i c_i(\text{eKE}) e^{-t/\tau_i}. \quad (3.5)$$

At zero pump-probe delay time ($t = 0$) equation (3.5) is simply a sum of all decay associated components which represents a photoelectron spectrum of the initially excited electronic states.

Multidimensional fitting procedures are prone to finding local minima, especially if there are a large number of parameters to fit. We avoid this by fitting discernible portions of the photoelectron spectra in turn, rather than fitting all the parameters simultaneously. An integration over a specific energy range (E_1 to E_2) simplifies equation (3.4):

$$S(t) = \sum_i c_i e^{-t/\tau_i} \otimes g(t), \quad (3.6)$$

where τ_i is the i th $1/e$ decay time and $c_i = \int_{E_1}^{E_2} c_i(\text{eKE}) d(\text{eKE})$ is its corresponding intensity, which is proportional to the product of the excited state population and the photoionisation cross-section. A detailed description of the data analysis and the precise form of the equations (3.4) and (3.6) are presented in chapter 2.7. The $1/e$ decay times obtained from the fit to equation (3.6) are summarised in Table 3.1.

First, the lifetime of the long-lived component of the broad, Gaussian shaped band at low eKE, τ_0 , is determined by fitting the total photoelectron counts from 0 to 400 ps to a single exponential decay.

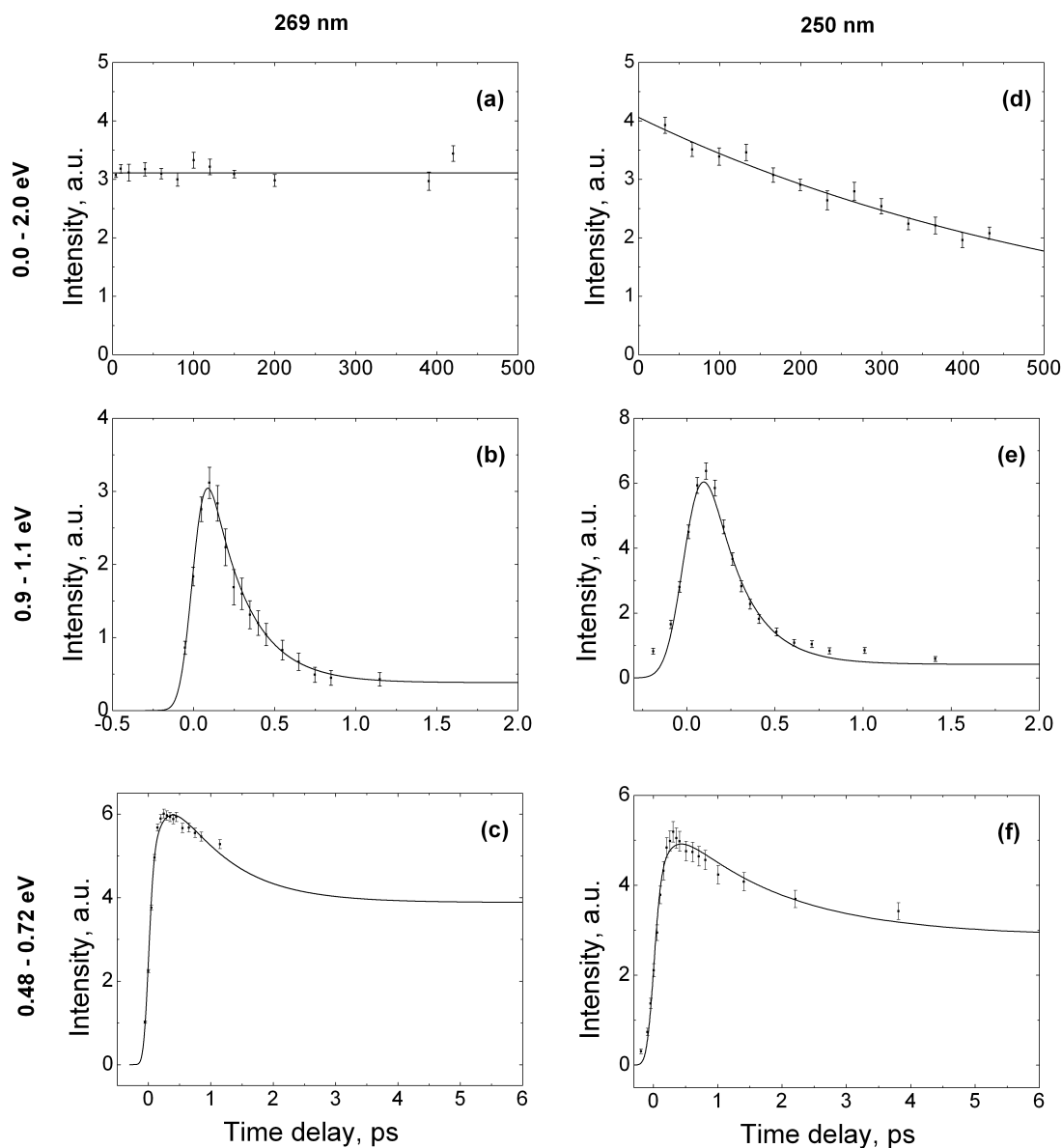


Figure 3.14: Integrated photoelectron counts as a function of pump-probe delay following excitation at 269 nm (a-c) and 250 nm (d-f): experimental data (points with error bars representing one standard deviation) and fits (solid lines). (a) and (d) Total photoelectron signal as a function of pump-probe delay. (b) and (e) Photoelectron signal integrated over the sharp peak in the photoelectron spectrum (0.9 eV to 1.1 eV). (c) and (f) Photoelectron signal integrated over the low energy part of the photoelectron spectrum (0.48 eV to 0.72 eV).

For the 269 nm and 250 nm data, the decay time of the $3s$ component of $S_2(\pi 3s/\pi\sigma^*)$, τ_2 , the cross-correlation, $g(t)$, and zero-time were determined by fitting the photoelectron signal integrated over the range 0.9 – 1.1 eV with two decays, one of which was fixed to τ_0 . The decay time associated with the shorter lived 0.6 eV

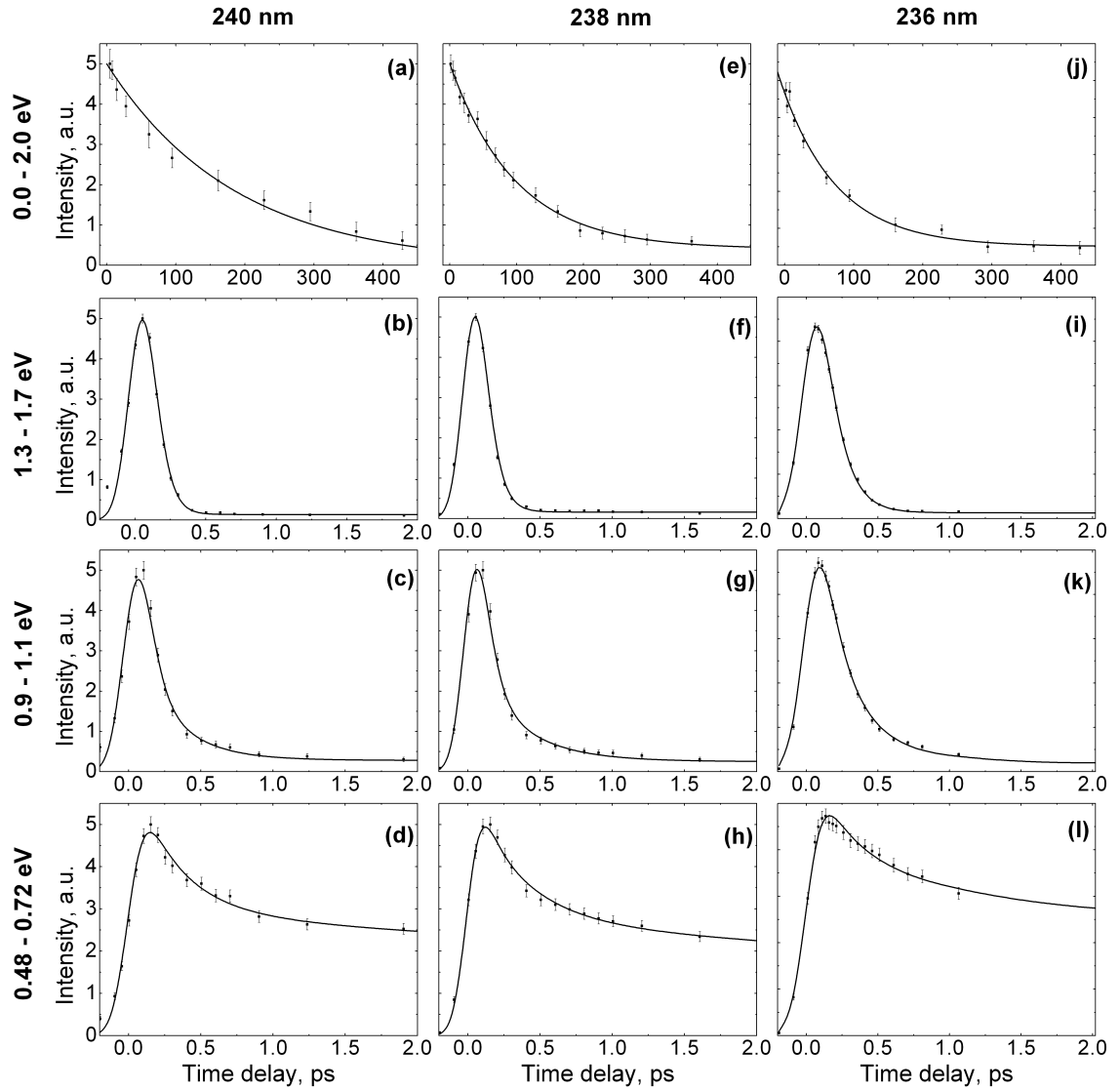


Figure 3.15: Integrated photoelectron counts as a function of pump-probe delay following excitation at 240 nm (a-d), 238 nm (e-h) and 236 nm (j-l): experimental data (points with error bars representing one standard deviation) and fits (solid lines). (a), (e) and (j) Total photoelectron signal as a function of pump-probe delay. (b), (f) and (i) Photoelectron signal integrated over the high eKE part of the spectra (1.3 - 1.7 eV). (c), (g) and (k) Photoelectron signal integrated over the sharp peak in the photoelectron spectrum (0.9 eV to 1.1 eV). (d), (h) and (l) Photoelectron signal integrated over the low energy part of the photoelectron spectrum (0.48 eV to 0.72 eV).

shoulder of the broad band at low eKE, τ_1 , was then determined from the fit of the photoelectron signal integrated over the range 0.48 – 0.72 eV to three decays, where two of the time constants were fixed to τ_0 and τ_2 .

For the 240 nm, 238 nm and 236 nm data, the decay time of the $S_3(\pi\pi^*)$ component, τ_3 , the cross-correlation, $g(t)$, and zero-time were determined by fitting the photoelectron signal integrated over the range 1.3 – 1.7 eV to equation (3.6) with two decays, one of which is τ_0 . The decay time of the 3s component of $S_2(\pi 3s/\pi\sigma^*)$, τ_2 , was then obtained by fitting the integrated photoelectron counts over the range 0.9 – 1.1 eV with three decays, two of which were fixed to τ_0 and τ_3 . Finally, the decay time associated with the shorter lived 0.6 eV shoulder of the broad band at low eKE, τ_1 , was determined from the fit of the photoelectron signal integrated over the range 0.48 – 0.72 eV to four decays, where three of the time constants were fixed to τ_0 , τ_2 and τ_3 .

Integrated photoelectron counts and fits across discernible portions of the time-resolved photoelectron spectra, following excitation at 269, 250, 240, 238 and 236 nm are presented in Figure 3.14 and Figure 3.15.

Table 3.1: Summary of 1/e decay lifetimes extracted from the fitting procedures described in the text.

| Pump wavelength (nm) | $S_3(\pi\pi^*)$ lifetime (fs) | $S_2(\pi 3s)$ lifetime (fs) | $S_2(\pi 3s/\pi\sigma^*)$ lifetime (ps) | $S_1(\pi\pi^*)$ lifetime (ps) | Cross-correlation FWHM (fs) |
|----------------------|-------------------------------|-----------------------------|---|-------------------------------|-----------------------------|
| 269 | - | 230 ± 70 | $0.9^{+0.9}_{-0.3}$ | > 1 ns | 150 ± 45 |
| 250 | - | 200 ± 45 | $1.6^{+2.0}_{-0.8}$ | 600 ± 35 | 200 ± 40 |
| 240 | 65 ± 20 | 280 ± 170 | $1.8^{+4.7}_{-1.5}$ | 185 ± 15 | 210 ± 20 |
| 238 | 70 ± 15 | 330 ± 150 | $2.4^{+4.8}_{-1.1}$ | 100 ± 10 | 185 ± 15 |
| 236 | 116 ± 13 | 259 ± 113 | $1.2^{+4.1}_{-0.8}$ | 81 ± 10 | 210 ± 20 |

3.4.5 Relaxation pathway

Using the 1/e lifetimes summarised in Table 3.1, the time-resolved photoelectron spectra for 269 and 250 nm excitation were fitted to equation (3.4) over the entire energy range to obtain the spectra associated with each of the decay times, $c_i(\text{eKE})$. As equation (3.4) fits a series of exponentially decaying functions that have zero pump-probe as their origin, positive values of $c_i(\text{eKE})$ correspond to exponential decay and negative values of $c_i(\text{eKE})$ correspond to exponential growth. Such a representation has been shown to be a valuable method for unraveling relaxation

mechanisms from time-resolved photoelectron spectra as long as exponential kinetics are valid [136, 137, 138].

The results of the fits to the data are shown in Figure 3.16(a) and (b). The spectra associated with the 230 fs (269 nm) and 200 fs (250 nm) timescales have positive amplitude components in the region of the photoelectron spectrum corresponding to the sharp $\pi 3s$ Rydberg component of $S_2(\pi 3s/\pi\sigma^*)$, at 1 eV, and negative amplitude components in the region of the photoelectron spectrum corresponding to photoionisation from $S_1(\pi\pi^*)$, at low eKE. This suggests that population flows from the $\pi 3s$ component of $S_2(\pi 3s/\pi\sigma^*)$ to $S_1(\pi\pi^*)$ on the timescale of a couple of hundred femtoseconds. The spectra associated with the longest lifetimes (> 1 ns for 269 nm and 600 ps for 250 nm) approximately mirror the negative amplitude components of the spectra associated with the 230 fs and 200 fs lifetimes. The spectra associated with the 0.9 ps (269 nm) and 1.6 ps (250 nm) timescales have large errors associated with them, suggesting that fitting exponential kinetics is not as appropriate for this component as it is for the others. This is discussed in more detail below. The sums of the coefficients $c_i(\text{eKE})$ represent the photoelectron spectra of the initially populated states. They suggest that for 269 nm, both $S_1(\pi\pi^*)$ and $S_2(\pi 3s/\pi\sigma^*)$ are populated during the initial excitation process but that for 250 nm, only $S_2(\pi 3s/\pi\sigma^*)$ is populated significantly, as we might expect from the absorption spectrum (Figure 3.9(b)). The time-resolved photoelectron spectra can be reconstructed using the timescales τ_i and coefficients $c_i(\text{eKE})$ obtained from the fitting procedure and are seen to reproduce all the dynamical features of the experimental spectra (compare Figures 3.16(d) and (e) with Figures 3.11(c) and (d), respectively).

Similar procedures were employed to analyse the decay associated spectra following 236 nm excitation. The time-resolved photoelectron spectra are fitted to equation (3.4) over the entire energy range to obtain the spectra associated with each of the decay times, $c_i(\text{eKE})$ ($i = 0 - 3$). The result of the fit to our data is shown in Figure 3.16(c). The spectrum associated with the 116 fs timescale is dominated by an intense, positive amplitude feature that represents the $S_3(\pi\pi^*)$ photoelectron spectrum. The spectrum associated with the 259 fs timescale has a positive amplitude component in the region of the photoelectron spectrum corresponding to the sharp $\pi 3s$ component of $S_2(\pi 3s/\pi\sigma^*)$ at 1.0 eV and a negative amplitude component in the region of the photoelectron spectrum corresponding to

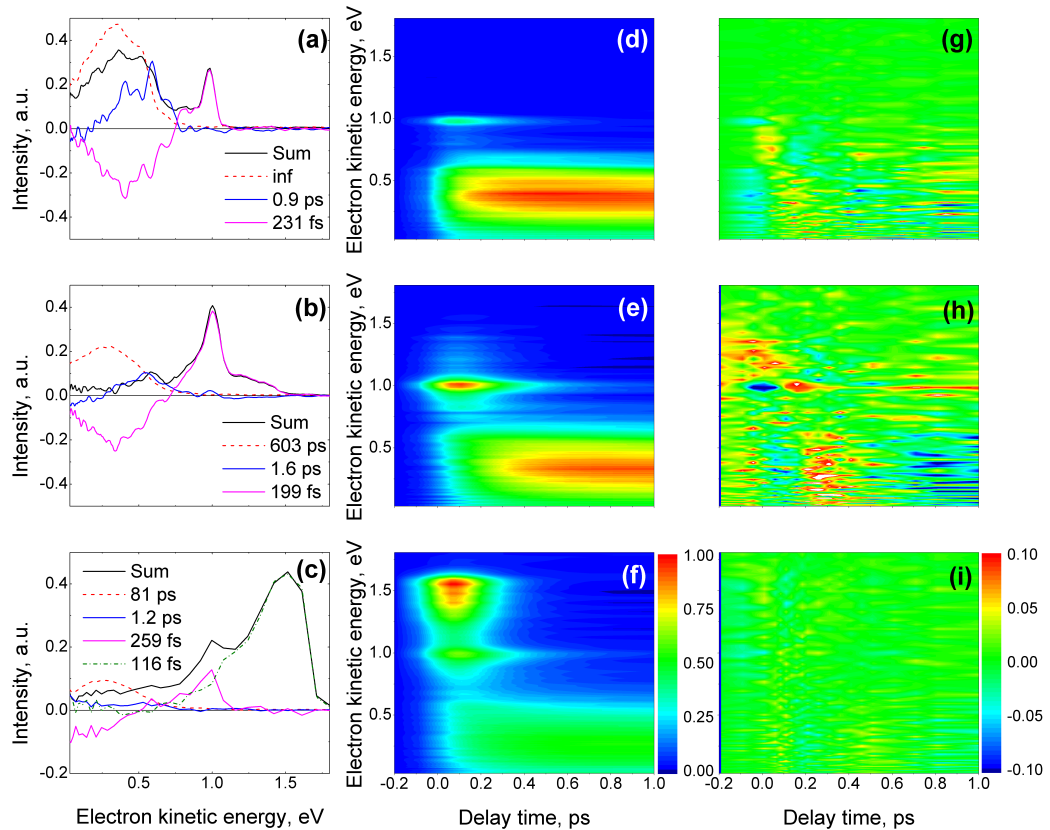


Figure 3.16: Spectral components of the three decays derived using the fitting procedure described in the text for (a) 269 nm, (b) 250 nm and (c) 236 nm excitation. Modelled photoelectron spectra for (d) 269 nm, (e) 250 nm and (f) 236 nm excitation, using the timescales listed in Table 3.1. Residuals: difference between the experimental and modelled photoelectron spectra for (g) 269 nm, (h) 250 nm and (i) 236 nm excitation.

$S_1(\pi\pi^*)$, suggesting that population flows from the $\pi 3s$ component of $S_2(\pi 3s/\pi\sigma^*)$ to $S_1(\pi\pi^*)$. The spectrum associated with the 81 ps timescale approximately mirrors the shape of the negative amplitude component of the spectrum associated with the 259 fs decay. The spectrum associated with the 1.2 ps timescale is very weak and has a large error associated with it. The sum of the coefficients $c_i(\text{eKE})$ is also plotted in Figure 3.16(c). According to equation (3.5), the sum excludes any dynamics and represents the photoelectron spectrum of the initially excited states and confirms that both $S_3(\pi\pi^*)$ and $S_2(\pi 3s/\pi\sigma^*)$ are populated during the initial excitation process. The time-resolved photoelectron spectrum $S(\text{eKE}, t)$ is reconstructed using equation (3.4) and presented in Figure 3.16(f). The reconstructed

photoelectron spectra can be seen to reproduce all the dynamical features of the experimental plot extremely well.

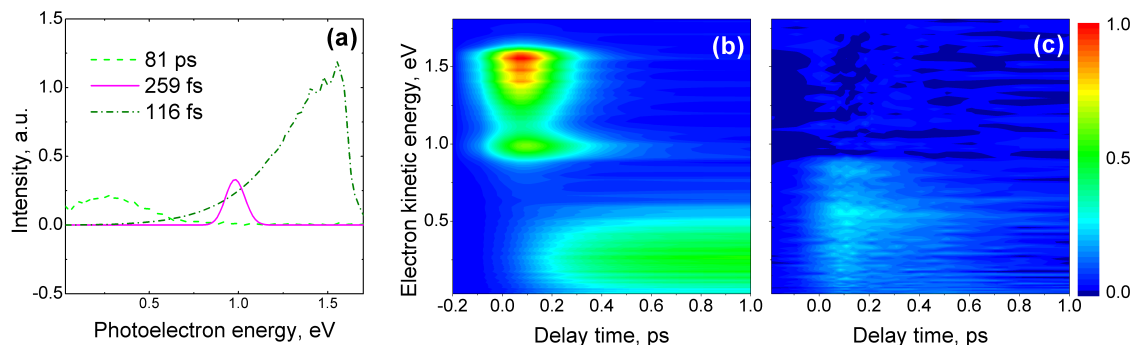


Figure 3.17: (a) Smoothed photoelectron spectral profiles for 236 nm. (b) Reconstructed photoelectron spectra, using timescales listed in Table 3.1 and the smoothed profiles presented in (a). (c) Difference spectra for 236 nm excitation, as described in the text.

To investigate the spectrum associated with the 1.2 ps timescale further, the time-resolved photoelectron spectra at 236 nm were modelled using the timescales, cross-correlation width and smoothed spectral profiles of S_3 , $3s$ and S_1 obtained from our fitting procedure (see Figure 3.17). The profile of S_3 is modelled with a smooth monotonic tail, the $3s$ component of S_2 is modelled with a Gaussian profile and the shape of S_1 is fixed to be the long-time profile. It is assumed that the rise time of S_1 is equal to the decay time of the $3s$ component of S_2 ($\pi 3s/\pi\sigma^*$). The modelled spectra (Figure 3.17 (b)) were then subtracted from the experimental photoelectron spectra (Figure 3.12 (f)) to obtain the difference spectra (Figure 3.17 (c)). The difference spectra show that the higher eKE component decays faster than the lower eKE component. We propose that this feature corresponds to motion of population on the $S_2(\pi 3s/\pi\sigma^*)$ potential energy surface. Restricting the rise of the S_1 state localises the decay time of the difference spectra towards the short lifetime end of the error margin obtained from the unrestricted fit in Figure 3.16.

It was not possible to determine the spectra associated with the various decay times for 240 and 238 nm excitation using the same procedure that was employed for 269, 250 and 236 nm. The main reason for this is that probably there are too many exponential contributions to the low eKE part of the photoelectron spectrum (0 – 0.7 eV) at short delays and the photoelectron signal contribution from the $S_1(\pi\pi^*)$ state is too low compared to the contribution from the $S_2(\pi 3s/\pi\sigma^*)$ state.

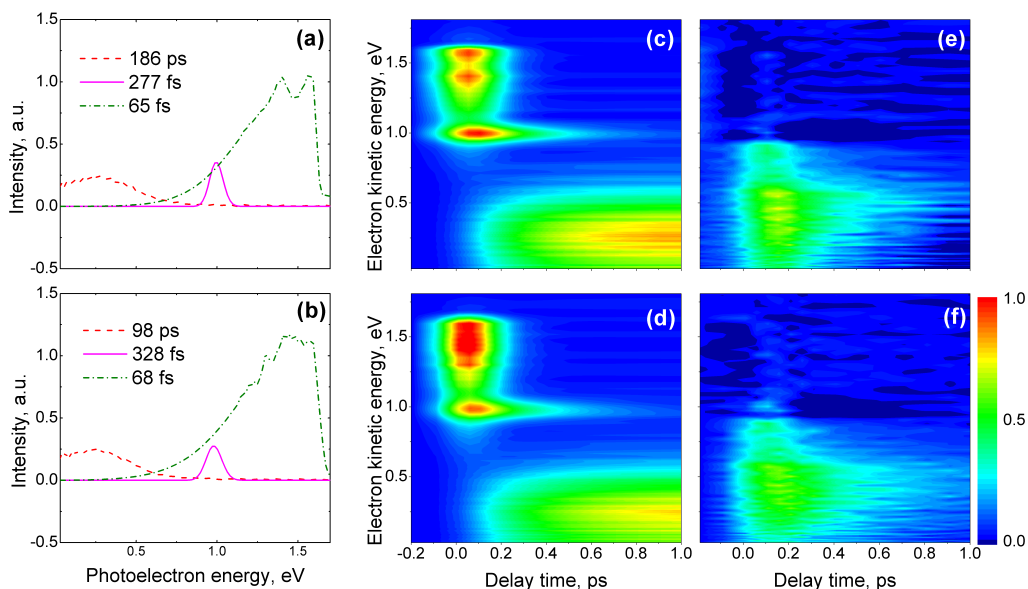


Figure 3.18: Smoothed photoelectron spectral profiles for (a) 240 nm and (b) 238 nm excitation. Reconstructed photoelectron spectra for (c) 240 nm and (d) 238 nm excitation, using timescales listed in Table 3.1 and the smoothed profiles presented in (a) and (b) of this Figure. Difference spectra for (e) 240 nm and (f) 238 nm excitation, as described in the text.

After further analysis (see text below) we found that photoelectron intensity from the $S_2(\pi 3s/\pi\sigma^*)$ state is larger for 240 and 238 nm excitation compared to 236 nm excitation (compare Figure 3.17 (c) to Figures 3.18 (e) and (f)). The estimated ratios of the peak photoelectron intensity produced from the $S_1(\pi\pi^*)$ component (maximum intensity taken from Figures 3.17 (b) and 3.18 (c),(d) at $t = 1$ ps) to the one produced from the $S_2(\pi 3s/\pi\sigma^*)$ shoulder component (maximum intensity taken from Figures 3.17 (c) and 3.18 (e),(f) at $t = 0.15$ ps) are 2, 1.3 and 1.1 for 236 nm, 238 nm and 240 nm excitation, respectively. The contribution from the $S_1(\pi\pi^*)$ component is the largest at 236 nm excitation. Thus, it is more likely to reveal the growth of the $S_1(\pi\pi^*)$ component at 236 nm than at 238 nm or 240 nm excitation wavelengths.

Instead of using the quasi-global fitting approach, the dynamics for 238 nm and 240 nm excitation were modelled using the $1/e$ lifetimes summarised in Table 3.1, together with the fitted cross-correlations and smoothed photoelectron spectral profiles deduced from the time-resolved photoelectron spectra. This approach is shown

to work for analysis of the 236 nm excitation data (Figure 3.17). The profiles for $S_3(\pi\pi^*)$ were modelled using the experimental spectral profiles for the 1.2 – 1.7 eV range and adding a smooth monotonic tail. The $\pi 3s$ component of $S_2(\pi 3s/\pi\sigma^*)$ was modelled using a Gaussian profile (FWHM = 0.1 eV) centered at 1 eV. The $S_1(\pi\pi^*)$ shape was fixed to the long time (>7 ps) profile. The spectral shapes are presented in Figures 3.18(a) and (b).

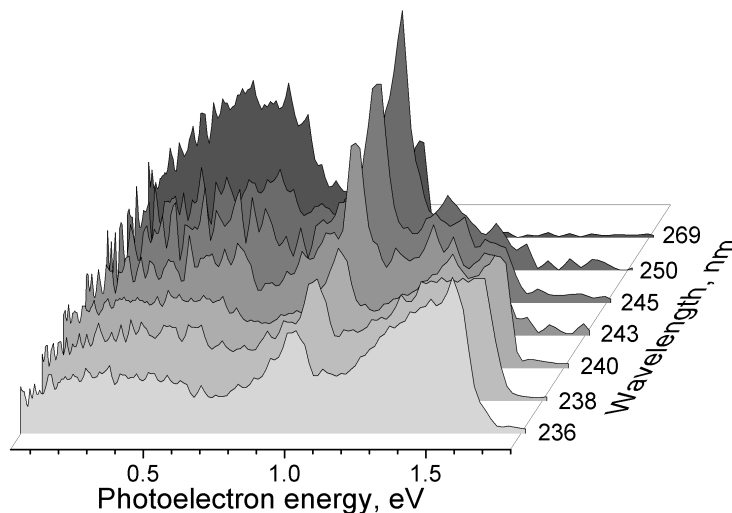


Figure 3.19: Photoelectron energy spectra for different excitation wavelengths and a 300 nm ionisation pulse. All spectra are acquired at around zero delay between the pump and the probe laser pulses. The area under each photoelectron spectrum is normalised to the same number in order to illustrate the change in the shape of the photoelectron spectrum.

It is assumed that only $S_3(\pi\pi^*)$ and $S_2(\pi 3s/\pi\sigma^*)$ (including the $\pi 3s$ component) are populated during the initial excitation and that the rise of population in $S_1(\pi\pi^*)$ equals the decay of the population from the $\pi 3s$ component of $S_2(\pi 3s/\pi\sigma^*)$. This has been shown to be the case for 269, 250 nm and 236 nm; although, at 269 nm a large fraction of $S_1(\pi\pi^*)$ is also populated directly. Using these assumptions, the relative amplitudes of the three spectral components were fitted to the experimental data and the resulting models are presented in Figure 3.18(c) and (d). These modelled spectra were then subtracted from the experimental photoelectron spectra (Figure 3.12(g) and (h)) to obtain difference spectra (Figure 3.18(e) and (f)).

The difference spectra represent the photoelectron spectra of the fast component in the low eKE range (0–0.7 eV) and show a variation in lifetime across the

photoelectron spectrum. This variation could account for the discrepancy in the fits shown in Figures 3.14 (c),(f) and 3.15 (d),(h),(l), however, it is not possible to add more decay components in the fit because the minimisation task becomes overparametrised and does not converge to a meaningful answer. The average decay times of the difference spectra are faster than the decays listed in Table 3.1 due to the restriction on the rise of the $S_1(\pi\pi^*)$ population. The difference spectra appear to be shifting to lower eKEs on a sub-hundred femtosecond timescale.

The evolution of the PES as a function of excitation wavelength is shown in Figure 3.19. The relative intensity of the $S_3(\pi\pi^*)$ contribution is growing with the excitation wavelengths while the relative contribution of the $S_2(\pi 3s/\pi\sigma^*)$ state is decreasing.

3.5 TRPEI investigation of deuterated aniline

3.5.1 Experimental method

The non-adiabatic dynamics in the fully deuterated aniline (aniline- D_7) molecule were also investigated using the femtosecond TRPEI experiment technique, with a 260 nm excitation pulse and a 305 nm photoionisation pulse. The TRPEI measurements of aniline- D_7 were performed using the same apparatus described in section 2.4. Deuteration of aniline changes its mass but does not change the charge distribution, thus the energy level diagram shown in Figure 3.9 can be used to locate the electronic energies for aniline- D_7 . On the other hand, the change in the atomic mass alters the vibrational frequencies [139] and, most importantly, dynamics dependent on the N–H/D stretch coordinate are expected to be slower in the deuterated molecule. A 260 nm (4.77 eV) UV photon has enough energy to excite aniline- D_7 above the origin of the $S_2(\pi 3s/\pi\sigma^*)$ electronic state. A 305 nm (4.07 eV) probe wavelength is chosen to ionise all the excited singlet states but below the significant single photon absorption to the $S_1(\pi\pi^*)$ state. The cross-correlation of the pump and the probe pulses in these experiments was 171 fs. The molecular beam is created by passing He gas through liquid aniline- D_7 (Sigma-Aldrich, 98%) at 750 mbar and expanding into the vacuum chamber through a 50 μm nozzle. The experimental conditions and data analysis procedures are exactly the same as already described in section 3.4.

3.5.2 Time-resolved photoelectron spectra

An example of the velocity map image and corresponding photoelectron spectrum and anisotropy parameter, β_2 , of aniline-D₇ using 260 nm pump and 305 nm probe pulses is shown in Figure 3.20. This spectrum looks very similar to the spectrum of aniline with 250 nm pump and 300 nm probe pulses: it features a sharp photoelectron peak at around 0.97 eV and a broad unresolved photoelectron profile at a low eKE (< 0.7 eV). The assignment of the electronic state in the aniline-D₇ photoelectron spectra is identical to the undeuterated aniline. Based on the energy arguments presented in section 3.4.3, the sharp photoelectron peak is associated with the ionisation from the $\pi 3s$ component of the $S_2(\pi 3s/\pi\sigma^*)$ state. The narrow width (0.1 eV) and high anisotropy ($\beta_2 \approx 1$) of this feature in the photoelectron spectrum provides additional evidence towards its origin – photoionisation from the electronic state with 3s Rydberg character. The low energy (< 0.7 eV) unresolved photoelectron band corresponds energetically either to ionisation from the $S_1(\pi\pi^*)$ or $S_2(\pi 3s/\pi\sigma^*)$ states.

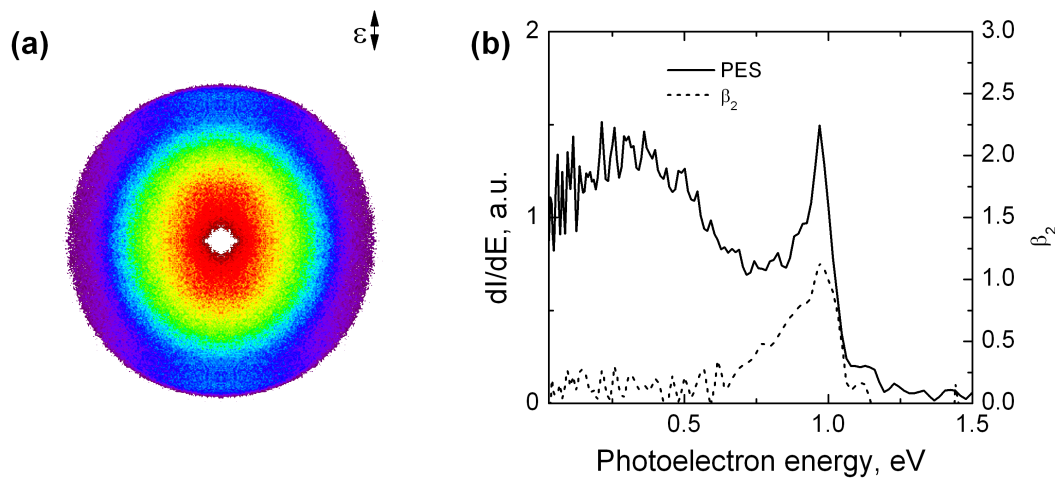


Figure 3.20: (a) Velocity map image recorded with a 260 nm pump pulse, a 305 nm probe pulse and a pump-probe delay of 3 fs. (b) Corresponding photoelectron spectrum (solid line) and eKE dependence of the anisotropy parameter, β_2 (dashed line).

The integrated photoelectron intensity and time dependent photoelectron spectra are shown in Figure 3.21. The total photoelectron signal rises to a maximum value on a 200 fs timescale and it can be modelled as a step function convoluted with the pump-probe cross-correlation function. More information about the dynamics can be obtained from the time-resolved photoelectron spectra presented in Figure 3.21 (b).

The sharp photoelectron peak associated with the $\pi 3s$ component of the $S_2(\pi 3s/\pi\sigma^*)$ state rises within the pump-probe cross-correlation time (171 fs) and decays on a similar time scale. The low energy part of the photoelectron spectrum (< 0.7 eV) has a similar rise time. However, the energy distribution of this portion of the spectrum changes from a flat profile at early time delays (< 200 fs) to a Gaussian shape at longer time delays (> 300 fs). The Gaussian profile is centered around 0.25 eV photoelectron energy and remains unchanged over the measured pump-probe delay time between 300 fs and 1.5 ps.

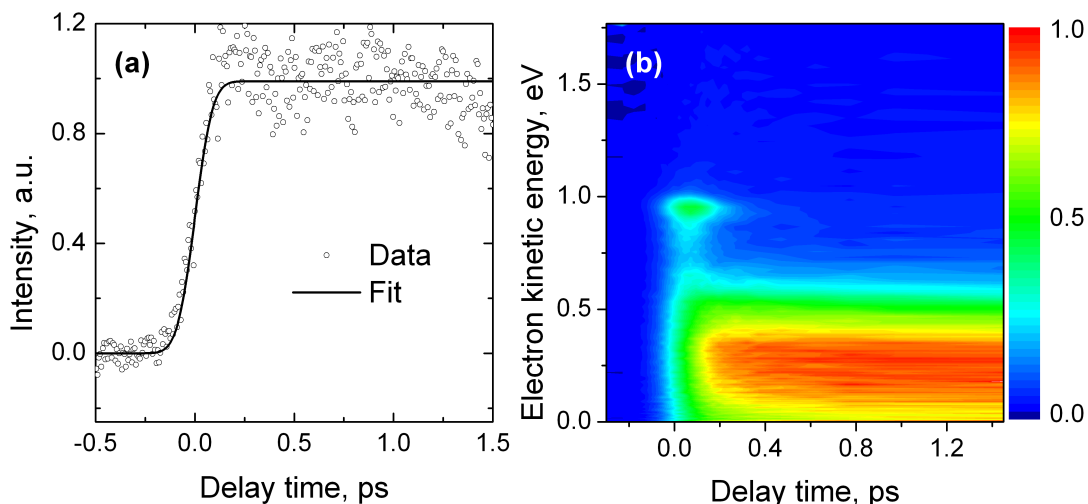


Figure 3.21: (a) Time evolution of the integrated photoelectron signal and (b) the photoelectron kinetic energy spectra as a function of pump-probe delay following excitation of deuterated aniline at 260 nm and ionisation with 305 nm.

3.5.3 Timescales

Further analysis of the TRPES shown in Figure 3.21 (b) is performed in a similar manner to the aniline data described in section 3.4.4. The timescales are obtained from the fit of the integrated signal over different portions of the photoelectron spectra to equation (3.6) which is the sum of exponential functions convoluted with Gaussian cross-correlation function. Integration over discrete portions of the photoelectron spectrum is used to isolate the contributions of the different electronic states to the photoelectron spectra.

As in the case of the aniline photoelectron spectrum, the long lived low eKE Gaussian profile is associated with ionisation from the $S_1(\pi\pi^*)$ state. Although picosecond pump-probe delay measurements for aniline- D_7 were not recorded, it

is not unreasonable to assume that the $S_1(\pi\pi^*)$ decay time in aniline- D_7 is of the order of the $S_1(\pi\pi^*)$ lifetime in aniline which is longer than 600 ps. Thus it is safe to approximate the $S_1(\pi\pi^*)$ decay time as infinity ($\tau_0 = \infty$) when analysing the time-resolved data up to 1.5 ps pump-probe delays.

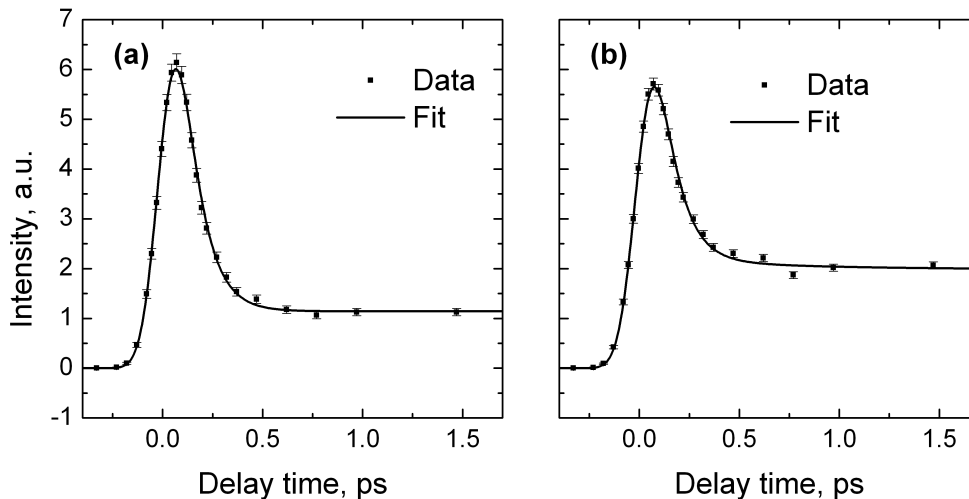


Figure 3.22: Integrated photoelectron counts as a function of pump-probe delay following excitation at 260 nm. (a) Photoelectron signal integrated over the sharp peak in the photoelectron spectrum (0.87 eV to 1.07 eV) and (b) Photoelectron signal integrated over the low energy part of the photoelectron spectrum (0.48 eV to 0.72 eV).

The majority of the photoelectron signal in the eKE range 0.87 eV to 1.07 eV originates from the photoionisation of the $\pi 3s$ component of the $S_2(\pi 3s/\pi\sigma^*)$ state. The integrated photoelectron intensity over this range, as a function of the pump-probe delay, is shown in Figure 3.22 (a). The solid line shows the fit of two exponential decays convoluted with a Gaussian cross-correlation function. One of the decay times is fixed to τ_0 and the decay time of the $\pi 3s$ component, τ_1 , the cross-correlation width and zero-time are all fitted together. As a result of the fit, $\tau_2 = 94 \pm 22$ fs is determined as the 1/e lifetime of the $\pi 3s$ component of the $S_2(\pi 3s/\pi\sigma^*)$ state.

A prominent change in shape of the low energy part of the photoelectron spectrum is observed in the eKE range 0.5 eV to 0.7 eV. The integrated intensity over this eKE range versus pump-probe delay time is shown in Figure 3.22 (b). The experimental data are fitted to the sum of three exponential decays, where two of them are fixed to τ_0 and τ_1 . This gave a third decay time $\tau_2 = 650$ fs.

3.5.4 Relaxation pathway

The $1/e$ lifetimes obtained in the previous section are used to obtain decay associated spectra (see section 3.4.4). The data set shown in Figure 3.21 (b) is fitted to equation (3.4) across the entire eKE range with three fixed lifetimes, τ_0 , τ_1 and τ_2 . The decay associated spectral coefficients, $c_i(\text{eKE})$, the modelled photoelectron spectrum and the residuals are shown in Figures 3.23. The spectrum associated with 94 fs has a positive amplitude at 0.97 eV which represents the $S_2(\pi 3s)$ state and a negative component in the region of the $S_1(\pi\pi^*)$ state. The negative component corresponds to the exponential rise in this eKE region. This suggests that the population flows from the $\pi 3s$ component of the $S_2(\pi 3s/\pi\sigma)$ state into the $S_1(\pi\pi^*)$ state. The spectrum with the infinite lifetime approximately mirrors the negative component associated with 94 fs rise time. The spectrum associated with the 650 fs lifetime has a small amplitude and is attributed to the ionisation from the $S_2(\pi 3s/\pi\sigma^*)$ state.

The sum of all the spectral components (black solid line in Figure 3.23 (a)) shows the spectrum at zero-delay time and corresponds to the initially excited profile of the photoelectron spectrum. The zero-delay spectrum confirms that the $\pi 3s$ state is excited directly, together with the low eKE component with the maximum around 0.7 eV. The origin of the initially excited low eKE part is assigned to ionisation from the $\pi\sigma^*$ component of the $S_2(\pi 3s/\pi\sigma^*)$ state using the arguments discussed in section 3.6. The modelled photoelectron spectrum shown in Figures 3.23 (b) is obtained from the decay associated spectra and the decay times and it reproduces the experimental data (Figure 3.21 (b)) well.

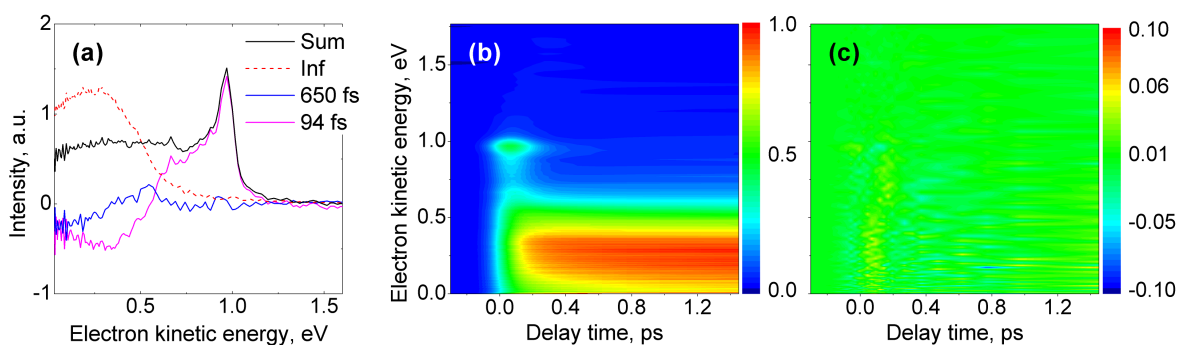


Figure 3.23: Summary of the fit with three decay components for 260 nm excitation. (a) spectral components, (b) modelled photoelectron spectra and, (c) the difference between the experimental and modelled photoelectron spectra.

3.6 Discussion

3.6.1 $S_2(\pi 3s/\pi\sigma^*)$

Our experiments show that the $S_2(\pi 3s/\pi\sigma^*)$ state is populated directly at all wavelengths. The $\pi 3s$ Rydberg component of $S_2(\pi 3s/\pi\sigma^*)$ decays on a timescale of a couple of hundred femtoseconds. For 269, 250 and 236 nm, the spectra associated with the $1/e$ decay of the $\pi 3s$ component of $S_2(\pi 3s/\pi\sigma^*)$ (Figure 3.16) have negative amplitudes in the region of the photoelectron spectrum corresponding to photoionisation from $S_1(\pi\pi^*)$. This suggests that there is an efficient mechanism for transferring population from the Rydberg component in the Franck-Condon region of $S_2(\pi 3s/\pi\sigma^*)$ to the $S_1(\pi\pi^*)$ state, through an S_2/S_1 conical intersection (Figure 3.9). This model also fits the data well for 240 and 238 nm excitation (Figure 3.18(c) and (d)). The anisotropy of the $\pi 3s$ component is preserved during the decay (Figure 3.13 (a)), suggesting that the S_2/S_1 conical intersection is located before the barrier in the vertical Franck-Condon region (Figure 3.6). Within experimental error, the timescale of S_2/S_1 internal conversion is independent of excitation energy above the S_2 origin (in the range 0–0.65 eV), suggesting that the vibrational mode connecting the vertical Franck-Condon region with the S_2/S_1 conical intersection seam is independent of excitation energy. The TRPEI experimental results on aniline- D_7 are very similar to the aniline TRPEI results. The results reveal the same population flow from the $\pi 3s$ component of the $S_2(\pi 3s/\pi\sigma^*)$ state to the $S_1(\pi\pi^*)$ state, through an S_2/S_1 conical intersection. The lifetime of the $\pi 3s$ component in aniline- D_7 is shorter than the corresponding lifetime in aniline (see Figure 3.24 (a)) and therefore it is unlikely that tunneling is a significant decay pathway from the $S_2(\pi 3s/\pi\sigma^*)$ state. If a significant amount of the $S_2(\pi 3s/\pi\sigma^*)$ population dissociates *via* tunneling its lifetime will be longer for aniline- D_7 than for aniline due to the mass difference between D and H.

The difference in the lifetime of the $S_2(\pi 3s)$ component between aniline- D_7 and aniline can be explained due to the higher density of the vibrational states and increased vibronic coupling in aniline- D_7 . In addition, a longer probe wavelength (305 nm compared to 300 nm for aniline) accesses a slightly different region of the excited state potential energy surface and could potentially decrease the observed lifetime. Population that is transferred from the $\pi 3s$ component of $S_2(\pi 3s/\pi\sigma^*)$ to

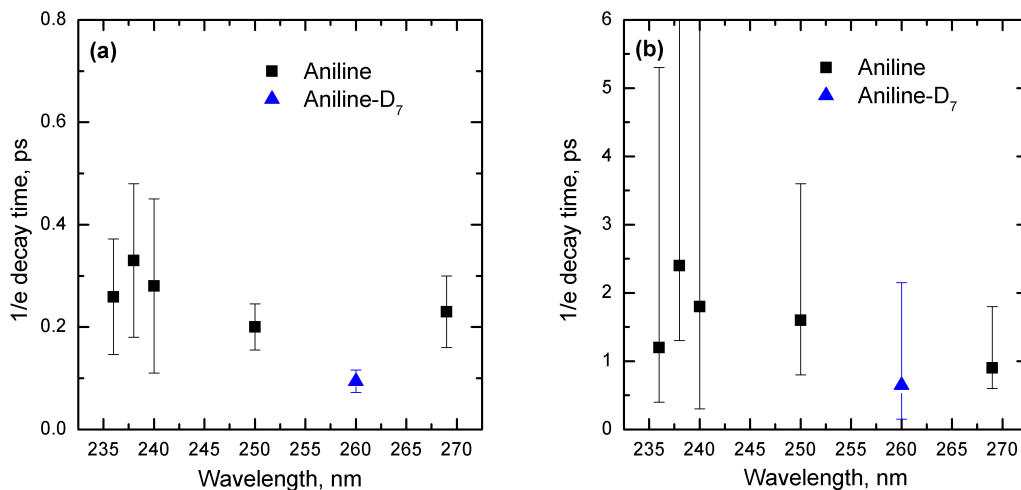


Figure 3.24: 1/e decay times of the (a) $S_2(\pi 3s)$ and (b) $S_2(\pi \sigma^*)$ components of the $S_2(\pi 3s/\pi \sigma^*)$ state for aniline and deuterated aniline.

$S_1(\pi \pi^*)$ subsequently decays relatively slowly, on a timescale that decreases from > 1 ns at the S_2 origin (269 nm), to around 81 ps at 0.65 eV above the S_2 origin (236 nm). The absence of any negative amplitude features in the spectra associated with this decay for 269 and 250 nm excitation (Figures 3.16(a) and (b)), indicates that the population moves directly out of the observation window. Thus, it is most likely that the $S_1(\pi \pi^*)$ population decays back to the electronic ground state S_0 . There is also a possibility of population passing diabatically through the S_2/S_1 conical intersection, at modest N–H bond lengths, to the $\pi \sigma^*$ component of the $S_2(3s/\pi \sigma^*)$ state to form the anilino radical and H atom; this could account for the fast H atoms observed in H-atom photofragmentation translational spectroscopy [103] and femtosecond pump-probe velocity map imaging measurements [119], discussed in section 3.3.4.

The femtosecond pump-probe photoionisation experiments reported by Castaño *et al.* [104] identified a decay with a lifetime of 165 fs which, within experimental error, matches the lifetime we assign to the $\pi 3s$ Rydberg component of $S_2(\pi 3s/\pi \sigma^*)$. They attributed the 165 fs lifetime to dissociation along the $\pi \sigma^*$ component of $S_2(\pi 3s/\pi \sigma^*)$, by reference to H atom photofragmentation studies [103], and to internal conversion to $S_1(\pi \pi^*)$. They determined that dissociation along the $\pi \sigma^*$ potential energy surface was not a significant relaxation pathway, although it is not surprising that the 165 fs decay was a minor component of the total integrated

decay profile, since both the $\pi 3s$ Rydberg component of $S_2(\pi 3s/\pi\sigma^*)$ and $S_1(\pi\pi^*)$ lie within the observation window of the photoionisation experiments. Assuming that the population flows from one state into the another and both states have similar ionisation cross-section, the dynamics of the $\pi 3s$ state will be masked in the integrated signal.

Our experiments have also revealed another non-radiative decay channel that has a 1 – 2 ps lifetime and is characterised by a broad band in the photoelectron spectrum from 0 – 0.6 eV. In principle, from an eKE point of view, this component of the photoelectron spectrum could correspond to photoionisation from $S_1(\pi\pi^*)$, but we believe that it is more likely that it corresponds to photoionisation from $S_2(\pi 3s/\pi\sigma^*)$ for the following reasons. The decay associated spectra for 269, 250 and 236 nm excitation (Figures 3.16(a), (b) and (c)) and fits to the 240 and 238 nm spectra (Figures 3.18(a) and (b)), suggest that the state with the 1–2 ps lifetime is populated directly during the excitation process. A direct excitation of this state is also observed in aniline-D₇ (Figure 3.23(a)) with a similar decay time (Figure 3.24(b)). From the absorption spectrum (Figure 3.9(b)), it seems unlikely that direct population of $S_1(\pi\pi^*)$ above 240 nm would be measurable in our experiments. In addition, the 269 nm decay associated spectra (Figure 3.16(a)) suggest that the spectrum of the directly excited component with a 0.9 ps decay has considerable overlap with the directly excited $S_1(\pi\pi^*)$ spectrum that decays on a timescale greater than 1 ns. It would be difficult to rationalise two decay timescales for $S_1(\pi\pi^*)$ following 269 nm excitation below the barrier along the N–H bond stretch (Fig. 3.6) and one 1–2 ps decay timescale for $S_1(\pi\pi^*)$ following excitation above the barrier. Moreover, like the $\pi 3s$ component of $S_2(\pi 3s/\pi\sigma^*)$, this feature has a decay time that does not vary significantly with excitation energy (Table 3.1). Thus, we believe that the 1–2 ps non-radiative decay channel is most likely to correspond to population across the $\pi 3s$ and $\pi\sigma^*$ components of $S_2(\pi 3s/\pi\sigma^*)$.

The lifetime of the $S_2(\pi 3s/\pi\sigma^*)$ population has a large uncertainty associated with it, which we attribute at least in part to a variation in the time constant across the spectral profile (Figures 3.17 (c) and 3.18(e) and (f)). This would be consistent with a change in the vertical detachment energy along the NH stretch coordinate [136], or possibly with population being trapped in the upper section of a conical intersection, as has been observed in thioanisol [140] and methylamine [141]. It is worth noting that the decay time derived from our fitting procedure is similar to the

timescales attributed to motion on $\pi\sigma^*$ surfaces in indole and 5-hydroxyindole [138]. In indole and 5-hydroxyindole the intermediate state with a lifetime of about 1 ps was attributed to the $\pi\sigma^*$ state which has two possible decay channels either *via* the dissociation of the N–H bond or relaxation back to the ground state. The absence of any negative amplitude features in the spectra associated with this decay following 269 and 250 nm excitation (Figures 3.16(a) and (b)) suggests that the population moves out of the observation window of our experiment, either passing diabatically through the S_2/S_0 conical intersection at extended N–H bond lengths to form the anilino radical and the H atom (which could explain the observation of anisotropic H atom distributions following excitation at wavelengths >260 nm in H atom photofragment translational spectroscopy experiments) [103] or diabatically to form vibrationally hot S_0 .

3.6.2 $S_3(\pi\pi^*)$

Following excitation above the origin of the $S_3 \leftarrow S_0$ transition (240 - 236 nm), our experiments show that direct excitation to the $S_3(\pi\pi^*)$ state is the dominant process, as expected from the absorption spectrum. The $S_3(\pi\pi^*)$ state decays extremely rapidly, on a timescale of around or less than 100 fs. The vibrational structure observed in the $S_3(\pi\pi^*)$ photoelectron spectrum is maintained during the decay; it is likely to correspond to a progression in a totally symmetric mode but does not provide any dynamical information. The significant decrease in the total photoionisation signal within the lifetime of the $S_3(\pi\pi^*)$ state (Figures 3.12(a-c)) suggests that the majority of the $S_3(\pi\pi^*)$ population moves out of the observation window of our experiment, most probably to the ground state through an S_3/S_0 conical intersection.

A rapid (< 100 fs) decay of total photoionisation signal was also observed in femtosecond pump-probe ionisation studies of Castaño *et al.* following excitation at wavelengths < 240 nm [104], but was attributed to internal conversion through an S_3/S_1 conical intersection. H atom loss was observed in photofragment translational spectroscopy studies at similar wavelengths and was proposed to arise from coupling to the $\pi\sigma^*$ component of the $S_2(\pi 3s/\pi\sigma^*)$ potential energy surface through an S_3/S_2 conical intersection or successive S_3/S_1 and S_1/S_2 conical intersections. However, we do not see any convincing evidence of significant population flow into $S_1(\pi\pi^*)$

or $S_2(\pi 3s/\pi\sigma^*)$ on a < 100 fs timescale. It is possible that there is some internal conversion through an S_3/S_1 conical intersection: a very small rise in $S_1(\pi\pi^*)$ population due to $S_3(\pi\pi^*)$ decay would be difficult to disentangle from the significant rise in $S_1(\pi\pi^*)$ population due to decay of the $\pi 3s$ Rydberg component of $S_2(3s/\pi\sigma^*)$. In principle, it is also possible that a small proportion of the population undergoes internal conversion through an S_3/S_2 conical intersection; however, we do not observe any delay in the rise of population in the $S_2(\pi 3s/\pi\sigma^*)$ state, which we believe lies within our observation window. Therefore, we conclude that the dominant decay pathway for $S_3(\pi\pi^*)$ population is rapid (< 100 fs) internal conversion to the electronic ground state through an S_3/S_0 conical intersection.

Theory has predicted that the $S_1 \leftarrow S_0$ transition has charge-resonance character and some charge-transfer character and that the $S_3 \leftarrow S_0$ transition is the result of a local excitation on the benzene ring [106], so we might expect an S_3/S_0 conical intersection to lie along a mode similar to the benzene ‘prefulvene mode’ which is understood to lead to ultrafast S_1/S_0 internal conversion in the ‘channel 3’ region of benzene [130, 131, 132]. Once back on the ground-state surface, there would be two possible mechanisms for fragmentation. One would involve passing adiabatically through the S_0/S_2 conical intersection at extended N–H bond lengths to generate H atoms with high translational energy. The other would be by unimolecular dissociation of vibrationally hot S_0 to generate H atoms with low translational energy. These mechanisms would be consistent with the bimodal distribution observed in H (Rydberg) atom photofragment translational spectroscopy experiments [103].

It is most likely that the vibrational structure observed in the $S_3(\pi\pi^*)$ photoelectron spectrum corresponds to a progression in a totally symmetric vibrations. Based on the vibration frequencies of the aniline cation observed experimentally by ZEKE spectroscopy [117], we suspect that our observed vibrational spacing at 236 nm excitation (604 cm^{-1}) is most likely to correspond to a progression in the ν_{6a} mode (quinoid ring deformation in the plane of the benzene ring). The vibrational spacing observed at 240 nm excitation (1200 cm^{-1}) corresponds most likely to the ν_{9a} mode (ring stretch and CH scissor motion in plane of the benzene ring). These observations suggest that there is a change in geometry along the 6a and 9a coordinate between the S_3 and D_0 states, but does not provide any dynamical information.

3.7 Conclusion

Our time-resolved photoelectron spectroscopy study of aniline, following absorption of ultraviolet light in the range 269–236 nm, has provided detailed information about the intermediate electronic states involved in the electronic relaxation of this biologically important chromophore, supporting some conclusions reached following H atom photofragment translational spectroscopy measurements and pump-probe photoionisation measurements, and contradicting some others.

Our results confirm that aniline possesses a low-lying electronic state with significant Rydberg character in the Franck-Condon region and reveal that this state is populated directly over a wide range of excitation wavelengths (269–236 nm). Our experiments and analysis have allowed us to visualise much of the relaxation process and our proposed scheme is summarised in Figure 3.25. Our analysis of the photoelectron spectra suggests that the directly excited $S_2(\pi 3s/\pi\sigma^*)$ population bifurcates to two non-radiative decay channels. Interestingly, the decay times of both $S_2(\pi 3s/\pi\sigma^*)$ paths are independent of excitation energy. One channel involves relaxation back to the electronic ground state by rapid internal conversion (200–300 fs) through an S_2/S_1 conical intersection that must be located close to the Franck-Condon region, followed by much slower internal conversion (81 ps – ns) to S_0 . Our results on deuterated aniline suggest that there is no significant dissociation in aniline directly from the $\pi 3s$ state. It is possible that population also passes diabatically through the S_2/S_1 conical intersection to form the anilino radical and H atom, which would be consistent with other experimental observations of fast H atoms [103, 119], including the timescale of 155 fs and 170 fs observed by Stavros *et al.* at 240 and 200 nm, respectively. The other channel involves motion on the $S_2(\pi 3s/\pi\sigma^*)$ potential energy surface with a decay time of 1–2 ps, most likely towards the S_2/S_0 conical intersection at extended N–H bond lengths, where it can either dissociate or return to the electronic ground state.

Close to the S_2-S_0 origin (269 nm excitation), both $S_2(\pi 3s/\pi\sigma^*)$ and $S_1(\pi\pi^*)$ are populated during the excitation process. At higher excitation energies, between the absorption maxima of $S_1(\pi\pi^*)$ and $S_3(\pi\pi^*)$ (250 nm excitation), only $S_2(\pi 3s/\pi\sigma^*)$ is populated during the excitation process. Increasing the excitation energy further to just below the absorption maximum of $S_3(\pi\pi^*)$ (240, 238 and 236 nm excitation) results in significant population of the $S_3(\pi\pi^*)$ state. Somewhat surprisingly, the

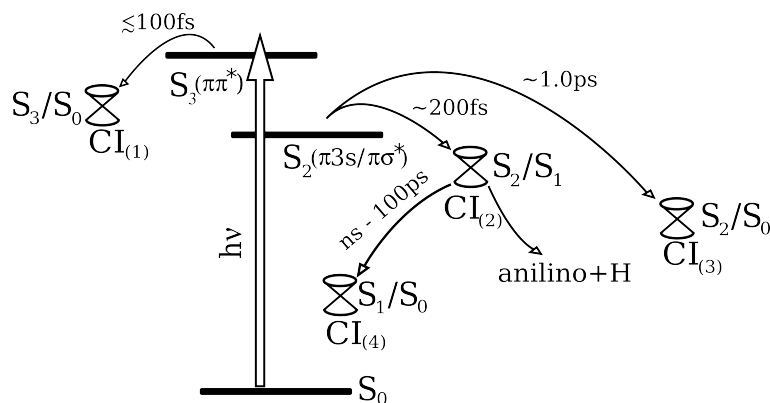


Figure 3.25: Schematic diagram summarising the non-radiative decay pathways determined from our experimental observations and analysis.

dominant relaxation pathway is an extremely rapid ($\lesssim 100$ fs) internal conversion back to the electronic ground state, most likely through an S_3/S_0 conical intersection.

The observation of these competing non-radiative relaxation channels in aniline illustrates that its photostability arises from a subtle balance between dynamics on different potential energy surfaces and between Rydberg and valence states. As well as providing the motivation to reinvestigate the electronic relaxation of other chromophores possessing excited electronic states with mixed Rydberg-valence character, this study highlights the need for time-resolved photoelectron spectroscopy with higher energy probe pulses to monitor both the formation of the products of dissociation and the return of population to the electronic ground state.

UV pump – VUV probe femtosecond TRPES experiments of aniline have been attempted by our group in collaboration with other universities using Rutherford Appleton Laboratory (RAL) and Imperial College London VUV sources. VUV femtosecond pulses were obtained *via* high harmonic generation (HHG) in argon from an 800 nm fundamental wavelength in both experiments. High energy VUV photons (around 20 eV at RAL and 35 eV at Imperial College) carry sufficient energy to ionise an aniline molecule from the ground electronic state by absorption of a single photon. Since only a small fraction of the molecules are excited in pump-probe experiments, the majority of the molecules in the interaction region remain in their ground electronic state. Assuming that the photoionisation cross-section is similar for all electronic states, most of the photoelectron signal in UV-VUV pump-probe experiments originates from the ground electronic state and only a small fraction of the photoelectrons are ionised from the excited states or reaction products. There-

fore the signal to noise ratio must be extremely high in such experiments in order to detect any excited state dynamics.

Reasonable progress has been made at RAL towards UV-VUV pump-probe experiments where we were able to detect the UV-VUV pump-probe signal using one of the He resonances. However, we could not detect any UV-VUV pump-probe signal from aniline due to the low signal to noise ratio. Increasing the density of aniline molecules in the interaction region would improve the sensitivity of the experiment to the aniline excited state dynamics.

The use of 35 eV photons during the experiments at Imperial College caused additional difficulties. Such high energy photons were able to ionise the ground state of the carrier gas *via* a single photon ionisation process. This process produced additional background signal and complicated the experiment.

High-level quantum molecular dynamics calculations using accurate potential energy surfaces and calculations of the time-resolved photoelectron spectra are also highly desirable, in order to better characterise the molecular system. Such theoretical studies are currently in progress in collaboration with Dr Graham Worth (University of Birmingham, UK) and Matthieu Sala (Universite Montpellier II, France).

Chapter 4

Ultrafast non-adiabatic dynamics in DABCO

Femtosecond gas phase non-adiabatic dynamics in 1,4-diazabicyclo[2.2.2]octane (DABCO) have been investigated using time-resolved photoelectron imaging apparatus. DABCO is excited over a wide range of wavelength in the ultraviolet spectrum between 251 and 233 nm. The $S_2 3p_{x,y}(+)$ state is predominantly directly populated at all wavelengths with a subsequent relaxation to the $S_1 3s(+)$ state. Also a small amount of the directly excited $S_1 3s(+)$ state is observed at 251 nm excitation wavelength. $S_1 3s(+)\leftarrow S_2 3p_{x,y}(+)$ internal conversion was found to be the only relaxation pathway of the photoexcited $S_2 3p_{x,y}(+)$ state. The $S_2 3p_{x,y}(+)$ decay dynamics is best described by a biexponential time dependence. Angular resolved measurements revealed that the excitation process is dependent on the molecular alignment.

A detailed overview of the spectroscopy, structure and dynamics of the low-lying Rydberg states of DABCO is given at the beginning of this chapter. In sections 4.3 and 4.4, time-resolved photoelectron imaging experimental results of $S_1 3s(+)\leftarrow S_2 3p_{x,y}(+)$ internal conversion in DABCO are presented and discussed.

4.1 Introduction

1,4-diazabicyclo[2.2.2]octane ($C_6H_{12}N_2$), DABCO, has been intensively studied in part due to its highly symmetric structure – it has a rigid cage-like structure and D_{3h} symmetry [142] (Figure 4.1). All of the singlet electronically excited states of DABCO have predominantly Rydberg character and a small amount of valance character [143]. The high symmetry and the low-lying Rydberg states have generated significant interest in the DABCO molecule.

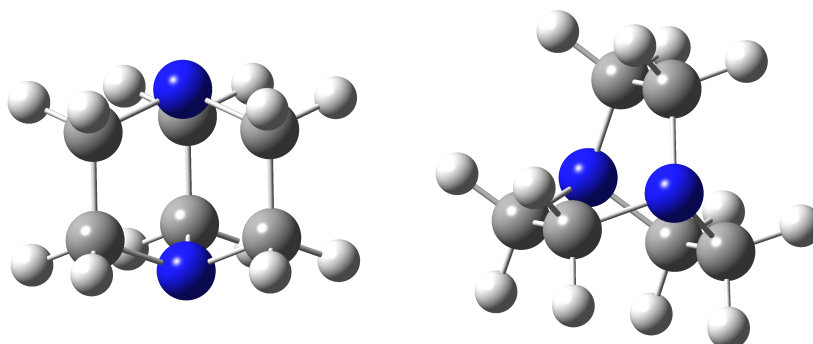


Figure 4.1: DABCO molecule in the ground electronic state. Two nitrogen atoms (blue) are situated at the top and bottom of the cage structure with six carbon atoms (grey) forming the cage.

4.2 Spectroscopy, structure and dynamics

4.2.1 Spectroscopy of DABCO

The gas phase absorption spectrum of DABCO has been studied in detail by A.M. Halpern *et al.* [144] (see Figure 4.2). The first strong absorption band corresponds to a single photon excitation of the second electronically excited singlet state $S_2 \leftarrow S_0$. The S_2 state possesses $3p_{x,y}(+)$ Rydberg character and has ${}^1E'_1$ symmetry. The location of its origin was measured at 4.94 eV ($39\,830\text{ cm}^{-1}$) above the ground state [144]. The second strong absorption band starts at about $49\,000\text{ cm}^{-1}$ and grows in intensity towards the ionisation limit which occurs at $58\,033\text{ cm}^{-1}$. This band was assigned to the $4p \leftarrow S_0$ transition where the $4p$ state has ${}^1E'$ symmetry [145]. The 0–0 transition of this single photon absorption band is located at

6.12 eV (49 380 cm^{-1}) [144]. The precise value of the adiabatic ionisation potential energy of 58 033 cm^{-1} (7.2 eV) was measured by ZEKE spectroscopy [146].

The first electronically excited singlet state, S_1 , has ${}^1A_1'$ symmetry, the same as the ground state [147]. Therefore, a single photon $S_1 \leftarrow S_0$ transition is forbidden in a molecule with D_{3h} symmetry and, hence, this transition does not appear in the absorption spectrum. The S_1 state has mostly 3s(+) Rydberg character and its origin lies 4.44 eV (35 790 cm^{-1}) above the ground state, which was measured using multiphoton ionisation spectroscopy [148]. The location of the third electronically excited singlet state ${}^1A_2''$ 3s(-) has been under discussion for some time [54, 145, 149, 150], however, it has never been detected. Its energetic location was calculated to be very close to the S_2 3p_{x,y}(+) state, however, its computed oscillator strength is much smaller than that of the S_2 3p_{x,y}(+) state [145, 147].



Figure 4.2: A gas-phase UV absorption spectrum of DABCO reproduced from reference [144].

Light emission studies of DABCO vapour [151] suggested that fluorescence is the main emission relaxation pathway in DABCO, which indicates that there is no efficient intersystem crossing in this molecule. A fluorescence lifetime of about 1 μs and a quantum yield of 0.9 were measured after photoexcitation of the molecule with 250.7 nm light.

A DABCO molecule in the D_{3h} symmetry group has 36 non-degenerate vibrational modes. Experimental and theoretical studies of the vibrational modes of the

DABCO molecule are summarised in a theoretical paper by Balakrishnan *et al.* [152]. The summary includes vibrational frequencies for the ground state of the neutral molecule and its cation and first two electronically excited singlet states. The theoretical calculations agree well with the experimental data obtained from the laser induced fluorescence (LIF) measurements [153] and Raman and IR spectroscopy measurements [154, 155, 156]. The lowest vibrational wavenumber of 58 cm^{-1} [157] corresponds to the torsional mode (a_1'') [152]. This low frequency mode can be thermally populated at room temperature ($T \sim 300\text{ K}$): $kT \sim 200\text{ cm}^{-1}$. It was shown that, by thermally populating the torsional levels, the D_{3h} symmetry of DABCO is broken and a single photon excitation $S_1 \leftarrow S_0$ becomes allowed [143].

A high resolution absorption spectrum of DABCO vapour [144] shows that the most intense $S_2\ 3p_{x,y}(+) \leftarrow S_0$ vibronic transitions correspond to excitation of the vibrational progressions of four vibrational modes in the $S_2\ 3p_{x,y}(+)$ state. These vibrational modes have been assigned to four totally symmetric a_1' modes: ν_3 (1293 cm^{-1}), ν_4 (875 cm^{-1}), ν_5 (788 cm^{-1}) and ν_6 (685 cm^{-1}). The wavenumbers of these modes were obtained from multiphoton ionisation measurements [148].

Using two-colour fluorescence dip spectroscopy the Jahn-Teller splitting of the vibronic states was observed for low lying electronic states in DABCO [158]. It was found that the splitting decreases with increasing principal quantum number n and disappears for $n > 6$. Due to this regularity the authors concluded that the Jahn-Teller splitting occurs due to the interaction between the Rydberg electron and the ion core. An energy splitting of 50 cm^{-1} was measured for the $5p$ state and $50\text{--}300\text{ cm}^{-1}$ for the $4p$ state.

4.2.2 Structure of DABCO

The DABCO molecule has a rigid cage-like structure (see Figure 4.1). The ground electronic state, S_0 , has a quasi- D_{3h} symmetry which is distorted from the D_{3h} symmetry by a small twist of about 10° around the C_3 axis [54, 142]. Therefore the S_0 potential energy surface has a double minimum, however, the barrier between the two minima is very small. The barrier height was determined from theoretical calculations to be only 20 cm^{-1} [54] which is in good agreement with 30 cm^{-1} obtained from electron diffraction experiments [142]. The minimum of the first excited singlet state, $S_1\ 3s(+)$, has a distortion over two angles leading to C_3 point

group symmetry [54]. The Jahn-Teller distortion reduces the S_2 $3p_{x,y}(+)$ symmetry to the C_{2v} point group. Due to the rigid structure of the molecule its geometry does not change dramatically between the different electronically excited states. Overall the length of the C–C bond increases with the higher excited state and the N–C bond shortens [54, 152].

4.2.3 Internal conversion in DABCO

Smith et al. [149] have employed two-colour photoionisation spectroscopy to study excited state dynamics in jet cooled DABCO. While exciting the origin of the S_2 $3p_{x,y}(+)$ with two photons and scanning the ionisation wavelength, they observed three distinct thresholds. The first high energy threshold corresponds to the adiabatic ionisation potential of DABCO and was determined to be $58\,052\text{ cm}^{-1}$ (7.1973 eV), which is in a good agreement with ZEKE spectroscopy measurements [146]. The second and third thresholds were attributed to the S_1 $3s(+)$ and the $3s(-)$ states, which have been populated through the internal conversion from the S_2 $3p_{x,y}(+)$ state. The origin of the $3s(-)$ obtained from these measurements is located $37\,500\text{ cm}^{-1}$ above the ground state, which does not agree with the previous theoretical calculations [147, 145]. However, later revision of this data by Pratt [150] suggested that the feature attributed to the $3s(-)$ state corresponds to the vibrationally autoionising Rydberg states accessed from vibrationally excited levels of the S_1 $3s(+)$ state and converging to vibrationally excited levels of the ground state ion. In this interpretation, the $3s(-)$ state remains unobserved.

In recent work, A. Stolow’s group [54] used TRPES to observe a non-adiabatic S_1 $3s(+)$ \leftarrow S_2 $3p_{x,y}(+)$ population transfer. They monitored evolution of the photoelectron spectrum after photo-excitation of DABCO to the S_2 $3p_{x,y}(+)$ origin with a 251.1 nm laser pulse and ionised it using a 267 nm laser pulse. From the observed photoelectron yields they concluded that only the S_1 $3s(+)$ and S_2 $3p_{x,y}(+)$ states are involved in the dynamics, and that these states have the same photoionisation cross-section. The decay of the S_2 $3p_{x,y}(+)$ state was best fit with a biexponential function, which was attributed to the non-exponential kinetics. In addition, they observed 11 cm^{-1} photoelectron intensity modulation of the S_1 $3s(+)$ and S_2 $3p_{x,y}(+)$ decay components. Their theoretical model predicted a three level structure formed due to the Jahn-Teller interaction which lifts the degeneracy of the S_2 $3p_{x,y}(+)$

state and non-adiabatic coupling between the S_1 $3s(+)$ and S_2 $3p_{x,y}(+)$ states. This would result in three modulation frequencies equal to the energy spacing between the electronic states. While two energy spacings would produce a high frequency modulation (~ 200 cm^{-1}), which can not be resolved in their experiment, the third energy spacing would produce a modulation of about 11 cm^{-1} , which matches the experimental observations. Their studies also revealed that, by reducing the cooling of the molecular beam, the contrast of the electronic revivals is reduced due to the incoherent sum of the initial wavepackets.

4.3 TRPEI investigation of DABCO following 251 – 234 nm excitation

4.3.1 Experimental method

Time-resolved photoelectron imaging (TRPEI) has been used to study non-adiabatic dynamics of photoexcited DABCO. DABCO molecules were promoted into the second electronically excited singlet state, S_2 $3p_{x,y}(+)$, as shown in Figure 4.3, *via* a single photon absorption process in a wide range of photoexcitation wavelengths 233.9 nm – 251.2 nm (4.9 eV – 5.3 eV). The dynamics were observed by detecting the photoelectron energy and angular distributions after photoionisation with 400 nm or 800 nm wavelength. Both the pump and the probe laser pulses were linearly polarised, parallel both to each other and to the detector plane. The schematic energy level diagram together with the excitation scheme are shown in Figure 4.3.

A detailed description of the setup is provided in section 2.5 in chapter 2. During the experiments, the detector chamber pressure was maintained below 10^{-7} Torr, ensuring collisionless conditions. The pump and probe pulse energies were reduced to < 100 nJ using polarisers and half-wave plates, to produce less than one photoelectron per laser shot due to the photoelectron detector limitations.

For each excitation wavelength, three data sets were obtained by collecting photoelectron images with 2×10^4 , 0.25×10^6 and 2×10^6 laser shots. Images were recorded as a function of pump-probe time delay for each data set. The pBasex inversion algorithm was used to reconstruct a three dimensional velocity distribution for all images [96]. Photoelectron angular distributions were obtained as a result of

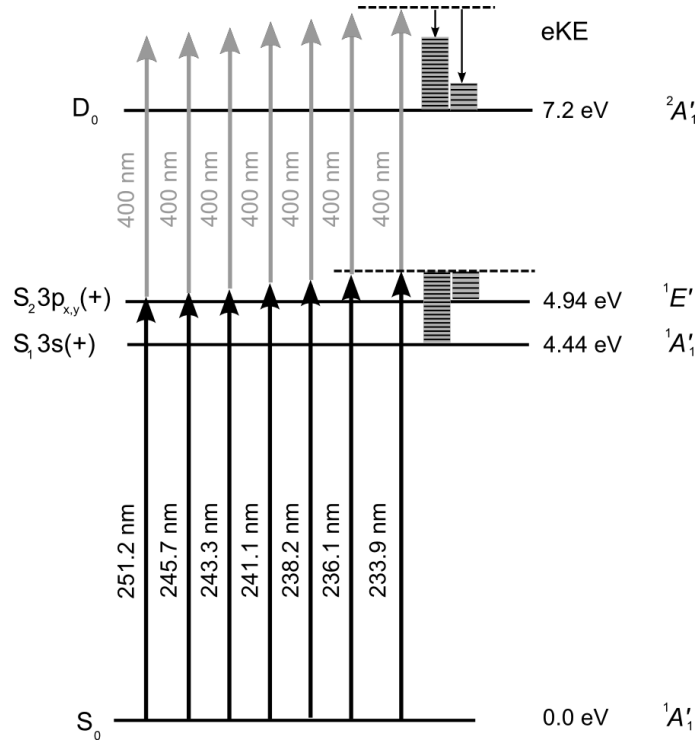


Figure 4.3: Excitation scheme: DABCO is excited using seven different wavelengths in the range from 233.9 nm to 251.2 nm. The excited state population is projected onto the ionisation continuum using a delayed 400 nm laser pulse. Assuming conservation of the vibrational energy during photoionisation, the electron kinetic energy (eKE), following ionisation out of the Franck-Condon region, is expected to increase in the order $S_1 < S_2$. The vibrational energies (blocks of horizontal lines) and corresponding eKEs (downward vertical arrows) are illustrated for 233.9 nm excitation.

the pBasex inversion, with the following expression for the angular basis set:

$$I(\theta) = a[1 + \beta_2 P_2(\cos \theta) + \beta_4 P_4(\cos \theta)], \quad (4.1)$$

where $I(\theta)$ is the probability of photoelectron emission at a particular angle θ , defined as the angle between the laser polarisation and the velocity vector of the photoelectron, $P_n(\cos \theta)$ are the n^{th} order Legendre Polynomials, β_n are the anisotropy parameters and a is a normalisation constant. An example of the photoelectron image obtained with single photon pump (251.2 nm) and single photon probe (400 nm) laser pulses is shown in Figure 4.4.

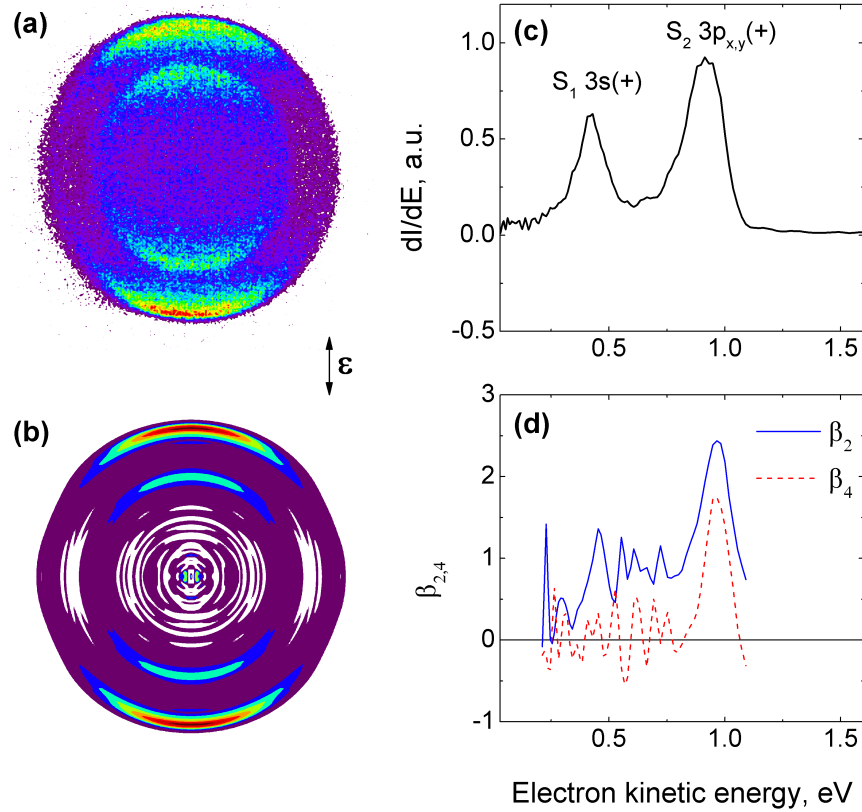


Figure 4.4: (a) Original velocity map image, (b) inverted velocity map image, (c) photoelectron spectra and (d) anisotropy parameters recovered from the inverted image. The image was recorded with a 251.2 nm pump pulse, a 400 nm probe pulse and a pump-probe delay of 150 fs.

4.3.2 Time-resolved photoelectron spectra

The DABCO spectrum has two distinct photoelectron bands centred at 0.9 eV and 0.4 eV photoelectron kinetic energies (Figure 4.4). In the first approximation, we can assign the origin of the photoelectron bands under the assumption that the vibrational energy is preserved during photoionisation:

$$\text{eKE} = h\nu_{\text{probe}} - [E(D_n) - E(S_n)], \quad (4.2)$$

where eKE is electron kinetic energy, $h\nu_{\text{probe}}$ is the energy of the ionising photon, $E(S_n)$ is the energy of the electronic state, S_n , above the ground state, and $E(D_n)$ is the ionisation potential of the molecule which has been determined to be 7.2 eV [146]. Using known energy values for the S_1 3s(+) and S_2 3p_{x,y}(+) states of 4.44 eV [148] and 4.94 eV [144], respectively, we can assign the low energy photoelectron peak

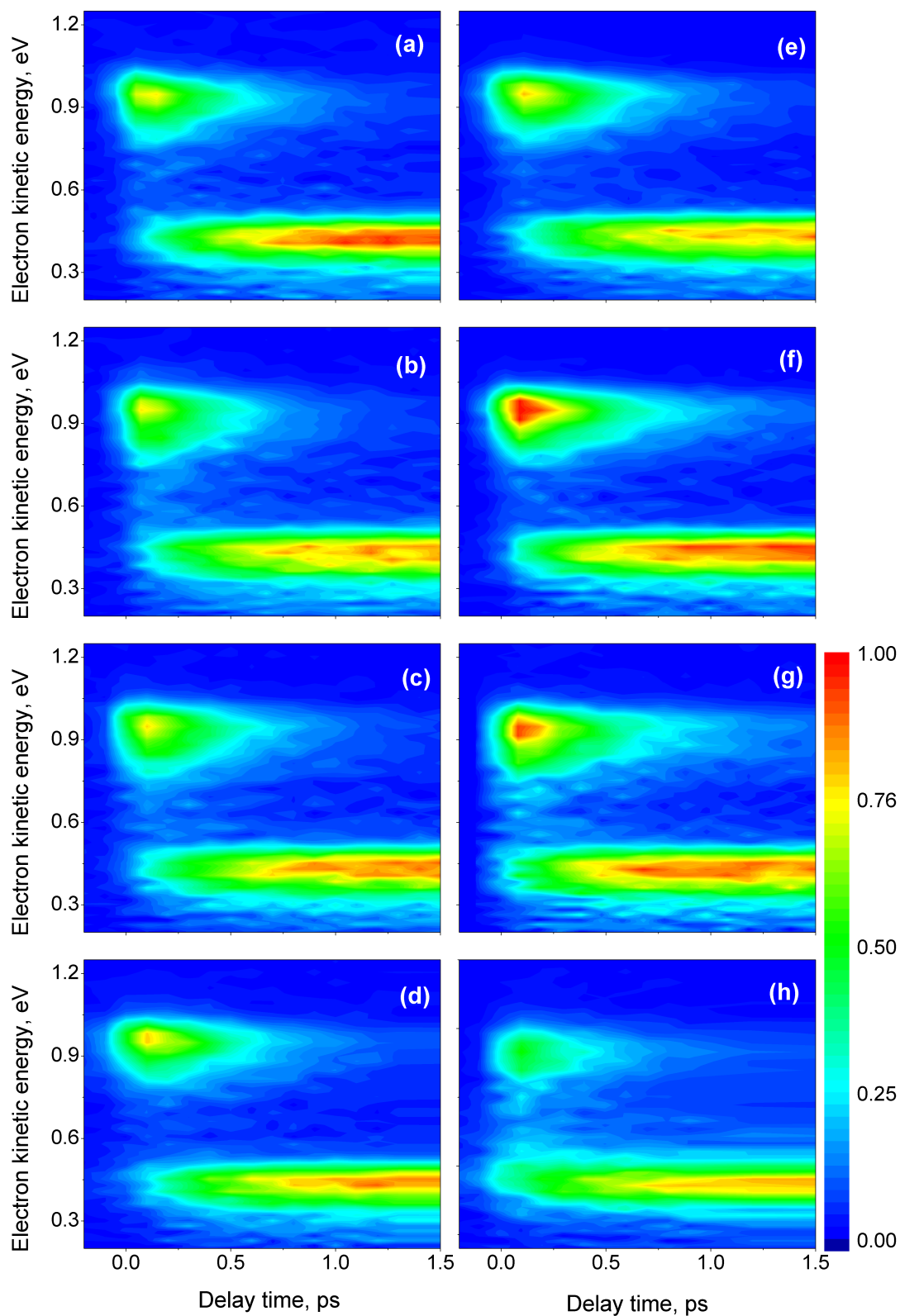


Figure 4.5: Time resolved photoelectron spectra of DABCO at (a) 233.9 nm, (b) 236.1 nm, (c) 238.2 nm, (d) 241.1 nm, (e) 243.3 nm, (f) 245.7 nm, (g) 251.2 nm pump wavelengths and 400 nm probe and (h) 251.2 nm pump and 800 nm probe wavelengths.

to correspond to ionisation from the S_1 $3s(+)$ electronic state and the high energy photoelectron peak to correspond to photoionisation from the S_2 $3p_{x,y}(+)$ electronic state.

The photoelectron peaks are reasonably sharp with FWHMs of about 0.14 eV and 0.2 eV for the S_1 $3s(+)$ and S_2 $3p_{x,y}(+)$ states, respectively. They also have highly anisotropic angular distributions. These facts are consistent with photoionisation from the electronic states with mainly Rydberg character. All photoelectron spectra possess non-zero values of β_2 and β_4 across the high and low energy photoelectron peaks. The presence of β_4 in the photoelectron angular distribution following single photon ionisation of the excited state indicates that molecules in the excited state were aligned at the instant of ionisation [39]. This is discussed in more detail in section 4.4.

The photoelectron kinetic energy spectra are plotted in Figure 4.5 as a function of the pump-probe delay time for different photoexcitation wavelengths. All the time-resolved photoelectron spectra exhibit similar features: a sharp rise of the S_2 $3p_{x,y}(+)$ component with a subsequent decay on the order of several hundreds of femtoseconds and consequent rise in the S_1 $3s(+)$ component approximately matching the decay of the S_2 $3p_{x,y}(+)$ component. The S_1 $3s(+)$ component does not decay on the time scale of our experiment, as its fluorescence lifetime is about 1 μ s [151].

4.3.3 Timescales

To quantify the dynamics, we fit our experimental photoelectron spectra to a sum of exponentially decaying spectral profiles convoluted with a Gaussian cross-correlation of the pump and probe laser pulses $g(t)$,

$$S(\text{eKE}, t) = \sum_i c_i(\text{eKE}) e^{-t/\tau_i} \otimes g(t), \quad (4.3)$$

where $c_i(\text{eKE})$ is the intensity of the i th decay at a given eKE and τ_i is its corresponding $1/e$ decay time.

The S_2 $3p_{x,y}(+)$ component can be easily separated in the photoelectron spectra. Thus, it is possible to simplify the procedure of finding timescales by fitting discernible portion of the photoelectron spectra, rather than fitting all the parameters simultaneously. An integration over a certain energy range (E_1 to E_2) simplifies equation (4.3):

Table 4.1: Summary of 1/e decay lifetimes extracted from the fitting procedures described in the text.

| Pump wavelength (nm) | Probe wavelength (nm) | S ₂ (fast) lifetime (fs) | S ₂ (slow) lifetime (fs) | FWHM Cross-correlation (fs) |
|----------------------|-----------------------|-------------------------------------|-------------------------------------|-----------------------------|
| 233.91 | 400 | 337 ± 43 | 947 ± 421 | 144 ± 6 |
| 236.1 | 400 | 348 ± 22 | 1389 ± 369 | 133 ± 6 |
| 238.24 | 400 | 358 ± 37 | 1106 ± 410 | 159 ± 5 |
| 241.1 | 400 | 352 ± 22 | 1079 ± 778 | 239 ± 8 |
| 243.3 | 400 | 359 ± 22 | 1749 ± 393 | 215 ± 6 |
| 245.7 | 400 | 314 ± 39 | 1199 ± 260 | 161 ± 5 |
| 251.2 | 400 | 383 ± 20 | 2768 ± 660 | 123 ± 8 |
| 251.2 | 800 | 304 ± 31 | 1945 ± 455 | 133 ± 9 |

$$S(t) = \sum_i c_i e^{-t/\tau_i} \otimes g(t), \quad (4.4)$$

where τ_i is the i th 1/e decay time and $c_i = \int_{E_1}^{E_2} c_i(\text{eKE}) d(\text{eKE})$ is its corresponding intensity, which is proportional to the product of the excited state population and the photoionisation cross-section. A more detailed description of the general data analysis procedure is provided in chapter 2.7. The lifetime of the S₂ 3p_{*x,y*}(+) state has

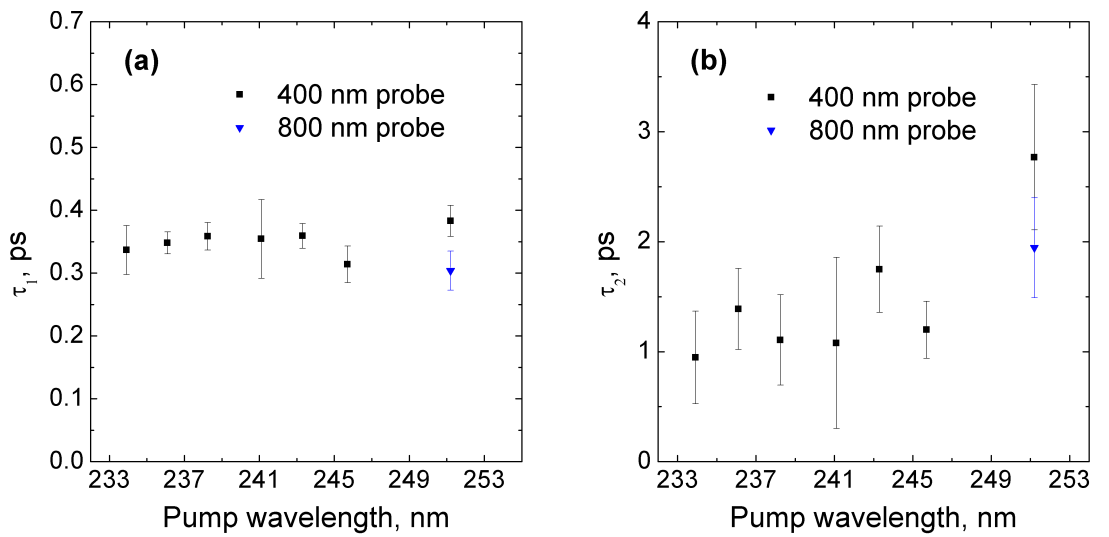


Figure 4.6: Summary of 1/e decay lifetimes of the electronically excited states, listed in Table 4.1. (a) the fast and (b) the slow 1/e decay times.

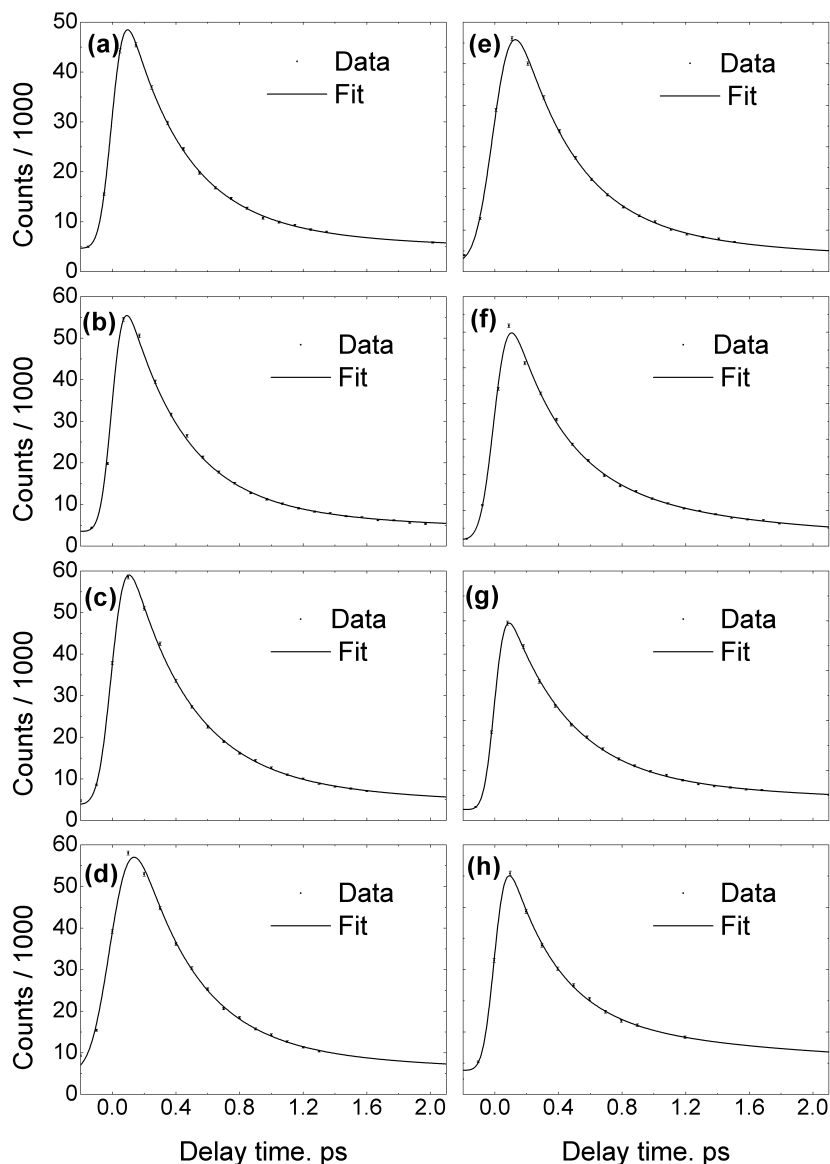


Figure 4.7: Integrated photoelectron counts of the S_2 $3p_{x,y}(+)$ component (0.7 eV to 1.2 eV) as a function of pump-probe delay time at (a) 233.9 nm, (b) 236.1 nm, (c) 238.2 nm, (d) 241.1 nm, (e) 243.3 nm, (f) 245.7 nm, (g) 251.2 nm pump wavelengths and 400 nm probe and (h) 251.2 nm pump and 800 nm probe wavelengths.

been determined by fitting the photoelectron signal integrated over 0.70 eV–1.2 eV to equation (4.4). Two exponential decay components were required to obtain good agreement between the data and the fit for all excitation wavelengths. Integrated photoelectron counts and fits of the S_2 $3p_{x,y}(+)$ component of the photoelectron spectra are shown in Figure 4.7. The $1/e$ decay times obtained from the fit to equation (4.4) are summarised in Table 4.1 and plotted in Figure 4.6. Both decay times

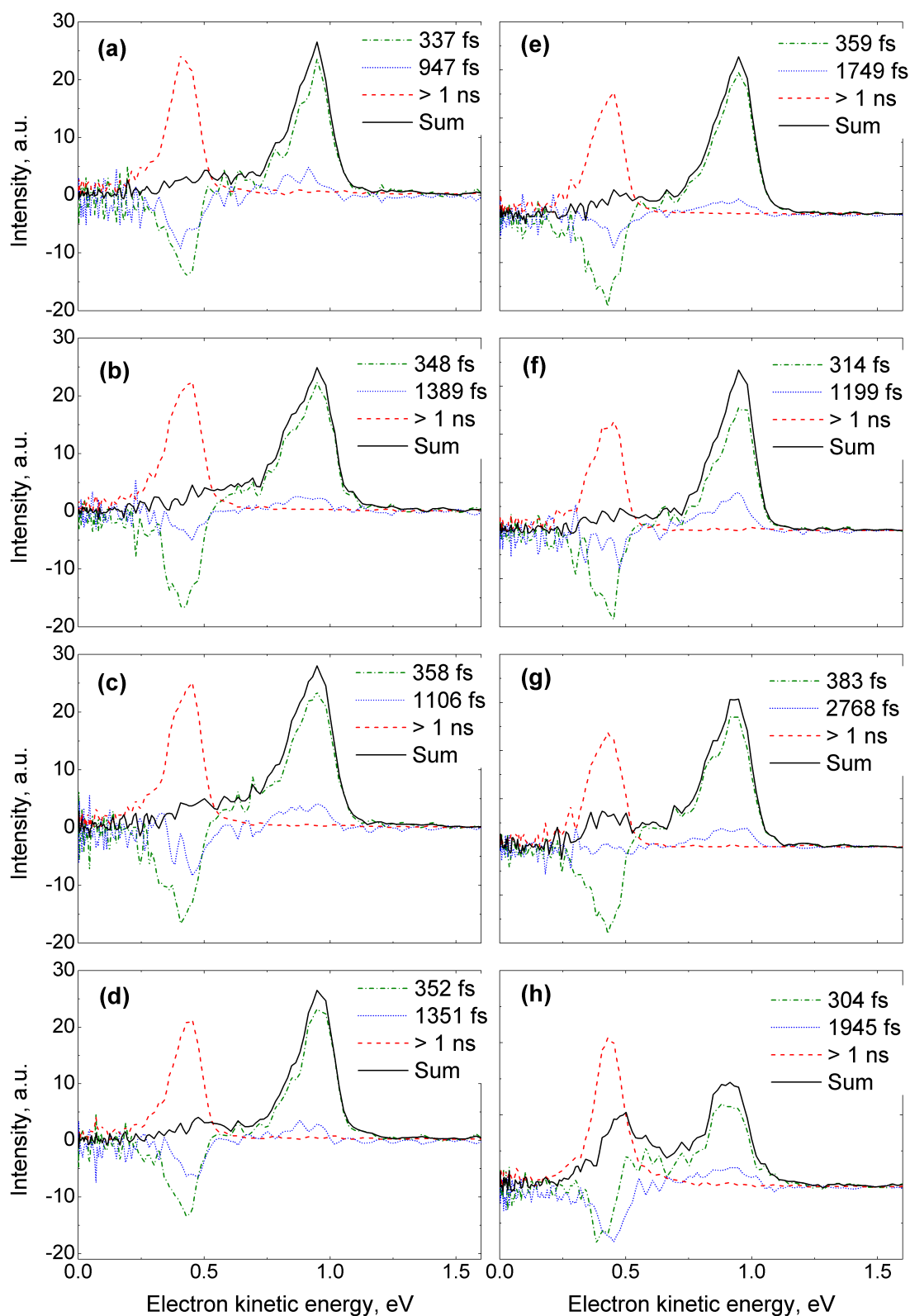


Figure 4.8: Spectral components of the two decay times derived using the fitting procedure described in the text for (a) 233.9 nm, (b) 236.1 nm, (c) 238.2 nm, (d) 241.1 nm, (e) 243.3 nm, (f) 245.7 nm, (g) 251.2 nm pump wavelengths and 400 nm probe and (h) 251.2 nm pump and 800 nm probe wavelengths.

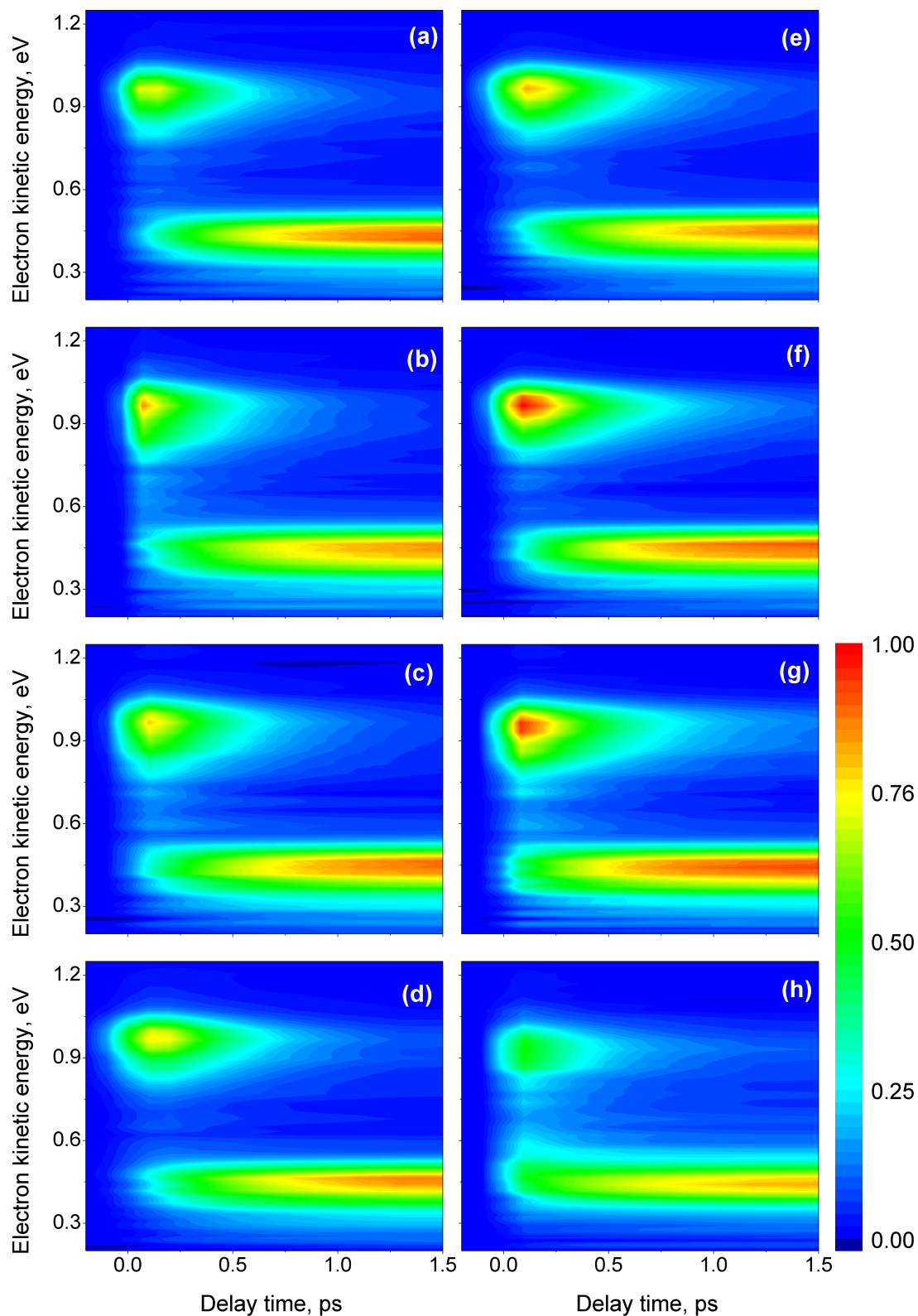


Figure 4.9: Modelled photoelectron spectra for (a) 233.9 nm, (b) 236.1 nm, (c) 238.2 nm, (d) 241.1 nm, (e) 243.3 nm, (f) 245.7 nm, (g) 251.2 nm pump wavelengths and 400 nm probe and (h) 251.2 nm pump and 800 nm probe wavelengths.

do not vary significantly with respect to the excitation wavelength. The rise of the S_1 3s(+) state can be reproduced using the decay components of the S_2 3p_{x,y}(+) state.

Using the lifetimes summarised in Table 4.1, the time resolved photoelectron spectra were fitted to equation (4.3) across the entire energy range. As a result, the decay associated spectra, $c_i(\text{eKE})$, for every decay component, i , were obtained. The positive values of $c_i(\text{eKE})$ correspond to exponential decay; negative values of $c_i(\text{eKE})$ correspond to exponential growth. As discussed in section 3.4.4 of chapter 3, this representation is a valuable method for unravelling relaxation mechanisms from time-resolved photoelectron spectra as long as exponential kinetics are valid.

The decay associated components obtained from the fits to the experimental data are shown in Figure 4.8. Two decay times were required to fit the entire energy range. Both decay times have positive amplitude in the S_2 3p_{x,y}(+) component region and negative amplitude in the S_1 3s(+) component region of the photoelectron kinetic energies. This result unambiguously shows that directly populated S_2 3p_{x,y}(+) state decays into the S_1 3s(+) state. The majority of the S_2 3p_{x,y}(+) population decays on the fast timescale of around 350 fs, however, there is a small contribution (about 10%) of the slow component with a timescale of about 1.5 ps. The solid black lines in Figure 4.8 are the sum over all decay amplitudes and show the directly excited part of the spectrum. A small amount of the S_1 3s(+) is seen to be directly excited at every wavelength.

The photoelectron spectra shown in Figure 4.9 are reconstructed using the obtained timescales and decay associated components and they reproduce the experimental data shown in Figure 4.5 well.

4.3.4 Photoelectron anisotropy

The photoelectron angular distribution can be characterised in terms of anisotropy parameters, β_i , described in equation (4.1). The anisotropy of the photoelectron distribution from a particular peak was calculated as a weighted average across the entire peak in the photoelectron image as explained in the original pBasex paper [96]. Only images with the highest statistics (2×10^6 laser shots) were used to calculate the anisotropy of each state at different time delays. Figure 4.10 shows the evolution of the β parameters with the pump-probe delay time. The second and fourth order

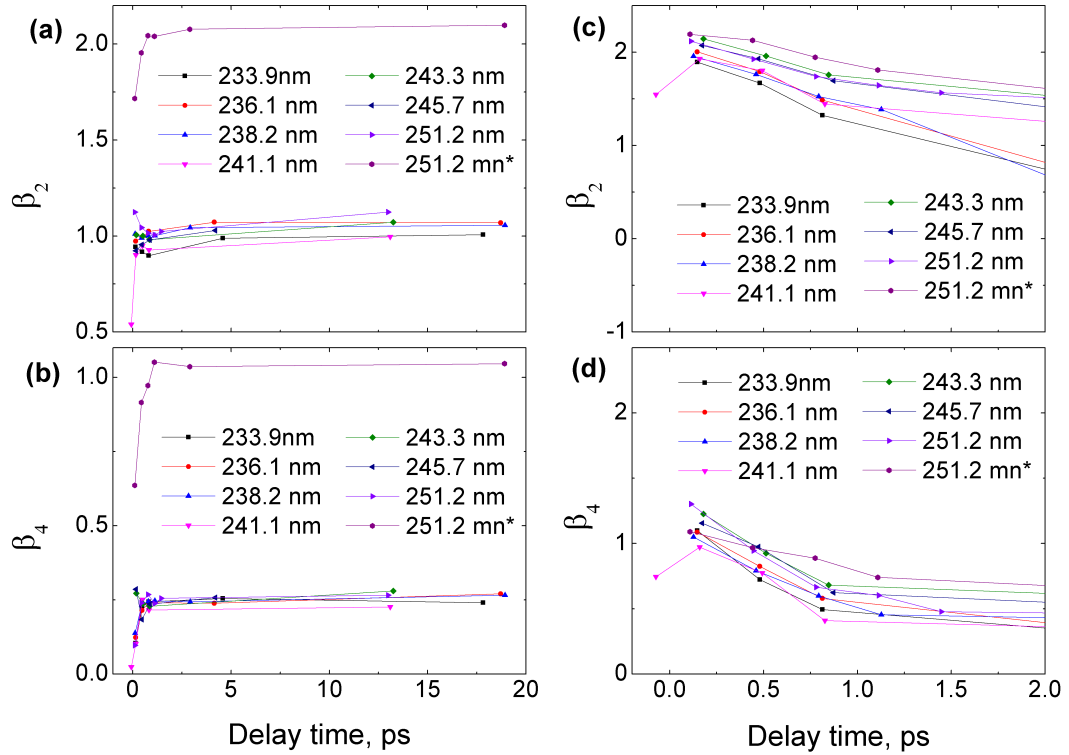


Figure 4.10: Time dependent anisotropy parameters described by equation (4.1) and obtained from the pBasex deconvolution [96]. (a) and (b) anisotropy parameters of the S_1 $3s(+)$ component of the photoelectron spectra and (c) and (d) anisotropy parameters of the S_2 $3p_{x,y}(+)$ component of the photoelectron spectra. *An 800 nm probe wavelength was used for this data set instead of the usual 400 nm probe.

anisotropy coefficients clearly appear in the fit at all delay times. The absolute value of the anisotropy depends on the probe wavelengths and its dependence on the delay time is very similar for all excitation wavelengths. The anisotropy of the S_1 state remains constant over the entire studied time range (0 – 20 ps), while the anisotropy of the S_2 shows a decay over the S_2 lifetime.

4.4 Discussion

4.4.1 S_2 $3p_{x,y}(+)$

Our experiments show that the S_2 $3p_{x,y}(+)$ state is directly populated over the entire range of studied excitation wavelengths (251 nm to 234 nm). The Rydberg nature of the state suppresses any ionisation processes with $\delta v \neq 0$, thus, a photoionisation from the S_2 $3p_{x,y}(+)$ state produces a narrow energy photoelectron peak. The

decay of the S_2 state is best described with a biexponential function. The need for two exponentials agrees with the work of Albert Stolow's group [54]. They concluded that two decay constants are required due to a non-exponential kinetic process. This conclusion is supported by the fact that both decay components have the same spectral shape (see Figure 4.8) and, thus, belong to the same electronic state. On the other hand, the Jahn-Teller interaction lifts the degeneracy of the S_2 $3p_{x,y}(+)$ state providing different diabatic potential energy curves for the orthogonal components of e' double degenerate modes [54]. The orthogonal components could potentially have different decay times but have a sufficiently small energy gap to be indistinguishable in the photoelectron spectrum with a broadband femtosecond laser pulse (approximately 200 cm^{-1}).

The $1/e$ lifetimes obtained with an 800 nm probe are slightly shorter than the lifetimes obtained with a 400 nm probe (Figure 4.6). One possible explanation is that the 800 nm probe accesses a slightly different part of the excited state potential energy surface and its ionisation cross-section is smaller at the location of the S_1 $3s(+)/S_2$ $3p_{x,y}(+)$ conical intersection than at the vertical excitation point. This would alter the measured $1/e$ lifetime for the S_2 $3p_{x,y}(+)$ state. On the other hand, ionisation of the S_2 $3p_{x,y}(+)$ state with the 800 nm probe is a two photon process which requires more laser intensity in contrast to the single photon 400 nm probe ionisation. A high electric field intensity can produce a Stark shift, modifying potential energy surfaces and, thus, altering the dynamics.

In contrast to Albert Stolow group's results [54], our experimental data do not reveal any oscillations of the decay components. The reason for this is the different molecular temperatures. While Albert Stolow's group used a pulsed nozzle with high backing pressure, cooling rovibrational motion in the molecular beam, our setup had a warm effusive molecular source, where numerous hot bands lead to an incoherent sum of the excited state wavepackets, which reduces the contrast of the electronic revivals.

Both anisotropy coefficients for the S_2 $3p_{x,y}(+)$ component, β_2 and β_4 , have non-zero positive values. The presence of β_4 indicates some degree of molecular alignment at the instant of ionisation. The pump and probe laser field intensities were too low to cause strong field alignment of the molecules, therefore the most probable source of the alignment is a preferential excitation of the molecules with a certain orientation with respect to the laser polarisation. The probability of a single

photon transition from the initial state $|\psi_i\rangle$ into the final state $|\psi_f\rangle$ is:

$$\sigma_{f\leftarrow i} = |\langle\psi_f|\mathbf{E}\cdot\mathbf{d}|\psi_i\rangle|^2, \quad (4.5)$$

where \mathbf{E} is the laser electric field and \mathbf{d} is the transition dipole moment. From equation (4.5), it follows that during the interaction with linearly polarised light, only molecules which have a component of the transition dipole moment parallel to the electric field at the instant of interaction will be excited. As the transition dipole moment generally depends on the molecular orientation, molecules with a certain orientation will be preferentially excited in the linearly polarised laser field [159, 160].

The anisotropy of the S_2 component reduces over the pump-probe delay time. A possible explanation for this could be the dephasing of the rotational wavepacket created during the pump step [159, 160]. After the pump step, the initial rotational alignment rapidly decreases to some constant anisotropic distribution which persists until the next revival time.

4.4.2 S_1 3s(+)

The majority of the S_1 3s(+) state is populated through the S_2 3p_{x,y}(+) / S_1 3s(+) conical intersection, as a result of the non-adiabatic decay of the S_2 3p_{x,y}(+) state, which can be seen from the negative contributions in the decay associated spectra in Figure 4.8. There is no visible dependence in the decay dynamics on the excess energy in the S_2 state (Figure 4.6). Therefore, the S_2 3p_{x,y}(+) / S_1 3s(+) conical intersection must be located close to the bottom of the S_2 3p_{x,y}(+) potential well.

The sum of all decay-associated components shows the photoelectron spectrum of the initially excited states – time zero photoelectron spectrum (black lines in Figure 4.8). Although, the time zero spectrum consists mainly of the S_2 3p_{x,y}(+) peak (~ 1 eV), there is a small contribution from the S_1 3s(+) peak (~ 0.45 eV). This contribution is especially visible with the 800 nm probe wavelength. A single photon excitation $S_1(^1A'_1) \leftarrow S_0(^1A'_1)$ is forbidden in a molecule with D_{3h} symmetry, however, if torsional vibrational levels are populated the symmetry breaks down and the transition becomes allowed. Due to the low frequency of the torsional modes (58 cm^{-1} [157]) they can be thermally populated, thus allowing a single photon excitation which has been recently observed [143]. The fact that Figure 4.8 (h) has a more pronounced initially excited S_1 3s(+) component in the photoelectron

spectrum, tells us that the two photon ionisation process must have a higher cross-section for the directly excited S_1 3s(+) component than for the indirectly populated one. The only significant difference between these two components is the vibrational wavepacket in the S_1 3s(+) state. There is probably better Frank-Condon overlap with the ion state for the directly excited S_1 3s(+) component than for the indirectly populated S_1 3s(+) component when a 800 nm probe is used.

The photoelectron angular distribution of the S_1 3s(+) component shows similar constant behaviour over the studied wavelength range. A small amount of positive β_4 coefficient remains after the S_1 3s(+) \leftarrow S_2 3p_{x,y}(+) internal conversion (Figure 4.10 (b)). A single photon ionisation from a s-Rydberg state produces an electron p-wave, which is independent of the molecular orientation [39]. Therefore, the non-zero β_4 coefficients in the photoelectron angular distribution of the S_1 3s(+) component indicate not only partial preservation of the molecular alignment after the internal conversion, but also that the S_1 3s(+) state does not have a pure 3s-Rydberg character. The partial axis alignment is consistent with the remaining molecular axis anisotropy in between molecular revivals [159, 160]. Although the main contribution to the S_1 3s(+) state wavefunction is 3s-Rydberg character, it also possesses about 10% of valence character [143] which is consistent with our observation of the non-zero β_4 coefficients after a single photon ionisation.

4.5 Conclusion

Ultrafast non-adiabatic dynamics of photoexcited DABCO is another example of the break-down of the Born-Oppenheimer approximation with an efficient relaxation route of the electronically photoexcited state. The relaxation dynamics of the S_2 3p_{x,y}(+) follow a biexponential decay function in all cases, which could reflect either non-exponential kinetics or excitation of two different electronic states formed due to the Jahn-Teller interaction. A definitive interpretation of biexponential behaviour requires time-dependent quantum dynamics simulations. Our obtained time scales and decay associated spectral components reproduce the experimental data very well. The excited state population dynamics are independent of the excess energy in the excited state and it takes a similar time for the wavepacket to reach an S_2 3p_{x,y}(+) / S_1 3s(+) conical intersection for any excitation wavelength. In addition to the direct excitation of the S_2 3p_{x,y}(+) state our analysis revealed a small

direct excitation of the S_1 $3s(+)$ state which is possible due to the breaking of D_{3h} symmetry by thermal population of the torsional vibrational modes.

Our photoelectron angular distributions show preferential excitation and ionisation of the DABCO molecule along a certain molecular axis when linearly polarised light is used. However, angular-dependent cross-section calculations are required for detailed interpretation of the obtained experimental results.

Chapter 5

Summary and outlook

5.1 Ultrafast internal conversion in aniline

Previously reported studies of aniline photochemistry in the gas phase produced valuable, although indirect, information on the excited state dynamics of aniline [103, 104, 119]. Our TRPEI experiments of aniline are direct observations of the excited state relaxation dynamics which lead to some important conclusions. The second electronically excited singlet state, S_2 , in aniline is directly excited by a single photon and relaxes straight to the lower electronically excited singlet state S_1 ($\pi\pi^*$) in approximately 200 fs. The measurements of PAD provided experimental evidence that the S_2 state in aniline has a 3s Rydberg character. The decay rate of the S_1 ($\pi\pi^*$) state increases with excess energy, following a similar trend observed for the S_1 ($\pi\pi^*$) state in benzene and other benzene derivatives [39]. Direct population of the $S_3(\pi\pi^*)$ state dominates when aniline absorbs photons at wavelengths of 240–236 nm. Our analysis of TRPES data allowed us to reach a conclusion on $S_3(\pi\pi^*)$ relaxation dynamics similar to the conclusion on the $S_3(\pi\pi^*)$ state in azobenzene [43]: that the $S_3(\pi\pi^*)$ state has an efficient relaxation pathway directly to the ground electronic state associated with dynamics on a phenyl ring.

The observation of these competing non-radiative relaxation channels in aniline illustrates that its photostability arises from a subtle balance between dynamics on different potential energy surfaces and between Rydberg and valence states. As well as providing the motivation to reinvestigate the electronic relaxation of other chromophores possessing excited electronic states with mixed Rydberg-valence character, this study highlights the need for time-resolved photoelectron spectroscopy

with higher energy probe pulses to monitor both the formation of the products of dissociation and the return of population to the electronic ground state. Such experiments are difficult to perform but were proved to be possible using a VUV laser source [15].

5.2 Ultrafast internal conversion in DABCO

The excited state dynamics of DABCO show some similar features to the excited state dynamics of aniline. The S_2 $3p_{x,y}(+)$ state relaxes back to the lower S_1 $3s(+)$ state, independent of the excess energy. On the other hand, its relaxation dynamics at any excess energy follow a biexponential decay profile contrary to an expected single exponential decay for each individual electronic state. A complicated internal conversion process could cause non-exponential kinetics, although molecular dynamics simulations are required to clarify this case. Our results show direct excitation of the optically dark S_1 $3s(+)$ state due to the population of torsional motions and distortion of D_{3h} molecular symmetry which agrees with earlier work [143].

The PADs obtained from the TRPEI experiments on DABCO reveal preferential excitation of certain molecular orientations with linearly polarised light. The PAD associated with the S_1 $3s(+)$ state also reflects a contribution of the valance character to the S_1 $3s(+)$ state. The presence of a valance character in the S_1 $3s(+)$ state gives rise to the β_4 anisotropy coefficients which otherwise would be zero. A more detailed study of the DABCO PAD with better delay time sampling could be performed using a conventional electron detector based on a CCD camera, instead of a delay line detector, allowing the data acquisition rates to be significantly increased. The DABCO molecule is a good candidate for molecular alignment studies because its PAD is sensitive to the molecular orientation. TRPEI of aligned DABCO molecules would allow measurements of the PAD in the molecular frame and provide more detailed information about the molecular orbitals.

Bibliography

- [1] R. Schoenlein, L. Peteanu, R. Mathies, and C. Shank, “The first step in vision: femtosecond isomerization of rhodopsin,” *Science*, vol. 254, no. 5030, pp. 412–415, 1991.
- [2] Y.-C. Cheng and G. R. Fleming, “Dynamics of light harvesting in photosynthesis,” *Annual Review of Physical Chemistry*, vol. 60, no. 1, pp. 241–262, 2009.
- [3] H. Spanggaard and F. C. Krebs, “A brief history of the development of organic and polymeric photovoltaics,” *Solar Energy Materials and Solar Cells*, vol. 83, no. 2-3, pp. 125 – 146, 2004.
- [4] J. E. Guillet, J. Dhanraj, F. J. Golemba, and G. H. Hartley, *Fundamental Processes in the Photodegradation of Polymers*, vol. 85, ch. 19, pp. 272–286. American Chemical Society, 1968.
- [5] F. de Gruijl, “Skin cancer and solar UV radiation,” *Eur. J. Cancer*, vol. 35, pp. 2003–2009, 1999.
- [6] M. Ichihashi, M. Ueda, A. Budiyanoto, T. Bito, M. Oka, M. Fukunaga, K. Tsuru, and T. Horikawa, “UV–induced skin damage,” *Toxicology*, vol. 189, pp. 21–39, 2003.
- [7] H. Satzger, D. Townsend, M. Z. Zgierski, S. Patchkovskii, S. Ullrich, and A. Stolow, “Primary processes underlying the photostability of isolated DNA bases: Adenine,” *P. Natl. Acad. Sci. USA*, vol. 103, pp. 10196–10201, 2006.
- [8] C. Z. Bisgaard, H. Satzger, S. Ullrich, and A. Stolow, “Excited-state dynamics of isolated DNA bases: A case study of adenine,” *Chem. Phys. Chem.*, vol. 10, pp. 101–110, 2009.

- [9] C. T. Middleton, K. de La Harpe, C. Su, Y. K. Law, C. E. Crespo-Hernandez, and B. Kohler, "DNA excited-state dynamics: From single bases to the double helix," in *Annual Review of Physical Chemistry*, vol. 60, pp. 217–239, Palo Alto: Annual Reviews, 2009.
- [10] A. Iqbal and V. G. Stavros, "Active participation of $^1\pi\sigma^*$ states in the photodissociation of tyrosine and its subunits," *J. Phys. Chem. Lett.*, vol. 1, pp. 2274–2278, 2010.
- [11] N. F. Scherer, J. L. Knee, D. D. Smith, and A. H. Zewail, "Femtosecond photofragment spectroscopy of the reaction iodine cyanide (ICN) \rightarrow cyanogen (CN) + atomic iodine," *The Journal of Physical Chemistry*, vol. 89, no. 24, pp. 5141–5143, 1985.
- [12] A. H. Zewail, "Femtochemistry: Atomic-scale dynamics of the chemical bond," *The Journal of Physical Chemistry A*, vol. 104, no. 24, pp. 5660–5694, 2000.
- [13] A. Stolow, A. E. Bragg, and D. M. Neumark, "Femtosecond time-resolved photoelectron spectroscopy," *Chem. Rev.*, vol. 104, pp. 1719–1757, 2004.
- [14] I. V. Hertel and W. Radloff, "Ultrafast dynamics in isolated molecules and molecular clusters," *Reports on Progress in Physics*, vol. 69, no. 6, p. 1897, 2006.
- [15] T. Suzuki, "Time-resolved photoelectron spectroscopy of non-adiabatic electronic dynamics in gas and liquid phases," *International Reviews in Physical Chemistry*, vol. 31, no. 2, pp. 265–318, 2012.
- [16] G. Wu, P. Hockett, and A. Stolow, "Time-resolved photoelectron spectroscopy: from wavepackets to observables," *Phys. Chem. Chem. Phys.*, vol. 13, pp. 18447–18467, 2011.
- [17] A. Messiah, *Quantum Mechanics*, ch. Stationary perturbations and the variational method. Unabridged Dover, 1999.
- [18] G. A. Worth and L. S. Cederbaum, "Beyond Born-Oppenheimer: Molecular dynamics through a conical intersection," *Annual Review of Physical Chemistry*, vol. 55, no. 1, pp. 127–158, 2004.

- [19] M. Born and R. Oppenheimer, “Zur quantentheorie der molekeln,” *Annalen der Physik*, vol. 389, no. 20, pp. 457–484, 1927.
- [20] G. Herzberg, *The Spectra and Structures of Simple Free Radicals*, ch. Diatomic Radicals and Ions. Cornell University Press Ithaca and London, 1971.
- [21] J. M. Hollas, *High Resolution Spectroscopy*, ch. Quantization of Energy. John Wiley & Sons Ltd, West Sussex, England, 1998.
- [22] L. Gonzalez, D. Escudero, and L. Serrano-Andres, “Progress and challenges in the calculation of electronic excited states,” *ChemPhysChem*, vol. 13, no. 1, pp. 28–51, 2012.
- [23] M. Bixon and J. Jortner, “Intramolecular radiationless transitions,” *The Journal of Chemical Physics*, vol. 48, no. 2, pp. 715–726, 1968.
- [24] H. Koeuppel, W. Domcke, and L. S. Cederbaum, *Multimode Molecular Dynamics Beyond the Born-Oppenheimer Approximation*, pp. 59–246. John Wiley & Sons, Inc., 2007.
- [25] J. Jortner, S. A. Rice, and R. M. Hochstrasser, *Radiationless Transitions in Photochemistry*, pp. 149–309. John Wiley & Sons, Inc., 2007.
- [26] L. J. Butler, “Chemical reaction dynamics beyond the Born-Oppenheimer approximation,” *Annual Review of Physical Chemistry*, vol. 49, no. 1, pp. 125–171, 1998.
- [27] L. S. Cederbaum, H. Koeppel, and W. Domcke, “Multimode vibronic coupling effects in molecules,” *International Journal of Quantum Chemistry*, vol. 20, no. S15, pp. 251–267, 1981.
- [28] L. Cederbaum, W. Domcke, H. Koeppel, and W. V. Niessen, “Strong vibronic coupling effects in ionization spectra: The ‘mystery band’ of butatriene,” *Chemical Physics*, vol. 26, no. 2, pp. 169 – 177, 1977.
- [29] W. Radloff, V. Stert, T. Freudenberg, I. V. Hertel, C. Jouvét, C. Dedonder-Lardeux, and D. Solgadi, “Internal conversion in highly excited benzene and benzene dimer: femtosecond time-resolved photoelectron spectroscopy,” *Chemical Physics Letters*, vol. 281, no. 1-3, pp. 20 – 26, 1997.

- [30] S. Matsika and P. Krause, “Nonadiabatic events and conical intersections,” *Annual Review of Physical Chemistry*, vol. 62, no. 1, pp. 621–643, 2011.
- [31] D. F. Heller and S. Mukamel, “Theory of vibrational overtone line shapes of polyatomic molecules,” *The Journal of Chemical Physics*, vol. 70, no. 1, pp. 463–472, 1979.
- [32] J. S. Hutchinson, W. P. Reinhardt, and J. T. Hynes, “Nonlinear resonances and vibrational energy flow in model hydrocarbon chains,” *The Journal of Chemical Physics*, vol. 79, no. 9, pp. 4247–4260, 1983.
- [33] E. L. Sibert III, W. P. Reinhardt, and J. T. Hynes, “Intramolecular vibrational relaxation of CH overtones in benzene,” *Chemical Physics Letters*, vol. 92, no. 5, pp. 455 – 458, 1982.
- [34] T. A. Stephenson, P. L. Radloff, and S. A. Rice, “ ${}^1B_{2u} \longleftrightarrow {}^1A_{1g}$ spectroscopy of jet-cooled benzene: Single vibronic level fluorescence studies,” *The Journal of Chemical Physics*, vol. 81, no. 3, pp. 1060–1072, 1984.
- [35] G. J. Atchity, S. S. Xantheas, and K. Ruedenberg, “Potential energy surfaces near intersections,” *The Journal of Chemical Physics*, vol. 95, no. 3, pp. 1862–1876, 1991.
- [36] W. Greiner, *Quantum Mechanics: An introduction*, p. 310. Springer, 2001.
- [37] E. Condon, “A theory of intensity distribution in band systems,” *Phys. Rev.*, vol. 28, pp. 1182–1201, Dec 1926.
- [38] S. K. Lower and M. A. El-Sayed, “The triplet state and molecular electronic processes in organic molecules,” *Chemical Reviews*, vol. 66, no. 2, pp. 199–241, 1966.
- [39] A. Stolow and J. G. Underwood, *Time-Resolved Photoelectron Spectroscopy of Nonadiabatic Dynamics in Polyatomic Molecules*, pp. 497–584. John Wiley & Sons, Inc., 2008.
- [40] V. Blanchet, M. Z. Zgierski, T. Seideman, and A. Stolow, “Discerning vibronic molecular dynamics using time-resolved photoelectron spectroscopy,” *Nature*, vol. 401, pp. 52–54, Sept 1999.

- [41] M. Kasha, "Characterization of electronic transitions in complex molecules," *Discuss. Faraday Soc.*, vol. 9, pp. 14–19, 1950.
- [42] M. N. R. Ashfold, B. Cronin, A. L. Devine, R. N. Dixon, and M. G. Nix, "The role of $\pi\sigma^*$ excited states in the photodissociation of heteroaromatic molecules," *Science*, vol. 312, pp. 1637–1640, 2006.
- [43] T. Schultz, J. Quenneville, B. Levine, A. Toniolo, T. J. Martinez, S. Lochbrunner, M. Schmitt, J. P. Shaffer, M. Z. Zgierski, and A. Stolow, "Mechanism and dynamics of azobenzene photoisomerization," *Journal of the American Chemical Society*, vol. 125, no. 27, pp. 8098–8099, 2003.
- [44] T. Koopmans, "Ueber die zuordnung von wellenfunktionen und eigenwerten zu den einzelnen elektronen eines atoms," *Physica*, vol. 1, no. 1 - 6, pp. 104 – 113, 1934.
- [45] V. Blanchet, M. Z. Zgierski, and A. Stolow, "Electronic continua in time-resolved photoelectron spectroscopy. I. Complementary ionization correlations," *The Journal of Chemical Physics*, vol. 114, no. 3, pp. 1194–1205, 2001.
- [46] M. Schmitt, S. Lochbrunner, J. P. Shaffer, J. J. Larsen, M. Z. Zgierski, and A. Stolow, "Electronic continua in time-resolved photoelectron spectroscopy. II. Corresponding ionization correlations," *The Journal of Chemical Physics*, vol. 114, no. 3, pp. 1206–1213, 2001.
- [47] K. L. Reid, "Photoelectron angular distributions," *Annual Review of Physical Chemistry*, vol. 54, no. 1, pp. 397–424, 2003.
- [48] R. Signorell and F. Merkt, "General symmetry selection rules for the photoionization of polyatomic molecules," *Molecular Physics*, vol. 92, no. 5, pp. 793–804, 1997.
- [49] C. N. Yang, "On the angular distribution in nuclear reactions and coincidence measurements," *Phys. Rev.*, vol. 74, pp. 764–772, Oct 1948.
- [50] O. Geßner, A. M. D. Lee, J. P. Shaffer, H. Reisler, S. V. Levchenko, A. I. Krylov, J. G. Underwood, H. Shi, A. L. L. East, D. M. Wardlaw, E. t. H. Chrysostom, C. C. Hayden, and A. Stolow, "Femtosecond multidimensional

- imaging of a molecular dissociation,” *Science*, vol. 311, no. 5758, pp. 219–222, 2006.
- [51] Y.-I. Suzuki, T. Horio, T. Fuji, and T. Suzuki, “Time-resolved photoelectron imaging of $S_2 \rightarrow S_1$ internal conversion in benzene and toluene,” *The Journal of Chemical Physics*, vol. 134, no. 18, p. 184313, 2011.
- [52] T. Suzuki, “Femtosecond time-resolved photoelectron imaging,” *Annu. Rev. Phys. Chem.*, vol. 57, pp. 555–592, 2006.
- [53] T. Seideman, “Time-resolved photoelectron angular distributions: Concepts, applications, and directions,” *Annu. Rev. Phys. Chem.*, vol. 53, pp. 41–65, 2002.
- [54] A. E. Boguslavskiy, M. S. Schuurman, D. Townsend, and A. Stolow, “Non-Born-Oppenheimer wavepacket dynamics in polyatomic molecules: vibrations at conical intersections in DABCO,” *Faraday Discuss.*, vol. 150, pp. 419–438, 2011.
- [55] J. A. Davies, A. M. Green, and K. L. Reid, “Deducing anharmonic coupling matrix elements from picosecond time-resolved photoelectron spectra: application to S_1 toluene at low vibrational energy,” *Phys. Chem. Chem. Phys.*, vol. 12, pp. 9872–9883, 2010.
- [56] C. J. Hammond, K. L. Reid, and K. L. Ronayne, “Observation of a simple vibrational wavepacket in a polyatomic molecule via time-resolved photoelectron velocity-map imaging: A prototype for time-resolved IVR studies,” *The Journal of Chemical Physics*, vol. 124, no. 20, p. 201102, 2006.
- [57] E. C. Lim and S. K. Chakrabarti, “Role of $1 \rightarrow a_\pi$ transitions in Spin—Orbit coupling of aromatic amines: Phosphorescence of aniline and its N-Alkyl derivatives,” *The Journal of Chemical Physics*, vol. 47, no. 11, pp. 4726–4730, 1967.
- [58] A. Gonzalez-Lafont, J. Lluch, J. Bertran, and J. Marquet, “Excited states and electronic spectra of monosubstituted benzenes. An AM1 study,” *Spectrochimica Acta Part A: Molecular Spectroscopy*, vol. 44, no. 12, pp. 1427 – 1434, 1988.

- [59] X.-J. Hou, P. Quan, T. Hölzl, T. Veszpremi, and M. T. Nguyen, “Theoretical study of low-lying triplet states of aniline,” *The Journal of Physical Chemistry A*, vol. 109, no. 45, pp. 10396–10402, 2005.
- [60] B. Kim, C. P. Schick, and P. M. Weber, “Time-delayed two-color photoelectron spectra of aniline, 2-aminopyridine, and 3-aminopyridine: Snapshots of the nonadiabatic curve crossings,” *The Journal of Chemical Physics*, vol. 103, no. 16, pp. 6903–6913, 1995.
- [61] T. Debies and J. Rabalais, “Photoelectron spectra of substituted benzenes: II. Seven valence electron substituents,” *Journal of Electron Spectroscopy and Related Phenomena*, vol. 1, no. 4, pp. 355 – 370, 1972.
- [62] T. Brabec and F. Krausz, “Intense few-cycle laser fields: Frontiers of nonlinear optics,” *Rev. Mod. Phys.*, vol. 72, pp. 545–591, Apr 2000.
- [63] U. Keller, “Recent developments in compact ultrafast lasers,” *Nature*, vol. 424, pp. 831–838, Aug 2003.
- [64] D. C. Edelstein, E. S. Wachman, L. K. Cheng, W. R. Bosenberg, and C. L. Tang, “Femtosecond ultraviolet pulse generation in β -BaB₂O₄,” *Applied Physics Letters*, vol. 52, no. 26, pp. 2211–2213, 1988.
- [65] K. Kato, “Second-harmonic generation to 2048 Å in β -BaB₂O₄,” *IEEE Journal of Quantum Electronics*, vol. 22, pp. 1013 – 1014, jul 1986.
- [66] M. Nisoli, S. D. Silvestri, V. Magni, O. Svelto, R. Danielius, A. Piskarskas, G. Valiulis, and A. Varanavicius, “Highly efficient parametric conversion of femtosecond Ti:sapphire laser pulses at 1 kHz,” *Opt. Lett.*, vol. 19, pp. 1973–1975, Dec 1994.
- [67] T. Wilhelm, J. Piel, and E. Riedle, “Sub-20-fs pulses tunable across the visible from a blue-pumped single-pass noncollinear parametric converter,” *Opt. Lett.*, vol. 22, pp. 1494–1496, Oct 1997.
- [68] M. K. Reed, M. K. Steiner-Shepard, M. S. Armas, and D. K. Negus, “Microjoule-energy ultrafast optical parametric amplifiers,” *J. Opt. Soc. Am. B*, vol. 12, pp. 2229–2236, Nov 1995.

- [69] A. Brodeur and S. L. Chin, “Ultrafast white-light continuum generation and self-focusing in transparent condensed media,” *J. Opt. Soc. Am. B*, vol. 16, pp. 637–650, Apr 1999.
- [70] F. Krausz and M. Ivanov, “Attosecond physics,” *Rev. Mod. Phys.*, vol. 81, pp. 163–234, Feb 2009.
- [71] E. Goulielmakis, M. Schultze, M. Hofstetter, V. S. Yakovlev, J. Gagnon, M. Uiberacker, A. L. Aquila, E. M. Gullikson, D. T. Attwood, R. Kienberger, F. Krausz, and U. Kleineberg, “Single-cycle nonlinear optics,” *Science*, vol. 320, no. 5883, pp. 1614–1617, 2008.
- [72] T. Pfeifer, M. J. Abel, P. M. Nagel, A. Jullien, Z.-H. Loh, M. J. Bell, D. M. Neumark, and S. R. Leone, “Time-resolved spectroscopy of attosecond quantum dynamics,” *Chemical Physics Letters*, vol. 463, no. 1-3, pp. 11 – 24, 2008.
- [73] M. Abd-Elmeguid *et al.*, *TESLA Technical Design Report*, ch. 5. The X-Ray Free Electron Laser. DESY, 2001.
- [74] K. Tiedtke, A. Azima, N. von Bargen, L. Bittner, S. Bonfigt, S. Duesterer, B. Faatz, U. Fruehling, M. Gensch, C. Gerth, N. Guerassimova, U. Hahn, T. Hans, M. Hesse, K. Honkavaar, U. Jastrow, P. Juranic, S. Kapitzki, B. Keitel, T. Kracht, M. Kuhlmann, W. B. Li, M. Martins, T. Nunez, E. Ploenjes, H. Redlin, E. L. Saldin, E. A. Schneidmiller, J. R. Schneider, S. Schreiber, N. Stojanovic, F. Tavella, S. Toleikis, R. Treusch, H. Weigelt, M. Wellhoefer, H. Wabnitz, M. V. Yurkov, and J. Feldhaus, “The soft x-ray free-electron laser FLASH at DESY: beamlines, diagnostics and end-stations,” *New Journal of Physics*, vol. 11, no. 2, p. 023029, 2009.
- [75] P. Emma, R. Akre, J. Arthur, R. Bionta, C. Bostedt, J. Bozek, A. Brachmann, P. Bucksbaum, R. Coffee, F.-J. Decker, Y. Ding, D. Dowell, S. Edstrom, A. Fisher, J. Frisch, S. Gilevich, J. Hastings, G. Hays, P. Hering, Z. Huang, R. Iverson, H. Loos, M. Messerschmidt, A. Miahnahri, S. Moeller, H.-D. Nuhn, G. Pile, D. Ratner, J. Rzepiela, D. Schultz, T. Smith, P. Stefan, H. Tompkins, J. Turner, J. Welch, W. White, J. Wu, G. Yocky, and J. Galayda, “First lasing and operation of an angstrom-wavelength free-electron laser,” *Nat Photon*, vol. 4, no. 9, pp. 641–647, 2010.

- [76] A. Azima, S. Dusterer, P. Radcliffe, H. Redlin, N. Stojanovic, W. Li, H. Schlarb, J. Feldhaus, D. Cubaynes, M. Meyer, J. Dardis, P. Hayden, P. Hough, V. Richardson, E. T. Kennedy, and J. T. Costello, "Time-resolved pump-probe experiments beyond the jitter limitations at FLASH," *Applied Physics Letters*, vol. 94, no. 14, p. 144102, 2009.
- [77] S. J. Buckman, R. J. Gulley, M. Moghbelalhossein, and S. J. Bennett, "Spatial profiles of effusive molecular beams and their dependence on gas species," *Measurement Science and Technology*, vol. 4, no. 10, p. 1143, 1993.
- [78] R. Campargue, "Progress in overexpanded supersonic jets and skimmed molecular beams in free-jet zones of silence," *The Journal of Physical Chemistry*, vol. 88, no. 20, pp. 4466–4474, 1984.
- [79] J. B. Anderson and J. B. Fenn, "Velocity distributions in molecular beams from nozzle sources," *Physics of Fluids*, vol. 8, no. 5, pp. 780–787, 1965.
- [80] A. Amirav, U. Even, and J. Jortner, "Cooling of large and heavy molecules in seeded supersonic beams," *Chemical Physics*, vol. 51, no. 1-2, pp. 31 – 42, 1980.
- [81] P. M. Mayer and T. Baer, "A photoionization study of vibrational cooling in molecular beams," *International Journal of Mass Spectrometry and Ion Processes*, vol. 156, no. 3, pp. 133 – 139, 1996.
- [82] U. Even, J. Jortner, D. Noy, N. Lavie, and C. Cossart-Magos, "Cooling of large molecules below 1 K and He clusters formation," *The Journal of Chemical Physics*, vol. 112, no. 18, pp. 8068–8071, 2000.
- [83] M. Faubel and T. Kisters, "Non-equilibrium molecular evaporation of carboxylic acid dimers," *Nature*, vol. 339, no. 6225, pp. 527 – 529, 1989.
- [84] A. Charvat, E. Lugovoj, M. Faubel, and B. Abel, "New design for a time-of-flight mass spectrometer with a liquid beam laser desorption ion source for the analysis of biomolecules," *Review of Scientific Instruments*, vol. 75, no. 5, pp. 1209–1218, 2004.

- [85] M. Faubel, K. R. Siefermann, Y. Liu, and B. Abel, “Ultrafast soft x-ray photoelectron spectroscopy at liquid water microjets,” *Accounts of Chemical Research*, vol. 45, no. 1, pp. 120–130, 2012.
- [86] Y. Tang, H. Shen, K. Sekiguchi, N. Kurahashi, T. Mizuno, Y.-I. Suzuki, and T. Suzuki, “Direct measurement of vertical binding energy of a hydrated electron,” *Phys. Chem. Chem. Phys.*, vol. 12, pp. 3653–3655, 2010.
- [87] S. Anderson, D. Rider, and R. Zare, “Multiphoton ionization photoelectron spectroscopy: a new method for determining vibrational structure of molecular ions,” *Chemical Physics Letters*, vol. 93, no. 1, pp. 11 – 15, 1982.
- [88] P. Kruit and F. H. Read, “Magnetic field paralleliser for 2 electron-spectrometer and electron-image magnifier,” *Journal of Physics E: Scientific Instruments*, vol. 16, no. 4, p. 313, 1983.
- [89] A. T. J. B. Eppink and D. H. Parker, “Velocity map imaging of ions and electrons using electrostatic lenses: Application in photoelectron and photofragment ion imaging of molecular oxygen,” *Review of Scientific Instruments*, vol. 68, no. 9, pp. 3477–3484, 1997.
- [90] A. T. J. B. Eppink, S.-M. Wu, and B. J. Whitaker, *Imaging in Molecular Dynamics*, ch. Reconstruction methods. Cambridge University Press, 2003.
- [91] S. J. Cavanagh, S. T. Gibson, M. N. Gale, C. J. Dedman, E. H. Roberts, and B. R. Lewis, “High-resolution velocity-map-imaging photoelectron spectroscopy of the O^- photodetachment fine-structure transitions,” *Phys. Rev. A*, vol. 76, p. 052708, Nov 2007.
- [92] G. Szabó, Z. Bor, and A. Müller, “Phase-sensitive single-pulse autocorrelator for ultrashort laser pulses,” *Opt. Lett.*, vol. 13, pp. 746–748, Sep 1988.
- [93] K. W. DeLong, R. Trebino, J. Hunter, and W. E. White, “Frequency-resolved optical gating with the use of second-harmonic generation,” *J. Opt. Soc. Am. B*, vol. 11, pp. 2206–2215, Nov 1994.
- [94] I. C. E. Turcu, E. Springate, C. A. Froud, C. M. Cacho, J. L. Collier, W. A. Bryan, G. R. A. J. Nemeth, J. P. Marangos, J. W. G. Tisch, R. Torres,

- T. Siegel, L. Brugnera, J. G. Underwood, I. Procino, W. R. Newell, C. Altucci, R. Velotta, R. B. King, J. D. Alexander, C. R. Calvert, O. Kelly, J. B. Greenwood, I. D. Williams, A. Cavalleri, J. C. Petersen, N. Dean, S. S. Dhesi, L. Poletto, P. Villorosi, F. Frassetto, S. Bonora, and M. D. Roper, “Ultrafast science and development at the Artemis facility,” vol. 7469, p. 746902, SPIE, 2009.
- [95] RoentDek Handels GmbH, *MCP Delay Line Detector Manual*, 9.22.1003.1 ed., 2010.
- [96] G. A. Garcia, L. Nahon, and I. Powis, “Two-dimensional charged particle image inversion using a polar basis function expansion,” *Review of Scientific Instruments*, vol. 75, no. 11, pp. 4989–4996, 2004.
- [97] G. M. Roberts, J. L. Nixon, J. Lecointre, E. Wrede, and J. R. R. Verlet, “Toward real-time charged-particle image reconstruction using polar onion-peeling,” *Review of Scientific Instruments*, vol. 80, no. 5, p. 053104, 2009.
- [98] V. Dribinski, A. Ossadtchi, V. A. Mandelshtam, and H. Reisler, “Reconstruction of abel-transformable images: The gaussian basis-set expansion abel transform method,” *Review of Scientific Instruments*, vol. 73, no. 7, pp. 2634–2642, 2002.
- [99] “J.R.R. Verlet, “Image deconvolution using polar onion peeling,” October 2012. <http://www.dur.ac.uk/chemistry/lsd/groups/j.r.r.verlet/research/clusters/pop/>.”
- [100] W. T. Eadie, D. Drijard, F. James, M. Roos, and B. Sadoulet, *Statistical Methods in Experimental Physics*, pp. 163–172. North-Holland, 1971.
- [101] R. Brun and F. Rademakers, “TROOT - an object oriented data analysis framework,” *Proceedings AIHENP’96 Workshop, Lausanne, Sep. 1996, Nucl. Inst. Meth. in Phys. Res. A 389 (1997) 81-86*.
See also <http://root.cern.ch/>.
- [102] W. T. Eadie, D. Drijard, F. James, M. Roos, and B. Sadoulet, *Statistical Methods in Experimental Physics*, pp. 204–205. North-Holland, 1971.

- [103] G. A. King, T. A. A. Oliver, and M. N. R. Ashfold, "Dynamical insights into ${}^1\pi\sigma^*$ state mediated photodissociation of aniline," *The Journal of Chemical Physics*, vol. 132, no. 21, p. 214307, 2010.
- [104] R. Montero, A. P. Conde, V. Ovejas, R. Martinez, F. Castano, and A. Longarte, "Ultrafast dynamics of aniline in the 294-234 nm excitation range: The role of the $\pi\sigma^*$ state," *The Journal of Chemical Physics*, vol. 135, no. 5, p. 054308, 2011.
- [105] T. Ebata, C. Minejima, and N. Mikami, "A new electronic state of aniline observed in the transient IR absorption spectrum from S_1 in a supersonic jet," *The Journal of Physical Chemistry A*, vol. 106, no. 46, pp. 11070–11074, 2002.
- [106] Y. Honda, M. Hada, M. Ehara, and H. Nakatsuji, "Excited and ionized states of aniline: Symmetry adapted cluster configuration interaction theoretical study," *The Journal of Chemical Physics*, vol. 117, no. 5, pp. 2045–2052, 2002.
- [107] H. Reisler and A. I. Krylov, "Interacting rydberg and valence states in radicals and molecules: experimental and theoretical studies," *International Reviews in Physical Chemistry*, vol. 28, no. 2, pp. 267–308, 2009.
- [108] A. L. Sobolewski, W. Domcke, C. Dedonder-Lardeux, and C. Jouvet, "Excited-state hydrogen detachment and hydrogen transfer driven by repulsive ${}^1\pi\sigma^*$ states: A new paradigm for nonradiative decay in aromatic biomolecules," *Phys. Chem. Chem. Phys.*, vol. 4, pp. 1093–1100, 2002.
- [109] M. N. R. Ashfold, G. A. King, D. Murdock, M. G. Nix, T. A. A. Oliver, and A. G. Sage, " $\pi\sigma^*$ excited states in molecular photochemistry," *Phys. Chem. Chem. Phys.*, vol. 12, p. 1218, 2010.
- [110] R. N. Dixon, T. A. A. Oliver, and M. N. R. Ashfold, "Tunnelling under a conical intersection: Application to the product vibrational state distributions in the UV photodissociation of phenols," *J. Chem. Phys.*, vol. 134, p. 194303, 2011.
- [111] Z. Lan, W. Domcke, V. Vallet, A. L. Sobolewski, and S. Mahapatra, "Time-dependent quantum wave-packet description of the ${}^1\pi\sigma^*$ photochemistry of phenol," *The Journal of Chemical Physics*, vol. 122, pp. 224315–224315, 2005.

- [112] D. Lister, J. Tyler, J. Hog, and N. Larsen, "The microwave spectrum, structure and dipole moment of aniline," *Journal of Molecular Structure*, vol. 23, no. 2, pp. 253 – 264, 1974.
- [113] G. Schultz, G. Portalone, F. Ramondo, A. Domenicano, and I. Hargittai, "Molecular structure of aniline in the gaseous phase: A concerted study by electron diffraction and ab initio molecular orbital calculations," *Structural Chemistry*, vol. 7, pp. 59–71, 1996.
- [114] P. M. Wojciechowski, W. Zierkiewicz, D. Michalska, and P. Hobza, "Electronic structures, vibrational spectra, and revised assignment of aniline and its radical cation: Theoretical study," *The Journal of Chemical Physics*, vol. 118, no. 24, pp. 10900–10911, 2003.
- [115] N. Vakula, G. Kuramshina, S. Makhmutova, and Y. Pentin, "DFT theoretical studies of anions of aniline and its several derivatives," *Structural Chemistry*, vol. 22, pp. 345–356, 2011.
- [116] K. Kimura, H. Tsubomura, and S. Nagakura, "The vacuum ultraviolet absorption spectra of aniline and some of its N-derivatives," *Bulletin of the Chemical Society of Japan*, vol. 37, no. 9, pp. 1336–1346, 1964.
- [117] X. Song, M. Yang, E. R. Davidson, and J. P. Reilly, "Zero kinetic energy photoelectron spectra of jet-cooled aniline," *The Journal of Chemical Physics*, vol. 99, no. 5, pp. 3224–3233, 1993.
- [118] M. Sala, "Equilibrium structure of the ground and electronically excited singlet states of aniline." private communication, 2012.
- [119] G. M. Roberts, C. A. Williams, J. D. Young, S. Ullrich, M. J. Paterson, and V. G. Stavros, "Unraveling ultrafast dynamics in photoexcited aniline," *Journal of the American Chemical Society*, vol. 134, no. 30, pp. 12578–12589, 2012.
- [120] W. E. Sinclair and D. W. Pratt, "Structure and vibrational dynamics of aniline and aniline–Ar from high resolution electronic spectroscopy in the gas phase," *The Journal of Chemical Physics*, vol. 105, no. 18, pp. 7942–7956, 1996.

- [121] C. Gee, S. Douin, C. Crepin, and P. Brechignac, "Infrared spectroscopy of aniline ($C_6H_5NH_2$) and its cation in a cryogenic argon matrix," *Chemical Physics Letters*, vol. 338, no. 2-3, pp. 130 – 136, 2001.
- [122] R. Kydd and P. Krueger, "The far-infrared vapour phase spectra of aniline- ND_2 and aniline-NHD," *Chemical Physics Letters*, vol. 49, no. 3, pp. 539 – 543, 1977.
- [123] N. Larsen, E. Hansen, and F. Nicolaisen, "Far infrared investigation of aniline and 4-fluoroaniline in the vapour phase. Inversion and torsion of the amino group," *Chemical Physics Letters*, vol. 43, no. 3, pp. 584 – 586, 1976.
- [124] T. Nakanaga, F. Ito, J. Miyawaki, K. Sugawara, and H. Takeo, "Observation of the infrared spectra of the NH_2 -stretching vibration modes of aniline- Ar_n ($n = 1, 2$) clusters in a supersonic jet using REMPI," *Chemical Physics Letters*, vol. 261, no. 4-5, pp. 414 – 420, 1996.
- [125] J. T. Meek, E. Sekreta, W. Wilson, K. S. Viswanathan, and J. P. Reilly, "The laser photoelectron spectrum of gas phase aniline," *The Journal of Chemical Physics*, vol. 82, no. 4, pp. 1741–1749, 1985.
- [126] N. Mikami, A. Hiraya, I. Fujiwara, and M. Ito, "The fluorescence excitation spectrum of aniline in a supersonic free jet: Double minimum potential for the inversion vibration in the excited state," *Chemical Physics Letters*, vol. 74, no. 3, pp. 531 – 535, 1980.
- [127] C. Gee, A. Cuisset, L. Divay, and C. Crepin, "Electronic relaxation of aniline in argon matrix: A site selective laser spectroscopy," *The Journal of Chemical Physics*, vol. 116, no. 12, pp. 4993–5001, 2002.
- [128] S. Sarkar and G. Kastha, "Environmental effects on the absorption and luminescence properties of aromatic amines: Aniline," *Spectrochimica Acta Part A: Molecular Spectroscopy*, vol. 48, no. 11-12, pp. 1611 – 1624, 1992.
- [129] R. Scheps, D. Florida, and S. A. Rice, "Influence of large amplitude vibrational motion on the rate of intersystem crossing: A study of single vibronic level fluorescence from aniline- h_7 , aniline N, N- d_2 , aniline- d_5 , and aniline- d_7 ," *The Journal of Chemical Physics*, vol. 61, no. 5, pp. 1730–1747, 1974.

- [130] T. Penfold and G. Worth, "The effect of molecular distortions on spin-orbit coupling in simple hydrocarbons," *Chemical Physics*, vol. 375, no. 1, pp. 58–66, 2010.
- [131] D. S. N. Parker, R. S. Minns, T. J. Penfold, G. A. Worth, and H. H. Fielding, "Ultrafast dynamics of the S_1 excited state of benzene," *Chem. Phys. Lett.*, vol. 469, pp. 43–47, 2009.
- [132] R. S. Minns, D. S. N. Parker, T. J. Penfold, G. A. Worth, and H. H. Fielding, "Competing ultrafast intersystem crossing and internal conversion in the "channel 3" region of benzene," *Phys. Chem. Chem. Phys.*, vol. 12, pp. 15607–15615, 2010.
- [133] P. A. MacFaul, D. D. M. Wayner, and K. U. Ingold, "Measurement of NH bond strengths in aromatic amines by photoacoustic calorimetry," *The Journal of Organic Chemistry*, vol. 62, no. 10, pp. 3413–3414, 1997.
- [134] C. Buth and R. Santra, "Rotational molecular dynamics of laser-manipulated bromotrifluoromethane studied by x-ray absorption," *The Journal of Chemical Physics*, vol. 129, p. 134312, 2008.
- [135] E. R. T. Kerstel, M. Becucci, G. Pietraperzia, D. Consalvo, and E. Castellucci, "Molecular beam spectroscopy of S_1 aniline: Assignments for the 0_0^0 , $6a_0^1$, I_0^2 , and 1_0^1 rovibronic bands," *Journal of Molecular Spectroscopy*, vol. 177, pp. 74–78, 1996.
- [136] A. M. D. Lee, J. D. Coe, S. Ullrich, M.-L. Ho, S.-J. Lee, B.-M. Cheng, M. Z. Zgierski, I.-C. Chen, T. J. Martinez, and A. Stolow, "Substituent effects on dynamics at conical intersections: α, β -enones," *J. Phys. Chem. A*, vol. 111, pp. 11948–11960, 2007.
- [137] O. Schalk, A. E. Boguslavskiy, and A. Stolow, "Substituent effects on dynamics at conical intersections: Cyclopentadienes," *The Journal of Physical Chemistry A*, vol. 114, no. 12, pp. 4058–4064, 2010.
- [138] R. Livingstone, O. Schalk, A. E. Boguslavskiy, G. Wu, L. T. Bergendahl, A. Stolow, M. J. Paterson, and D. Townsend, "Following the excited state

- relaxation dynamics of indole and 5-hydroxyindole using time-resolved photoelectron spectroscopy,” *The Journal of Chemical Physics*, vol. 135, no. 19, p. 194307, 2011.
- [139] M. Quack and M. Stockburger, “Resonance fluorescence of aniline vapour,” *Journal of Molecular Spectroscopy*, vol. 43, no. 1, pp. 87 – 116, 1972.
- [140] J. S. Lim and S. K. Kim, “Experimental probing of conical intersection dynamics in the photodissociation of thioanisole,” *Nat. Chem.*, vol. 2, pp. 627–632, 2010.
- [141] D.-S. Ahn, J. Lee, J.-M. Choi, K.-S. Lee, S. J. Baek, K. Lee, K.-K. Baek, and S. K. Kim, “State-selective predissociation dynamics of methylamines: The vibronic and H/D effects on the conical intersection dynamics,” *The Journal of Chemical Physics*, vol. 128, no. 22, p. 224305, 2008.
- [142] A. Yokozeki and K. Kuchitsu, “Structure and intramolecular motions in triethylenediamine as studied by gas electron diffraction,” *Bulletin of the Chemical Society of Japan*, vol. 44, pp. 72–77, 1971.
- [143] L. Poisson, R. Maksimenska, B. Soep, J.-M. Mestdagh, D. H. Parker, M. Nsangou, and M. Hochlaf, “Unusual quantum interference in the S_1 state of DABCO and observation of intramolecular vibrational redistribution,” *The Journal of Physical Chemistry A*, vol. 114, no. 9, pp. 1089–5639, 2010.
- [144] A. M. Halpern, J. L. Roebber, and K. Weiss, “Electronic structure of cage amines: Absorption spectra of triethylenediamine and quinuclidine,” *The Journal of Chemical Physics*, vol. 49, no. 3, pp. 1348–1357, 1968.
- [145] V. Galasso, “Theoretical study of the low-lying excited states of ABCO, DABCO and homologous cage amines,” *Chemical Physics*, vol. 215, no. 2, pp. 183 – 190, 1997.
- [146] M. J. Watkins and M. C. R. Cockett, “Adiabatic and vertical ionization energies of 1,4-diazabicyclo[2,2,2]-octane measured by zero electron kinetic energy spectroscopy and Rydberg extrapolation,” *The Journal of Chemical Physics*, vol. 113, no. 23, pp. 10560–10571, 2000.

- [147] P. Avouris and A. R. Rossi, "Low-energy electronic transitions of alkylamines," *The Journal of Physical Chemistry*, vol. 85, no. 16, pp. 2340–2344, 1981.
- [148] D. H. Parker and P. Avouris, "Multiphoton ionization spectra of two caged amines," *Chemical Physics Letters*, vol. 53, no. 3, pp. 515–520, 1978.
- [149] M. A. Smith, J. W. Hager, and S. C. Wallace, "Two-color laser photoionization spectroscopy in a collisionless free-jet expansion: spectroscopy and excited-state dynamics of diazabicyclooctane," *The Journal of Physical Chemistry*, vol. 88, no. 11, pp. 2250–2255, 1984.
- [150] S. T. Pratt, "Photoionization of DABCO via high vibrational levels of the S_1 state," *Chemical Physics Letters*, vol. 360, no. 3-4, pp. 406 – 413, 2002.
- [151] A. M. Halpern, "The vapor state emission from a saturated amine," *Chemical Physics Letters*, vol. 6, no. 4, pp. 296 – 298, 1970.
- [152] G. Balakrishnan *et al.*, "The radical cation and lowest Rydberg states of 1,4-diaza[2.2.2]bicyclooctane (DABCO)," *The Journal of Physical Chemistry A*, vol. 104, no. 9, pp. 1834–1841, 2000.
- [153] D. Consalvo, J. Oomens, D. Parker, and J. Reuss, "DABCO: an investigation of the vibrational structured of the S_0 and S_1 state through two-photon LIF measurements," *Chemical Physics*, vol. 163, no. 2, pp. 223 – 239, 1992.
- [154] E. E. Ernstbrunner, R. B. Girling, W. E. L. Grossman, and R. E. Hester, "Free radical studies by resonance raman spectroscopy. Part 2.-diazabicyclo-octane radical cation," *J. Chem. Soc., Faraday Trans. 2*, vol. 74, pp. 501–508, 1978.
- [155] J. R. McDivitt and G. L. Humphrey, "Spectroscopic studies of the boron trihalide and borane complexes of 1,4-diazabicyclo[2.2.2]octane and quinuclidine," *Spectrochimica Acta Part A: Molecular Spectroscopy*, vol. 30, no. 4, pp. 1021 – 1033, 1974.
- [156] M. P. Marzocchi, G. Sbrana, and G. Zerbi, "Structure and fundamental vibrations of cage molecules. I. 1,4-diazabicyclo[2.2.2]octane," *Journal of the American Chemical Society*, vol. 87, no. 7, pp. 1429–1432, 1965.

- [157] M. A. Quesada, Z. W. Wang, and D. H. Parker, “Hot-band study of DABCO using resonant multiphoton optogalvanic spectroscopy,” *The Journal of Physical Chemistry*, vol. 90, no. 2, pp. 219–222, 1986.
- [158] M. Fujii, Y. Tsuchiya, and M. Ito, “Jahn-Teller splitting induced by penetration of the 4p-rydberg electron in 1,4-diazabicyclo[2.2.2]octane,” *The Journal of Physical Chemistry*, vol. 92, no. 9, pp. 2398–2400, 1988.
- [159] P. M. Felker, “Rotational coherence spectroscopy: studies of the geometries of large gas-phase species by picosecond time-domain methods,” *The Journal of Physical Chemistry*, vol. 96, no. 20, pp. 7844–7857, 1992.
- [160] C. Riehn, “High-resolution pump-probe rotational coherence spectroscopy – rotational constants and structure of ground and electronically excited states of large molecular systems,” *Chemical Physics*, vol. 283, no. 12, pp. 297 – 329, 2002.
- [161] Nokia-Corporation, “Qt - a cross-platform application and ui framework,” November 2012. <http://qt.nokia.com/>.

Appendix A

Convolution integrals

A.1 Double integral with variable limits of integration

A solution of the following double integral is shown in this section:

$$I_1 = \int_{-\infty}^{\infty} e^{-\frac{1}{2}\left(\frac{t-t_2}{\sigma_2}\right)^2} e^{-\lambda_A t} \int_{-\infty}^t e^{\lambda_A t'} e^{-\frac{1}{2}\left(\frac{t'-t_1}{\sigma_1}\right)^2} dt' dt. \quad (\text{A.1})$$

First, the power function in the inner integral has to be rearranged:

$$\begin{aligned} -\frac{(t'-t_1)^2}{2\sigma_1^2} + \lambda_A t' &= -\frac{(t'-t_1)^2}{2\sigma_1^2} + \lambda_A(t' - t_1) + \lambda_A t_1 = -\frac{(t'-t_1)^2 - 2\sigma_1^2 \lambda_A(t'-t_1)}{2\sigma_1^2} + \lambda_A t_1 = \\ &= -\frac{(t'-t_1)^2 - 2\sigma_1^2 \lambda_A(t'-t_1) + \sigma_1^4 \lambda_A^2 - \sigma_1^4 \lambda_A^2}{2\sigma_1^2} + \lambda_A t_1 = -\frac{(t'-t_1)^2 - 2\sigma_1^2 \lambda_A(t'-t_1) + \sigma_1^4 \lambda_A^2}{2\sigma_1^2} + \frac{\sigma_1^2 \lambda_A^2}{2} + \lambda_A t_1 = \\ &= -\frac{(t'-t_1 - \sigma_1^2 \lambda_A)^2}{2\sigma_1^2} + \frac{\sigma_1^2 \lambda_A^2}{2} + \lambda_A t_1. \end{aligned}$$

In order to simplify this expression, a new variable can be introduced: $x = \frac{t'-t_1 - \sigma_1^2 \lambda_A}{\sqrt{2}\sigma_1}$, $dt' = \sqrt{2}\sigma_1 dx$.

Exactly the same procedure can be done for the outer integral leading to a new variable: $y = \frac{t-t_2 + \sigma_2^2 \lambda_A}{\sqrt{2}\sigma_2}$, $dt = \sqrt{2}\sigma_2 dy$.

As a result of the above transformations, the resultant convolution integral can be written as following:

$$\begin{aligned} I_1 &= \int_{-\infty}^{\infty} e^{-y^2} e^{\frac{(\sigma_2 \lambda_A)^2}{2} - \lambda_A t_2} \int_{-\infty}^{y\sqrt{2}\sigma_1 + \sigma_1^2 \lambda_A} e^{-x^2} e^{\frac{(\sigma_1 \lambda_A)^2}{2} + \lambda_A t_1} \sqrt{2}\sigma_1 dx \sqrt{2}\sigma_2 dy \\ &= e^{\frac{(\sigma_2 \lambda_A)^2}{2} - \lambda_A t_2} e^{\frac{(\sigma_1 \lambda_A)^2}{2} + \lambda_A t_1} 2\sigma_1 \sigma_2 \int_{-\infty}^{\infty} e^{-y^2} \int_{-\infty}^{y\sqrt{2}\sigma_1 + \sigma_1^2 \lambda_A} e^{-x^2} dx dy. \end{aligned} \quad (\text{A.2})$$

It is important to note that the variable integration limit has changed after the substitution of the new variables: $-\infty < x < \frac{t-t_1 - \sigma_1^2 \lambda_A}{\sqrt{2}\sigma_1} = \frac{y\sqrt{2}\sigma_2 + t_2 - \sigma_2^2 \lambda_A - t_1 - \sigma_1^2 \lambda_A}{\sqrt{2}\sigma_1} =$

$y \frac{\sigma_2}{\sigma_1} + \frac{t_2 - t_1 - \lambda_A(\sigma_1^2 + \sigma_2^2)}{\sqrt{2}\sigma_1} = ky + b$, where the following substitutions have been made for our convenience:

$$\frac{\sigma_2}{\sigma_1} = k \text{ and } \frac{t_2 - t_1 - \lambda_A(\sigma_1^2 + \sigma_2^2)}{\sqrt{2}\sigma_1} = b. \quad (\text{A.3})$$

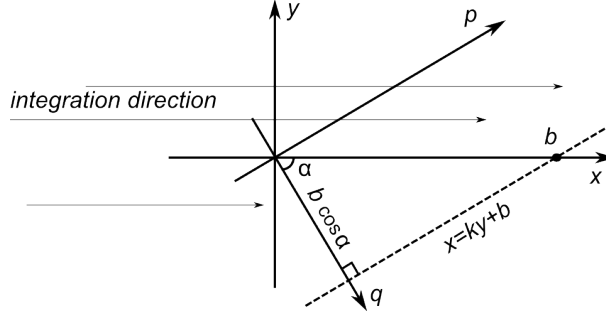


Figure A.1: Diagram of orthogonal coordinate systems (x, y) and (p, q) . Axis q is parallel to the integration limit $x = ky + b$. New axes (p, q) are rotated by α degrees with respect to the original (x, y) axes.

The area of integration for the double integral in equation (A.2) is shown in Figure A.1. While the y axis has infinite limits of integration, integration over the x axis goes from $-\infty$ until the line $x = ky + b$. In order to solve this double integral one can rotate the coordinate system in such a way that integration limits are decomposed and become independent of the integration variables. Such a transformation is shown in Figure A.1. The new coordinate system (p, q) is rotated by α degrees so that one of the axis is parallel to the integration limit $x = ky + b$. The angle α can be related to the known parameters of the integration limit:

$$\tan \alpha = k. \quad (\text{A.4})$$

It is clear from Figure A.1 that the limits of integration in the new coordinate system are:

$$\begin{aligned} -\infty < p < +\infty \\ -\infty < q < b \cos \alpha. \end{aligned} \quad (\text{A.5})$$

The relation between the new and the old coordinates is given by the rotation matrix, R_α :

$$\begin{pmatrix} q \\ p \end{pmatrix} = R_\alpha \begin{pmatrix} x \\ y \end{pmatrix} = \begin{pmatrix} \cos \alpha & \sin \alpha \\ -\sin \alpha & \cos \alpha \end{pmatrix} \begin{pmatrix} x \\ y \end{pmatrix}. \quad (\text{A.6})$$

The Jacobian of the transformation matrix is $\det R_\alpha = 1$, thus $dx dy = dq dp$. Using transformation (A.6), one can also show that $x^2 + y^2 = q^2 + p^2$. In this light, the double integral in equation (A.2) can be solved:

$$\begin{aligned}
I_2 &= \int_{-\infty}^{\infty} e^{-y^2} \int_{-\infty}^{yk+b} e^{-x^2} dx dy = \int_{-\infty}^{\infty} \int_{-\infty}^{yk+b} e^{-(x^2+y^2)} dx dy = \int_{-\infty}^{\infty} \int_{-\infty}^{b \cos \alpha} e^{-(q^2+p^2)} dq dp \\
&= \int_{-\infty}^{\infty} e^{-p^2} dp \int_{-\infty}^{b \cos \alpha} e^{-q^2} dq = \sqrt{\pi} \left(\int_{-\infty}^0 e^{-q^2} dq + \int_0^{b \cos \alpha} e^{-q^2} dq \right) \\
&= \sqrt{\pi} \left(\frac{\sqrt{\pi}}{2} + \frac{\sqrt{\pi}}{2} \operatorname{erf}(b \cos \alpha) \right) = \frac{\pi}{2} (1 + \operatorname{erf}(b \cos \alpha)),
\end{aligned} \tag{A.7}$$

where $\operatorname{erf}(x)$ is an error function. $\cos \alpha$ can be derived from equations (A.3) and (A.4) and the trigonometric relation, $\cos \alpha$ may be written:

$$\cos \alpha = \sqrt{\frac{1}{1 + \tan^2 \alpha}} = \sqrt{\frac{1}{1 + k^2}} = \frac{\sigma_1}{\sqrt{\sigma_1^2 + \sigma_2^2}}. \tag{A.8}$$

The final solution for the double integral I_1 is obtained by combining the result of equation (A.7) with equations (A.3) (A.8) and substituting it into equation (A.2):

$$\begin{aligned}
I_1 &= e^{\frac{(\sigma_2 \lambda_A)^2}{2} - \lambda_A t_2} e^{\frac{(\sigma_1 \lambda_A)^2}{2} + \lambda_A t_1} 2\sigma_1 \sigma_2 \frac{\pi}{2} (1 + \operatorname{erf}(b \cos \alpha)) \\
&= e^{\frac{(\sigma_2^2 + \sigma_1^2) \lambda_A^2}{2}} e^{-\lambda_A (t_2 - t_1)} \pi \sigma_1 \sigma_2 \left(1 + \operatorname{erf} \left(\frac{t_2 - t_1 - \lambda_A (\sigma_1^2 + \sigma_2^2)}{\sqrt{2} \sigma_1} \frac{\sigma_1}{\sqrt{\sigma_1^2 + \sigma_2^2}} \right) \right) \\
&= e^{\frac{\sigma^2 \lambda_A^2}{2}} e^{-\lambda_A (t_2 - t_1)} \pi \sigma_1 \sigma_2 \left(1 + \operatorname{erf} \left(\frac{t_2 - t_1 - \lambda_A \sigma^2}{\sqrt{2} \sigma} \right) \right),
\end{aligned} \tag{A.9}$$

where the substitution $\sigma = \sqrt{\sigma_1^2 + \sigma_2^2}$ has been made.

A.2 Triple integral with variable limits of integration

A solution of the following triple integral is shown in this section:

$$I_3 = \int_{-\infty}^{\infty} e^{-\frac{1}{2}\left(\frac{t-t_2}{\sigma_2}\right)^2} e^{-\lambda_B t} \int_{-\infty}^t e^{\lambda_B x} e^{-\lambda_A x} \int_{-\infty}^x e^{\lambda_A t'} e^{-\frac{1}{2}\left(\frac{t'-t_1}{\sigma_1}\right)^2} dt' dx dt. \quad (\text{A.10})$$

First consider the two inner integrals:

$$I_4 = \int_{-\infty}^t e^{\lambda_B x} e^{-\lambda_A x} \int_{-\infty}^x e^{\lambda_A t'} e^{-\frac{1}{2}\left(\frac{t'-t_1}{\sigma_1}\right)^2} dt' dx. \quad (\text{A.11})$$

It is possible to integrate the inner integral over the t' variable, however, an error function will be the result of the integration and, thus, analytical integration of the outer integral would be difficult. One possible option to overcome this problem is to change the order of the integration:

$$\int \int f(x, t') dt' dx \rightarrow \int \int f(x, t') dx dt'. \quad (\text{A.12})$$

Due to the variable upper integration limit, x , in the inner integral the change of the integration order requires additional considerations. Diagram A.2 shows the integration area for the double integral (A.11) which has the following borders:

$$\begin{aligned} -\infty < x &\leq t \\ -\infty < t' &\leq x. \end{aligned}$$

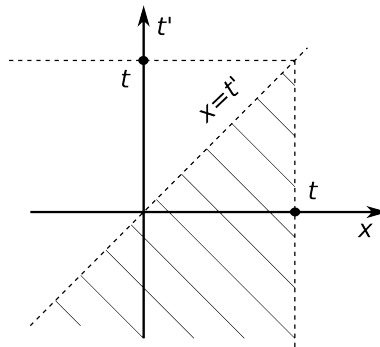


Figure A.2: Integration area of the double integral (A.11) filled with stripes. The bottom limit of the area is infinity.

When changing the order of the integration, the area of the integration shown in diagram A.2 must remain the same. Thus, the correct limits of the integration, after changing the order of the integration of the double integral (A.11), are:

$$\begin{aligned} -\infty < t' \leq t \\ t' < x \leq t, \end{aligned}$$

and the double integral changes to:

$$I_4 = \int_{-\infty}^t e^{\lambda_A t'} e^{-\frac{1}{2} \left(\frac{t'-t_1}{\sigma_1} \right)^2} \int_{t'}^t e^{\lambda_B x} e^{-\lambda_A x} dx dt'. \quad (\text{A.13})$$

Integration of the inner integral results in the sum of two exponential functions and expression (A.13) becomes a sum of two integrals:

$$\begin{aligned} I_4 &= \int_{-\infty}^t e^{\lambda_A t'} e^{-\frac{1}{2} \left(\frac{t'-t_1}{\sigma_1} \right)^2} \int_{t'}^t e^{(\lambda_B - \lambda_A)x} dx dt' \\ &= \int_{-\infty}^t e^{\lambda_A t'} e^{-\frac{1}{2} \left(\frac{t'-t_1}{\sigma_1} \right)^2} \frac{e^{(\lambda_B - \lambda_A)t} - e^{(\lambda_B - \lambda_A)t'}}{\lambda_B - \lambda_A} dt' \\ &= \frac{1}{\lambda_B - \lambda_A} \left[e^{(\lambda_B - \lambda_A)t} \int_{-\infty}^t e^{-\frac{1}{2} \left(\frac{t'-t_1}{\sigma_1} \right)^2} e^{\lambda_A t'} dt' - \int_{-\infty}^t e^{-\frac{1}{2} \left(\frac{t'-t_1}{\sigma_1} \right)^2} e^{\lambda_B t'} dt' \right]. \end{aligned} \quad (\text{A.14})$$

Substituting the result from equation (A.14) into the original equation (A.10):

$$\begin{aligned} I_3 &= \int_{-\infty}^{\infty} e^{-\frac{1}{2} \left(\frac{t-t_2}{\sigma_2} \right)^2} e^{-\lambda_B t} \times \\ &\quad \frac{1}{\lambda_B - \lambda_A} \left[e^{(\lambda_B - \lambda_A)t} \int_{-\infty}^t e^{-\frac{1}{2} \left(\frac{t'-t_1}{\sigma_1} \right)^2} e^{\lambda_A t'} dt' - \int_{-\infty}^t e^{-\frac{1}{2} \left(\frac{t'-t_1}{\sigma_1} \right)^2} e^{\lambda_B t'} dt' \right] dt \\ &= \frac{1}{\lambda_B - \lambda_A} \left[\int_{-\infty}^{\infty} e^{-\frac{1}{2} \left(\frac{t-t_2}{\sigma_2} \right)^2} e^{-\lambda_A t} \int_{-\infty}^t e^{-\frac{1}{2} \left(\frac{t'-t_1}{\sigma_1} \right)^2} e^{\lambda_A t'} dt' dt - \right. \\ &\quad \left. \int_{-\infty}^{\infty} e^{-\frac{1}{2} \left(\frac{t-t_2}{\sigma_2} \right)^2} e^{-\lambda_B t} \int_{-\infty}^t e^{-\frac{1}{2} \left(\frac{t'-t_1}{\sigma_1} \right)^2} e^{\lambda_B t'} dt' dt \right]. \end{aligned} \quad (\text{A.15})$$

The double integrals in equation (A.15) have the exact form as the one that has been solved in Appendix A.2. Therefore the final answer for the triple integral I_3 is:

$$\begin{aligned} I_3 &= \frac{\pi \sigma_1 \sigma_2}{\lambda_A - \lambda_B} \left[e^{\frac{\sigma^2 \lambda_B^2}{2}} e^{-\lambda_B(t_2 - t_1)} \left(1 + \operatorname{erf} \left(\frac{t_2 - t_1 - \lambda_B \sigma^2}{\sqrt{2} \sigma} \right) \right) - \right. \\ &\quad \left. e^{\frac{\sigma^2 \lambda_A^2}{2}} e^{-\lambda_A(t_2 - t_1)} \left(1 + \operatorname{erf} \left(\frac{t_2 - t_1 - \lambda_A \sigma^2}{\sqrt{2} \sigma} \right) \right) \right]. \end{aligned} \quad (\text{A.16})$$

Appendix B

Image Inversion software

B.1 Introduction

This appendix contains the description, user manual and brief compilation instructions for the software used to process and recover 3D velocity map images, using an inverse Abel transform, from the 2D projections. When using a VMI spectrometer, the inverse Abel transform is the main routine required in order to recover velocity spectra and angular distributions (see section 2.6.1). For this purpose, new software, later referred to as Image Inversion software, has been developed to perform this task.

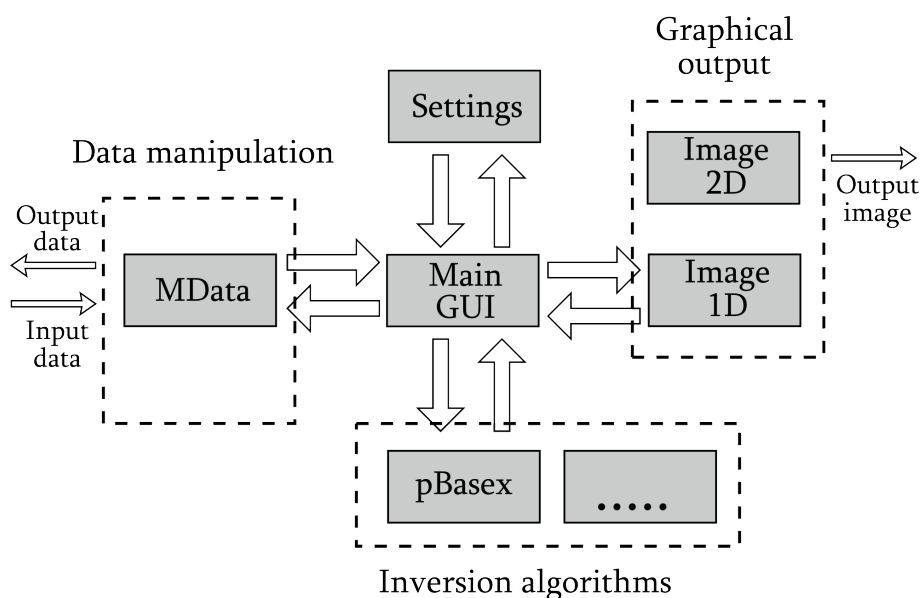


Figure B.1: Block diagram of the main modules of the Image Inversion software. The software consists of data manipulation, inversion algorithm and graphical output modules. All modules are controlled *via* a graphical user interface (GUI).

The source code and the compiled program under Windows XP is provided on the CD-ROM which is attached to the thesis. The program is divided into several modules (classes) where every module is responsible for certain tasks. Figure B.1 shows a block diagram of the Image Inversion program. The program structure can be divided into three main parts: data manipulation, inversion algorithms and graphical outputs. Each part can contain several classes. All classes are linked *via* the main user interface (UI). The data manipulation part currently includes a class *MData* which is responsible for 2D and 1D arrays manipulation. The inversion algorithm part has a single class for the inverse Abel transform based on the pBasex algorithm [96]. This class contains a modified version of the original routines written by Gustavo A. Garcia. The graphical output part contains two classes for visualisation of 2D and 1D arrays.

B.2 User manual

B.2.1 Computer requirements.

The program can be compiled under most operating systems (see section B.3), however, the attached CD-ROM provides a compiled standalone example for Windows XP. The software requires a sufficient amount of RAM in order to perform the pBasex inversion routine. The amount of RAM depends on the active basis set and can be estimated according to the following formula:

$$\text{RAM} = \text{NR} \times \text{NTH} \times \text{NL} \times \text{NK} \times 8 \text{ bytes}, \quad (\text{B.1})$$

where NR and NTH are the number of radial and azimuthal bins, IK is the size of the radial basis set and NL is the order of the Legendre polynomials. NK is hard-coded to be equal to NR/2. The minimum recommended available RAM for the program is 256 Mb.

B.2.2 GUI controls.

A layout of the Image Inversion program is shown in Figure B.2. The program GUI consists of three windows: a control window, a 2D image display window and a 1D image display window. The 2D image display window is used for displaying an original and inverted VMI and the 1D image display window is used for displaying

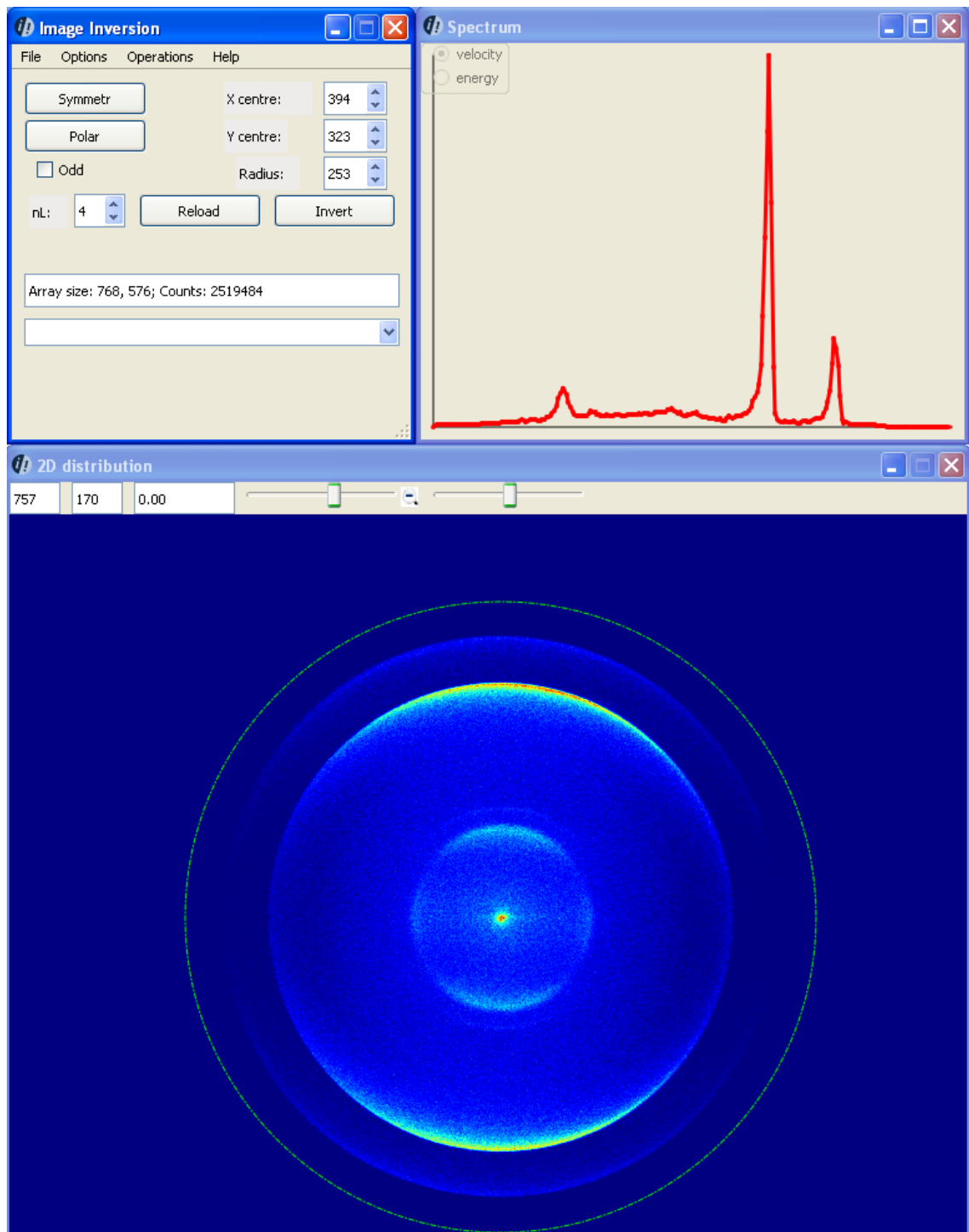


Figure B.2: Layout of the Image Inversion software interface designed for the processing of velocity map images. The main controls of the UI (top left), display of the 2D velocity map image (bottom) and display of the 1D velocity spectrum (top right).

a velocity spectrum. The control window includes the menu options and the control panel.

Menu options.

1. ***File*→*Open*→*ASCII***. Opens an ASCII file of the velocity map image. The Image Inversion program can open files in ASCII format only. Please make sure that the number delimiters are either tabs or spaces and each line ends with *end of line* symbol.
2. ***File*→*Open*→*Settings***. Sets up the number of lines which are skipped when the ASCII file is loading. This option is useful when the image file has a header that has to be ignored during the data read in.
3. ***File*→*Save*→*All***. Saves the following data arrays in the ASCII format: processed VMI (*.proc*), inverted VMI (*.inv*), photoelectron spectrum (*.pes*) and angular distribution (*.ang*). The first column in the *.pes* and *.ang* files corresponds to velocity in arbitrary units. The second column in *.pes* file is the photoelectron intensity. The second and all subsequent columns correspond to β parameters placed in ascending order, which were used during the inversion. β parameters are described in section 2.6.1.
4. ***File*→*Save*→*Image***. Saves an image which is currently displayed in the 2D image window. The image is saved in *.jpeg* format.
5. ***Options*→*Inversion area***. By default the program uses complete 2D when executing the inverse Abel transform routine. When selecting the *Within circle* option, only the pixels within the green circle, displayed in the image window, are used during the image inversion.
6. ***Options*→*Settings***. Sets up the basis set dimensions for the pBasex algorithm. *Save settings* saves current program settings into the file *user.set* and *Load settings* loads settings from the file *user.set*.
7. ***Operations*→*pBasex*→*Generate Basis***. Generates a pBasex basis set for the parameters set in *Options*→*Settings* and saves the basis set to the files. It can take several hours to generate a basis set, depending on the processor speed and the dimension of the basis set.
8. ***Operations*→*Image*→*Show***. Displays an initially loaded image in the 2D image window. Analogous to *Reload* button.

9. ***Operations***→***Image***→***Add***. Loads a 2D image from the ASCII file and adds it to the existing 2D image. The result is displayed in the 2D image window.
10. ***Operations***→***Background***→***Show***. Displays a background array in the 2D image window.
11. ***Operations***→***Background***→***Set***. Copies an active (loaded) 2D image into the background array.
12. ***Operations***→***Background***→***Add***. Adds an active (loaded) 2D image to the background array.
13. ***Operations***→***Subtract bkg***. Subtracts the background array from the active 2D image.
14. ***Operations***→***Invert files***. Performs the inverse Abel transform with the pBasex routine for multiple files and saves the result. After clicking, please choose multiple ASCII files in the dialog box by holding the *Ctrl* or *Shift* keys. Please make sure that the values of X centre and Y centre in the control panel are set correctly, before using this function.
15. ***Operations***→***Invert a set***. Performs the inverse Abel transform with the pBasex routine for multiple files in all subfolders of the chosen folder and saves the result. After clicking, please enter a destination folder so you can see all the subfolders with the data files and press *OK*. Afterwards, type the desirable file name. The program will invert all files with the chosen file name in every subfolder of the chosen folder. Please make sure that the values of X centre and Y centre in the control panel are set correctly, before using this function.

Control panel.

1. The centre position and the radius of the active circle displayed in the 2D image window can be controlled by spinboxes *X centre*, *Y centre* and *Radius*. *X centre* and *Y centre* values are used in the inversion routine as the centre of the image during the conversion from cartesian to polar coordinates.
2. ***Invert***. Performs the inverse Abel transform with the pBasex routine of a loaded 2D image and displays an inverted image and a velocity spectrum.

Make sure that the pBasex basis set files exist before attempting the inversion (see *Generate Basis* menu option).

3. **Reload**. Displays an initially loaded image in the 2D image window. Analogous to *Operations*→*Image*→*Show* menu option.
4. **Symmetr**. Symmetrises the image by mirroring the image with respect to the vertical line $x = X \text{ centre}$ and horizontal line $y = Y \text{ centre}$.
5. **Polar**. Converts active 2D image into polar coordinates and displays it in the 2D image window.
6. **nL spinbox** displays a maximum order of Legendre polynomials used in the pBasex inversion routine.
7. **Odd checkbox** defines whether odd Legendre polynomials are used during the inversion. If unchecked, only the even Legendre polynomials are used.

2D image window. The 2D image window is used for graphical display of any 2D array. The array is displayed using a 256 division colour map loaded from the file *colourmap.py*. The image colours can be scaled using the top right sidebar. When initially loaded, the size of the image is always equal to the actual number of rows and columns in the data file. It is possible to zoom in/out by adjusting the sidebar in the top left part of the window. Use the zoom out button in order to return to the original image size. The number fields in the top left corner display the cursor position and the pixel content under the cursor. Mouse functions: 1) right button single click changes the active circle centre to the cursor position; 2) right button hold and mouse drag changes the active circle centre to the cursor position and the radius of the circle; 3) left button double click allows to change the pixel content under the cursor (useful for removing bright pixels).

B.3 Development information and compilation instructions

Image Inversion software is based on the Qt cross-platform application framework [161]. Qt framework has several advantages: 1) its applications can be compiled under a

wide range of the operating systems (Windows, Linux/X11, Mac OS X and others); 2) it is available under the General Public License (GPL) and is freely available for the development of open source software; 3) it is based on widely used modular C++ class libraries; 4) it has a built in user interface (UI) designer; 5) it is a constantly developing framework.

Source files. The following source files are included in the Image inversion Qt project *Iminv.pro*:

- *main.cpp*: main program runs the application
- *mainwindow.cpp*: main GUI window with the control panel
- *mimageview.cpp*: 2D image display window
- *mspectrum.cpp*: 1D image display window
- *mdata.cpp*: data processing class
- *pbinversion.cpp*: pBasex inversion class
- *options.cpp*: options handler

Compilation. In order to compile the Image Inversion Qt project, *Iminv.pro*, first a Qt development software has to be installed according to the instructions provided on the Qt website [161]. Open *Iminv.pro* file with the Qt creator and follow the Qt manual for the compilation instructions. In addition, the GNU Scientific Libraries (GSL) have to be linked to compile the project and to perform the pBasex inversion. The compiled GSL dll files for Windows are provided on the disk; alternatively they can be compiled from the source code provided at <http://www.gnu.org/software/gsl>. Under most Linux based OS, GSL may be installed directly from the package installation manager. Please check that the path for the location of the GSL in the *Iminv.pro* is correct.